Early Detection of Brine and CO₂ Leakage Using Pressure and Surface-Deformation Monitoring Data: Methodology Development, Demonstration, and Application

29 November 2016

Disclaimer

This report was prepared as an account of work sponsored by an agency of the United States Government. Neither the United States Government nor any agency thereof, nor any of their employees, makes any warranty, express or implied, or assumes any legal liability or responsibility for the accuracy, completeness, or usefulness of any information, apparatus, product, or process disclosed, or represents that its use would not infringe privately owned rights. Reference therein to any specific commercial product, process, or service by trade name, trademark, manufacturer, or otherwise does not necessarily constitute or imply its endorsement, recommendation, or favoring by the United States Government or any agency thereof. The views and opinions of authors expressed therein do not necessarily state or reflect those of the United States Government or any agency thereof.

This report has been reviewed by Lawrence Berkeley National Laboratory and approved for public release.

Cover Illustration: Schematic of a typical storage system with CO_2 injection through an injection well into a deep storage formation, pressure monitoring at gauges and sensors (orange symbols) in the storage formation and overlying permeable aquifers, and Interferometric Synthetic Aperture Radar (InSAR) monitoring of ground-surface deformation, and with a permeable leaky fault and a leaky well that may act as leaky pathways of resident brine or injected CO_2.

An electronic version of this report can be found at:
http://www.netl.doe.gov/research/on-site-research/publications/featured-technical-reports
https://edx.netl.doe.gov/nrap

Early Detection of Brine and CO₂ Leakage Using Pressure and Surface-Deformation Monitoring Data: Methodology Development, Demonstration, and Application

Quanlin Zhou, Yoojin Jung, Fei Chen, Xiaoyi Liu, Jens T. Birkholzer, Michael B. Kowalsky, Tom Daley

Lawrence Berkeley National Laboratory, One Cyclotron Road, Berkeley, CA 94720

This page intentionally left blank.

Table of Contents

List of Figures

List of Figures (cont.)

List of Tables

Acronyms, Abbreviations, and Symbols

Term	Description
2-D	Two-dimensional
3-D	Three-dimensional
4-D	Four-dimensional
CO_2	Carbon dioxide
CSM	Colorado School of Mines
dp/dt	Pressure derivative signal
EE	Elementary effect
ERT	Electrical resistivity
GCS	Geologic carbon storage
GFZ	Geoforschungszentrum Potsdam
HM	Hydro-mechanical
InSAR	Interferometric Synthetic Aperture Radar
LBNL	Lawrence Berkeley National Laboratory
LW	Leaky well
MW	Monitoring well
NRAP	National Risk Assessment Partnership
NEGB	Northeast German Basin
NWGB	Northwest German Basin
OA	Overlying aquifer
PT	Polish Trough
SF	Storage formation
VERA	Vertical electrical resistivity array

Acknowledgments

This page intentionally left blank.

EXECUTIVE SUMMARY

This report summarizes the development, demonstration, and application of an inversion-based methodology for early leakage detection using pressure and surface deformation monitoring data. The report is one of two deliverables resulting from a Lawrence Berkeley National Laboratory (LBNL) National Risk Assessment Partnership (NRAP) project aimed at developing, testing, and applying novel methods for modeling carbon dioxide (CO_2) geologic storage and jointly inverting monitoring data for leakage detection. The ability to identify potential leakage pathways with monitoring data and continually monitor localized leakage of CO_2 and/or brine is essential for the science-based quantitative risk assessment at the core of the mission of the NRAP project.

The basic concept of early leakage detection is to identify pressure-driven brine leakage via joint inversion of pressure and deformation anomalies as early as possible, ideally long before the CO_2 plume would reach the leakage locations. If successful, this would provide early warning of potential CO_2 leakage, and risk management can be initiated to avoid CO_2 leakage. Risk management would likely start with simulating CO_2 migration to predict the timing and magnitude of CO_2 leakage through these pathways, which could then lead to deploying mitigation measures for leakage prevention as well as additional monitoring at the potential leakage locations. The monitoring data identified as particularly useful for early detection of brine leakage are: (1) pressure data from monitoring wells within/above the storage reservoir, and (2) Interferometric Synthetic Aperture Radar (InSAR) (and/or tiltmeter) data showing land surface deformations. Joint inversion of such complementary monitoring data types—the first providing quantitative measurements at a few borehole locations, and the latter giving quantitative and qualitative information over large areas—will improve early identification of the leakage signals and the high-permeability structures causing leakage. The inversion-based early leakage detection technique described in this report is complementary to current techniques for CO_2 leakage detection which are based on the physical, geophysical, or/and geochemical signatures that are induced by migrating CO_2 and that can be observed in the deep and shallow subsurface, at the land surface, and in the atmosphere. Many of these techniques have relatively low spatial resolution and coverage, in comparison to the footprint of CO_2 plumes, and all these techniques can only detect anomalous CO_2 signals long after CO_2 leakage has first occurred. The new technique developed in this project has the ability to provide an early indication of potential CO_2 leakage before it occurs.

Section 2 presents the concept and framework of early leakage detection. The framework developed consists of four key components: site characterization for known surface faults and abandoned wells, inversion-based early detection of brine leakage, CO_2 leakage prediction and monitoring, and decision-making for risk management and mitigation. A methodology was developed for early detection of potential CO_2 leakage from geological storage formations using pressure and surface-deformation anomalies. The early detection methodology involves automatic inversion of anomalous brine leakage signals with efficient forward pressure and surface-deformation modeling tools to estimate the location and permeability of leaky features in the caprock. A global sensitivity analysis was conducted to better understand under which conditions pressure anomalies can be clearly identified as leakage signals, and evaluate signal detectability for a broad parameter range considering different detection limits and levels of data noise. The detectability in terms of detection time and detection region for a given leakage

scenario (e.g., number, location, and permeability of leaky wells) can help understand the applicability of the early leakage detection methodology.

In Section 3, the inversion methodology for early leakage detection is used to estimate leakage parameters (i.e., the location and permeability of the leaky well) in four synthetic examples of idealized two-aquifer-and-one aquitard storage systems, with an injection well and a leaky well, for different monitoring scenarios. Example 1 assumes knowledge of formation parameters and pressure data with no uncertainties and errors. In this case, the inversion methodology produced accurate leakage estimates, regardless of whether the detection problem itself is unique or non-unique depending on the number and configuration of monitoring wells. In a random configuration of two monitoring wells, the inversion methodology may need different initial guesses to have accurate estimates of the leakage parameters and a best match for pressure data. The inversion results were stable after the first half year of injection and monitoring. In Example 2, which involved two monitoring wells and large pressure data noise, the inversion methodology improved the estimation accuracy of the leakage parameters with increasing monitoring time and data used in the inversion. The detection accuracy and convergence speed with time depend on the configuration of the two monitoring wells. For an optimal configuration, an accurate detection can be achieved within the first 2–3 years of monitoring. When the formation parameters are uncertain and the pressure data have large noise (Example 3), the detection can be improved by simultaneously calibrating the formation parameters and the leakage parameters using data of pressure anomalies in the overlying formations as well as the storage formation. As shown in Example 4, joint inversion of pressure and surface-deformation measurements can significantly improve the speed of convergence toward the true solution of the leakage parameters and enable earlier, accurate detection of the location of the leaky well. This example demonstrated that high-resolution deformation data can help locate the leakage pathway while the pressure data from a limited number of monitoring wells can help estimate the permeability of the leaky well or the leakage rate.

In Section 4, the methodology of early leakage detection is applied to hypothetical leakage problems at the Ketzin CO$_2$ pilot site in Germany. These problems are formulated by introducing a hypothetical leaky well located 675 m away from the injection well, with varying well permeability and leakage rate. Note that this is a purely hypothetical scenario. At Ketzin, no signals of leakage of brine and CO$_2$ through the Weser/Amstadt formation from the Stuttgart formation to the Exter formation were observed during the CO$_2$ injection over 5 years. The monitoring system at the Ketzin site consists of one injection well and two monitoring wells in the storage formation, and one monitoring well in the Exter formation. The application demonstration includes three components of the framework of the leakage detection system: site characterization, model calibration, and leakage detection. Model calibration was conducted to estimate large-scale spatial-varying permeability using pressure data observed during the pumping tests conducted prior to the CO$_2$ injection test. A forward model was developed using TOUGH2/EOS9, and the inverse modeling is conducted using iTOUGH2-PEST. The model calibration indicated that the storage formation in the near-well region contains sand channels and a low-permeability zone, and the near-well region is located in a semi-closed system with a flow barrier located in the north. The calibrated large geologic features are consistent with the field monitoring of CO$_2$ injection. For the early leakage detection, the "monitoring" pressure at the four wells was obtained by simulating the CO$_2$ injection into the Stuttgart formation with the hypothetical leaky well. The forward model was developed for an extended three-dimensional (3-D) domain of 15 km by 15 km covering the Stuttgart formation, the Weser/Amstadt

formation, and the Exter formation of ~260 m thickness in total, using site-specific data. Using a moderate injection rate of 1.59 kg/s for 2 years (i.e., 50,000 tonnes of CO$_2$ per year), the detection methodology can accurately estimate the leaky well permeability when the permeability is higher than 1,000 darcy, indicating that the methodology is applicable to detect large leakage events with high flow rates. If the injection rate increases by a factor of 10 (i.e., a half million tonnes CO$_2$ per year), a leakage event in a 10-darcy well can be accurately detected. The benefit of early leakage detection via inversion of pressure signals can be seen from the difference between the time of successful detection of a pressure anomaly from brine leakage (180 days) and the CO$_2$ arrival time (255 days) at the leaky well. If a leakage pathway for CO$_2$ can be detected in advance, mitigating measures can be undertaken to minimize the leakage risks, such as ceasing CO$_2$ injection or pumping CO$_2$ back out of the injection zone.

The authors of this report realize that the work conducted so far shows promise in that early leakage detection via joint inversion has been successful for simplified test cases and a fictitious leakage scenario for the Ketzin site. Without prior optimization of monitoring well location, detection was achieved in many example cases, but only when the leakage pathways had relatively large permeability and clear anomalies could be recorded. Further work is required to test the detection framework envisioned in this study, for a larger range of conditions and eventually in comparison with data from a field demonstration site in which actual leakage signals have been measured.

Further details of the material presented in this report were studied by Jung et al. (2013) and Chen et al. (2013).

1. INTRODUCTION

1.1 RESEARCH BACKGROUD

The ability to detect carbon dioxide (CO_2) leakage is a key component of risk assessment and management associated with geologic carbon storage (GCS) (IPCC, 2005; NETL, 2009). Injected CO_2 may escape from the deep storage formation to shallower groundwater aquifers, ultimately to the atmosphere, through abandoned wells that are not properly plugged (Gasda et al., 2004; Watson and Bachu, 2008), through permeable or semi-permeable faults that are pre-existing or injection-induced (Morris et al., 2011; Rutqvist, 2012), or through caprock fractures. Current techniques for CO_2 leakage detection are based on the physical, geophysical, or/and geochemical signatures that are induced by migrating CO_2 and that can be observed in the deep and shallow subsurface, at the land surface, and in the atmosphere (Benson, 2006; BES, 2007; Carroll et al., 2009; Oldenburg et al., 2003) (see Figure 1). For example, seismic reflection surveys may detect secondary accumulations of leaked CO_2 in overlying formations, groundwater sampling and soil gas surveys can be successful in the shallow subsurface (Romanak et al., 2012), and Eddy Covariance towers or airborne monitoring techniques can find CO_2 escaping from the subsurface into the atmosphere (Lewicki and Hilley, 2009; Lewicki et al., 2009; Strazisar et al., 2009).
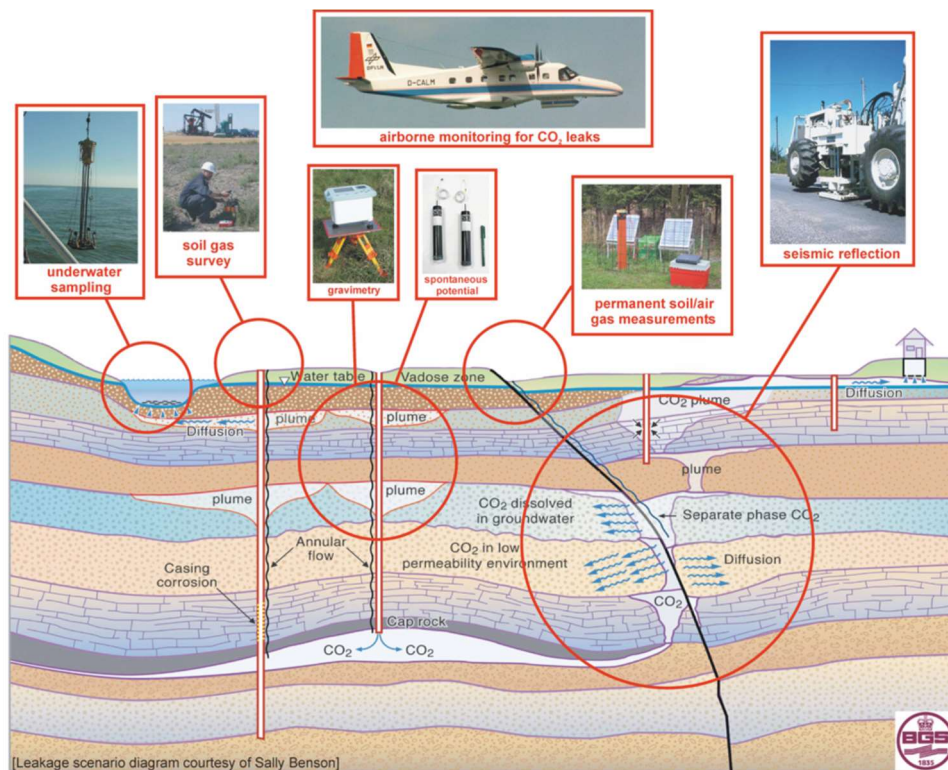
Figure 1: Example of the existing techniques used to measure geochemical-geophysical-hydrological subsurface properties and processes (BES, 2007).

One of the great challenges in CO_2 leakage detection is that many of these techniques have relatively low spatial resolution and coverage, in comparison to the footprint of CO_2 plumes that is on the order of tens of square kilometers for an industrial-scale GCS project (Zhou et al., 2010; Zhou and Birkholzer, 2011), and may not be effective in locating and identifying unknown leakage pathways that are not identified by near-field site characterization. The other great challenge is that all these techniques can only detect anomalous CO_2 signals long after CO_2 leakage has first occurred, thus lacking the ability to provide an early indication of potential CO_2 leakage before it occurs. For successful risk management of large-scale GCS, it is desirable to develop or devise a monitoring method capable of early detection of unknown leaky pathways.

Pressure-based detection techniques for CO_2 and brine leakage have recently been proposed in the community of GCS (Benson et al., 2006; Chabora and Benson, 2008; Nogues et al., 2011; Zeidouni et al., 2011; Sun and Nicot, 2012; Sun et al., 2013). The original idea of using pressure signals dates back to the 1980s when Javandel et al. (1988) proposed hydrologic detection of abandoned wells for hazardous waste disposal. To date, researchers have mainly focused on evaluating signal detectability via pressure monitoring in the aquifer overlying the storage formation, separated by a caprock formation. For instance, Benson et al. (2006) focused on pressure anomalies induced by brine leakage through a leaky abandoned well and a leaky fault, and concluded that the pressure-based detection method could be useful for providing early warning of large leaks within 1 year after the start of fluid injection. Chabora and Benson (2008) investigated the detectability of pressure signals at a monitoring well in the overlying aquifer, caused by brine leakage through the monitoring well or CO_2 leakage through the injection well. Nogues et al. (2011) investigated the spatial probability of being able to detect a leakage event using one monitoring well in an overlying aquifer, and determined the average time needed for successful detection. Zeidouni et al. (2011) formulated an inverse problem for leakage detection and evaluated the 95% confidence intervals of the location and transmissivity of the leaky well using up to five monitoring wells in the overlying aquifer. Sun and Nicot (2012) and Sun et al. (2013) applied different optimization methods to design optimal observation well placement for leakage detection using the pressure signals in the overlying aquifer.

All studies mentioned above used analytical forward models (Javandel et al., 1988; Avci, 1994; Nordbotten et al., 2004) assuming that the caprock was impervious and any pressure changes observed in the overlying aquifer were caused by well (or fault) leakage. However, intact caprock is usually of low, but not zero, permeability (Hart et al., 2006; Neuzil, 1994), and slow "diffuse" migration of brine through the caprock (referred to hereafter as diffuse leakage) may induce signals in the overlying aquifer that can be hard to discern from those related to focused leakage through leaky wells or faults (Zhou et al., 2010; Zhou and Birkholzer, 2011; Chabora and Benson, 2009; Birkholzer et al., 2009; Zhou et al., 2008). In other words, the pressure-anomaly signals of focused well (or fault) leakage in the overlying aquifer may be "contaminated" by diffuse leakage through the caprock or aquitard, in particular when the monitoring sensors in the overlying aquifer are not in the vicinity of the leakage location. Therefore, the effects of diffuse leakage through the caprock should be considered when evaluating early detection methods for focused leakage through leaky pathways (Cihan et al., 2011; Cihan et al., 2013).

Another concern about pressure monitoring for leakage detection is that it can be conducted at high temporal frequency, but is often limited to a few spatial locations (available only at a very small number of wells and gauges). Surface deformation measured by Interferometric Synthetic

Aperture Radar (InSAR) may be considered as a complementary monitoring tool for detecting large leaks. The InSAR technology provides dense spatial information on the scale of kilometers, and has been successfully used to assess ground surface deformation induced by earthquakes (Massonnet et al., 1993; Massonnet and Feigl, 1998), groundwater pumping and recharge (Galloway et al., 1998; Amelung et al., 1999; Bawden et al., 2001; Buckley et al., 2003; Hoffmann et al., 2003; Schmidt and Bürgmann, 2003; Bell et al., 2008; Galloway and Hoffmann, 2007), oil and gas production (Fielding et al., 1998; Xu et al., 2001), geothermal energy exploitation (Massonnet et al., 1997), and CO_2 injection and storage (Vasco et al., 2008a,b; Vasco et al., 2010). At least for large leakage events, it may be expected that the surface deformations induced by fluid leakage would show recognizable anomalies that can support early leakage detection methods, even at vegetated or urban sites (Amelung et al., 1999; Buckley et al., 2003; Schmidt and Bürgmann, 2003).

1.2   MOTIVATION

Industrial-scale CO_2 injection and storage in deep saline aquifers induce significant pressure perturbations that travel much faster in a heterogeneity-smoothing way than the heterogeneity-manifesting two-phase CO_2-brine flow. Pressure-induced phenomena (e.g., ground surface deformation) and their anomalous responses to leaking faults, abandoned wells, and other seal imperfections can be extremely useful for locating, identifying, and quantifying brine leakage pathways, and for providing early warning of potential CO_2 leakage.

The significant pressure buildup in the subsurface and the related detectable surface deformation offer an excellent opportunity for detecting and quantifying anomalous signals of resident fluid leakage through seal imperfections. These leaky seal imperfections may become, at a later time, leakage pathways of slower-migrating CO_2 accumulations. The early-detection concept has been explicitly identified in the Grand Challenge of Integrated Characterization, Modeling, and Monitoring of Geologic Systems in the *Basic Research Needs for Geosciences: Facilitating 21th Century Energy Systems* (BES, 2007, p. 80), as quoted:

> "*An important technological advance of integrated characterization and monitoring will be the development of systems that can be routinely used to detect and quantify phenomena that provide the earliest indication of processes that are unexpected in the manipulated system. A particular important example is the development of monitoring technology and strategies for early identification and quantification of CO_2 leakage, so that the hazard can be mitigated or remediated before the overall storage system integrity is compromised.*"

1.3   OBJECTIVES

To complement current CO_2 leakage detection techniques, the aim of this study was to develop, test, and apply a modeling-based method for an early leakage detection system relying on inverse analysis of pressure and, if available, surface deformation data. The concept of early detection of large leaks makes use of the fact that pressure signals travel very fast in the subsurface, and pressure-driven processes can be detected earlier than CO_2 migration processes. The concept of early leakage detection is thus to detect pressure-driven brine leakage through leakage pathways as early as possible, then use this knowledge to predict CO_2 plume migration in the storage reservoir and evaluate implications for CO_2 leakage, and finally to guide deployment of monitoring for improving data and detection, with the ultimate goal of mitigating leakage risks.

The framework of early leakage detection consists of four key components: site characterization for known surface faults and abandoned wells, early detection of brine leakage, CO_2 leakage prediction and monitoring, and decision-making for risk management and mitigation.

An inversion-based methodology was developed for early detection of potential CO_2 leakage from geological storage formations using pressure and surface-deformation anomalies. The methodology development in this report includes automatic inversion of anomalous brine leakage signals to estimate the location and permeability of leaky features in the caprock, a global sensitivity analysis to better understand under which conditions pressure anomalies can be clearly identified as leakage signals, and a detectability analysis for a broad parameter range considering different detection limits and levels of data noise in terms of detection time and detection region. For demonstration, the methodology of early leakage detection was applied to estimate leakage parameters (i.e., the location and permeability of the leaky well) in four synthetic examples of idealized two-aquifer-and-one aquitard storage systems, with an injection well and a leaky well, for different monitoring scenarios. These examples vary in the number and configuration of monitoring wells and in the type and quality of monitoring data. For example, in some cases it was assumed no pressure noise and in other cases large data noise was considered, inversions were conducted assuming that formation parameters are known without or with uncertainty, and only pressure data was used for the inversion or consider availability of both pressure and surface-deformation data available for detection. The demonstration indicated that early leakage detection can be successful in cases with relatively large leakage events when pressure signals are used from both the storage formation and the overlying aquifers. The accuracy of leakage detection can be improved by jointly inverting surface-deformation, if available, and pressure anomalies.

Finally, the inversion-based methodology of the early leakage detection was applied to hypothetical leakage problems at the Ketzin site in Germany. The problems were formulated by introducing a hypothetical leaky well located 675-m away from the injection well, with varying well permeability. It is assumed that the position of this well is known (e.g., abandoned well), but not whether the well integrity is such that it might act as a leaky pathway. The "monitoring" pressure at four wells in both the storage formation and the above zone was simulated for hypothetical CO_2 injection scenarios using TOUGH2/ECO2N. For the case with a constant CO_2 injection rate of 1.59 kg/s (50,000 tonnes CO_2 per year), the current configuration of monitoring wells would allow accurate detection of large leaks from the leaky well if the effective permeability is 1,000 darcy or higher. When the injection rate was increased to 15.9 kg/s (a half million tonnes CO_2 per year), the leakage signals became significantly stronger and leaks with a leaky well permeability of 10 darcy could be accurately detected.

2. DEVELOPMENT OF EARLY LEAKAGE DETECTION METHODOLOGY

This section presents the concept of early leakage detection with pressure and surface-deformation monitoring data, and briefly describes the four components of the framework for early leakage detection, which together would allow for improved risk assessment and mitigation. Details of the inversion modeling methodology are presented with the formulation of the detection problem using anomalies of pressure and surface deformation (induced by leakage) in comparison to no-leakage cases. The sensitivity and detectability analysis is presented with demonstration for an idealized storage formation using semi-analytical solutions for pressure and deformation. Note that the demonstration in this section and Section 3 is conducted for an idealized CO$_2$ storage system, which allows the use of efficient analytical solutions for single-phase flow. However, for a real application (Section 4), a numerical modeling of the coupled two-phase CO$_2$-brine flow and geomechanics was conducted (see Section 2.3.3).

2.1 CONCEPT OF EARLY LEAKAGE DETECTION

Figure 2 shows schematically a typical storage system with CO$_2$ injection through an injection well into a deep saline formation for storage of CO$_2$ (target reservoir), situated below a sequence of overlying near-impermeable aquitards and permeable aquifers (above-zone reservoir). Consistent with the idea of using pressure-based detection techniques, monitoring of pressure (in addition to temperature, CO$_2$ saturation, and fluid compositions) was envisioned at both the injection well and monitoring wells in the storage formation and overlying aquifers, and possibly InSAR monitoring of deformation at the ground surface. This study assumed that the site integrity is challenged by the presence of a permeable, hidden fault and a leaky well, through which resident brine or injected CO$_2$ could escape from the storage formation. For such a storage system, the objective of early leakage detection would be to locate, identify, and quantify initially unknown leakage pathways (e.g., leaky faults, fractures, abandoned wells) using the signals of fast-propagating pressure perturbation and surface-deformation anomalies caused by brine leakage. If successful, this would provide early warning of potential CO$_2$ leakage, and risk management can be initiated to avoid CO$_2$ leakage. Risk management would likely start with simulating CO$_2$ migration to predict the timing and magnitude of CO$_2$ leakage through these pathways, which could then lead to deploying mitigation measures for leakage prevention as well as additional monitoring at the potential leakage locations.

Whether unknown leakage pathways can be located and characterized via analysis of pressure and surface-deformation data will largely depend on (1) the detectability of the leakage signals, and (2) the effectiveness and accuracy of the inverse modeling methodology. Detectability is a function of strength of signal anomalies relative to data noise and model uncertainties, and signal strength depends on the magnitude of the leak and the properties of the storage formation and the overlying units. With respect to signal strength, industrial-size CO$_2$ injection is expected to generate strong and large-scale pressure perturbations. For example, the maximum pressure changes measured at the In Salah site in Algeria are as high as 100 bar (Rinaldi and Rutqvist, 2013), and the pressure buildup simulated for a hypothetical full-scale deployment scenario in the Illinois Basin exceeds 25 bar within a 120 km × 100 km region in the center of the basin (Zhou et al., 2010; Zhou and Birkholzer, 2011; Birkholzer and Zhou, 2009). If leakage pathways exist, such pressure increases in the storage reservoirs may lead to substantial brine migration into the overlying aquifer. The concept of above-zone pressure monitoring relies on the assumption that the resulting anomalous pressure signals in the overlying aquifer would be

clearly identifiable compared to pressure perturbations caused by other sources, such as those due to natural pressure fluctuations or the pressure changes resulting from diffuse leakage through the caprock. That is, the configuration of the pressure sensors (i.e., distance to leakage locations) may also be an important factor affecting detectability. Note that this project is not about optimization of sensor configuration; rather it assumed that the monitoring well setup and sensor configuration was given and that for this given scenario leakage detection via inverse modeling of pressure anomalies needs to be conducted.
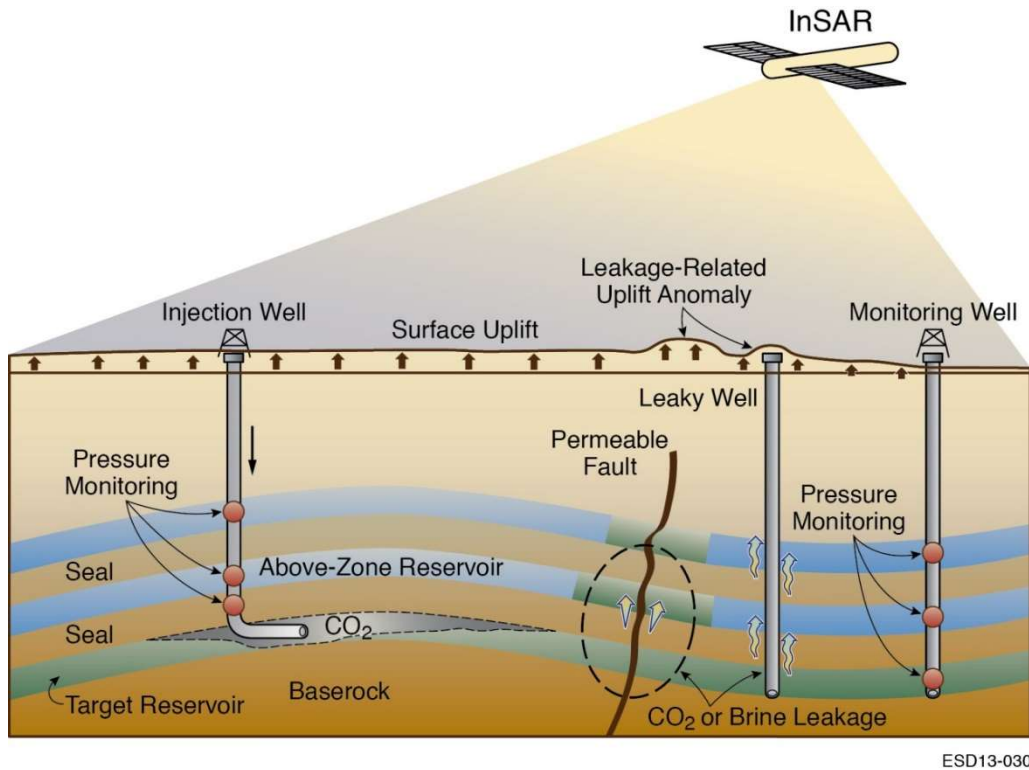
Figure 2: Schematic of a typical storage system with CO$_2$ injection through an injection well into a deep storage formation, pressure monitoring at gauges and sensors (orange symbols) in the storage formation and overlying permeable aquifers, and InSAR monitoring of ground-surface deformation, and with a permeable leaky fault and a leaky well that may act as leaky pathways of resident brine or injected CO$_2$.

A large-scale CO$_2$ storage project is also expected to induce noticeable surface deformation. Advanced InSAR techniques, which can capture surface deformation as small as 1 mm with a pixel resolution of 10 m × 10 m, have been successfully used to track transient surface deformations of up to 18 mm induced by injecting 4.3 million metric tonnes (Mt) of CO$_2$ at the In Salah CO$_2$ storage site in Algeria (Vasco et al., 2008a,b). The shape of the InSAR surface-deformation images also revealed the dynamic opening of a fracture or fault zone caused by high pressure buildup (Morris et al., 2011; Vasco et al., 2010; Rinaldi and Rutqvist, 2013). It may thus expect that InSAR monitoring can help capture localized surface deformations (i.e., anomalies) induced by fluid flow through seal imperfections (e.g., leaky faults, fracture zones, and clusters of abandoned wells).

Figure 3 was used to visualize the concept of early leakage detection using leakage-induced anomalies in pressure monitoring data, and to show the pressure evolution at a monitoring well in the storage formation and in the overlying aquifer as an example for leakage-relevant monitoring data. The red line represents the "measured" data at the monitoring sensors affected by a distant unknown leakage pathway, while the blue line indicates the "expected" pressure evolution at the same sensors using a pre-calibrated forward model for a case without a leaky pathway. Note that the shaded band following the red line indicates possible data noise stemming from instrument errors or natural fluctuations, and that the one following the blue line illustrates a range of uncertainty associated with the forward model. In both cases, the pressure increases in the storage formation were expected to be rapid and strong, and those in the overlying aquifer to be delayed and much more moderate. The difference between the red and the blue line is the pressure anomaly due to leakage; this difference is what was hoped to identify and use for the detection of an unknown leaky pathway.
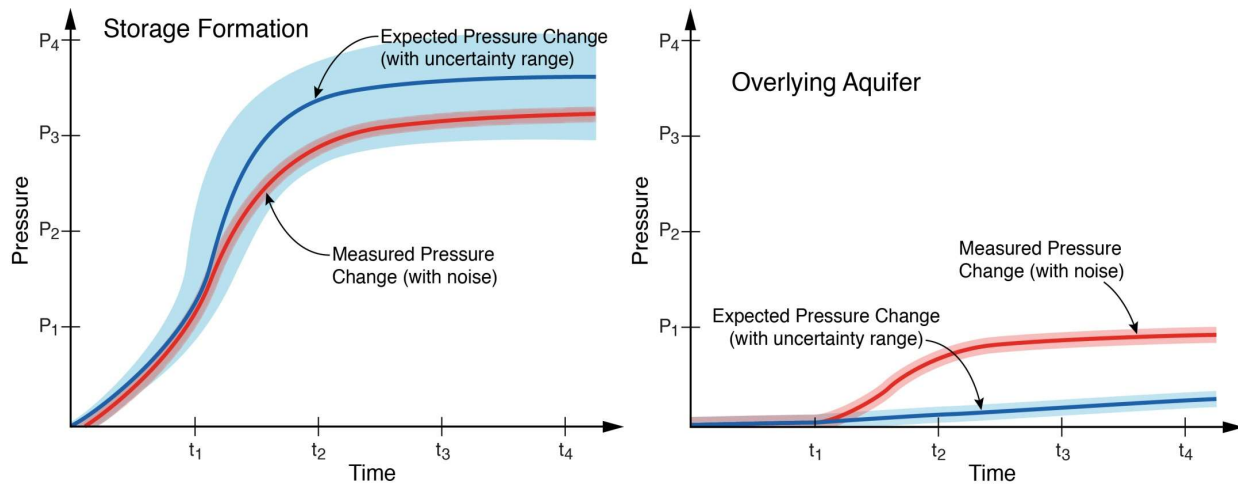
Figure 3: Schematic of pressure evolution at a monitoring well in the storage formation and the overlying aquifer: measured pressure change (with noise) in the red line and expected pressure change (with uncertainty range) in the blue line.

For the CO₂ storage system with pressure monitoring data as shown in Figure 3, if the "expected" behavior is substantially different from the "measured" pressure response, the study will need to account for the possibility of leakage pathways in the forward model. An inversion problem will then be defined in which the forward model with leakage pathways is used to minimize the difference between "measured" and "expected" behavior. However, a certain range of uncertainty associated with the forward predictions cannot be avoided because no forward model can account for all real-world phenomena. Even if the forward model reasonably captures the major mechanisms controlling the system responses, the calibration of model parameters is often not fully site-specific and has to rely on best guesses based on the available literature or past experiences. This uncertainty in the forward model parameters can make the detection of leakage anomalies more difficult. This study postulates that this is particularly true for the pressure measurements in the storage formation, where the leakage signals are relatively subtle compared to the overall pressure changes and may be just within the uncertainty range of the

forward predictions. Relative to the total pressure change induced by CO_2 sequestration, the leakage signal is qualitatively stronger in the overlying formation (where the expected pressure change without focused leakage should be slow and small) than in the storage formation. An important prerequisite for early leakage detection is thus that prediction of the expected system behavior needs to be conducted with as little uncertainty as possible. This requires detailed site characterization as well as thorough model calibration using all monitoring data available at a CO_2 storage site, such as CO_2 saturation, temperature, and geochemical changes (in addition to pressure perturbation and surface-deformation data), before and during CO_2 injection. Using the carefully calibrated forward model that provides the "expected" behavior of the storage system in the absence of leaky pathways, this study may be able to identify leakage anomalies and define an inversion problem to search for leaky pathways. Because leakage-induced anomalies are expected to become stronger as injection progresses, the estimation of leaky pathways should become increasingly reliable with incrementally more monitoring data available with time.

2.2   FRAMEWORK OF EARLY LEAKAGE DETECTION

Figure 4 shows the framework of the system of early leakage detection in support of the real-time operation and decision-making of a GCS project with risk management. This framework includes: (1) site characterization for known faults and abandoned wells; (2) early detection of brine leakage through hydro-mechanical joint inversion of pressure and deformation monitoring data; (3) CO_2 leakage prediction through CO_2-brine flow modeling, monitoring, and model calibration; and (4) decision-making on risk management and mitigation. Monitoring of the pressure-based phenomena (e.g., pressure perturbations and ground-surface deformation) and their anomalous responses to leaking faults, abandoned wells, and other seal imperfections may help locate, identify, and quantify these leaky pathways and provide early warning of potential leakage of CO_2 through these leaky pathways. The timing and flow rate of a CO_2 leakage event not only depend on the characteristics (e.g., geometry and permeability) of the detected leaky pathways, but also depend on the migration and trapping of CO_2 in the naturally heterogeneous storage formation, as well as the rock properties of the storage formation near the leaky pathways. This discussion is focused on: (1) monitoring of pressure and surface deformation, (2) detection of brine leakage through leaky pathways, (3) prediction of CO_2 leakage through model calibration, and (4) risk management and benefits of early leakage detection.

2.2.1   <u>Monitoring of Pressure and Surface Deformation</u>

The first component of the early-leakage-detection system is the monitoring of pressure perturbations at injection and monitoring wells and the InSAR monitoring of ground-surface deformation. As shown in Figure 2, the pressure monitoring may be conducted in the storage formation and the overlying permeable aquifers using pressure sensors. Automatic pressure monitoring can be conducted at high frequency (e.g., one data point every ~10 seconds), which for further analysis is often compressed to hourly or daily pressure data. The maximum pressure changes monitored ranged from 2.1 bar at the Frio I pilot site in Texas to as high as 100 bar at the In Salah site with industrial-scale CO_2 storage (Doughty et al., 2008; Rinaldi and Rutqvist, 2013). In a full-scale deployment scenario in which enough CO_2 is captured and stored to make relevant contributions to global climate change mitigation, the volumetric rates and cumulative volumes of CO_2 injection would be comparable to or higher than those related to existing deep-subsurface injection and extraction activities, such as oil production. In this scenario, the scale and magnitude of pressure buildup will be unprecedented (Zhou and Birkholzer, 2011). For

example, the simulated pressure buildup for a full-scale deployment scenario in the Illinois Basin is over 25 bar for a region of 120 km × 100 km (Birkholzer and Zhou, 2009; Zhou et al., 2010; Zhou and Birkholzer, 2011). The high pressure buildup over a large area may drive resident brine to leak from the storage formation via high-permeability leaky pathways, inducing anomalous pressure signals at monitoring wells. These anomalous pressure signals may be easily distinguished because the deep saline aquifers are not exposed to other significant perturbations and background pressure fluctuations are relatively small.
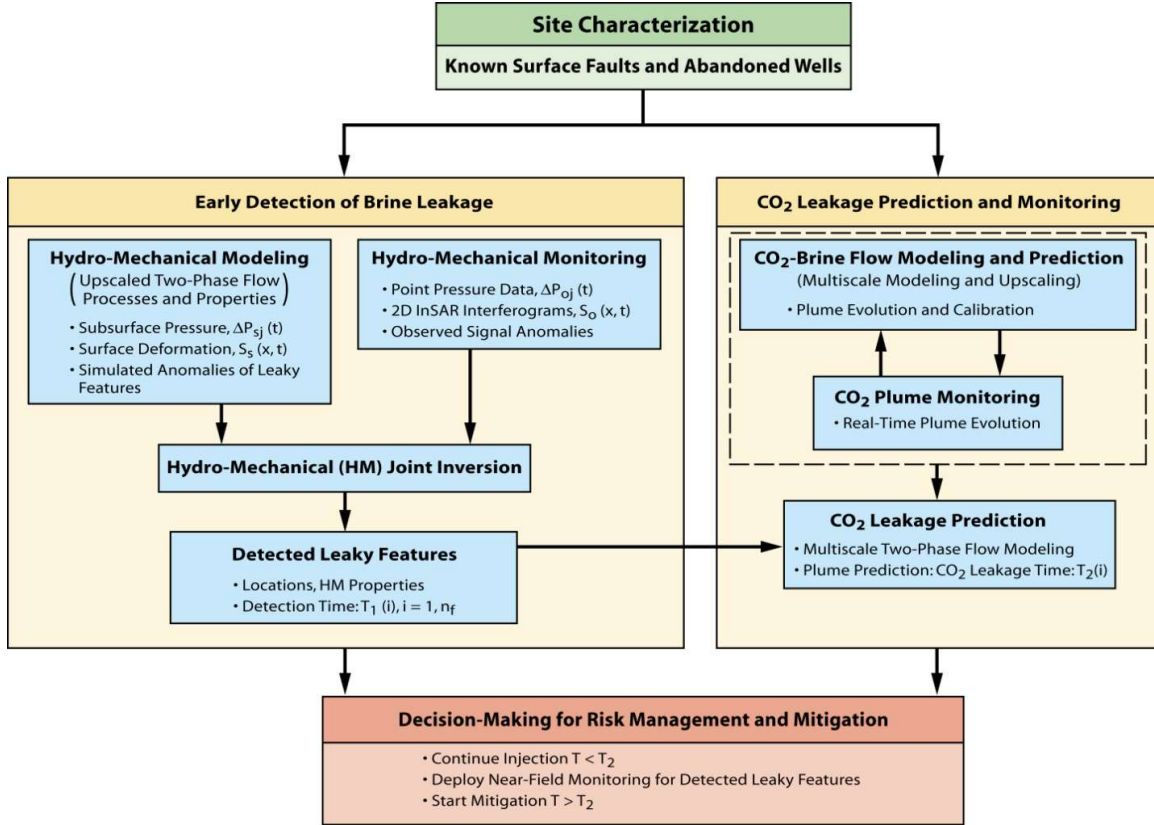
Figure 4: Flow chart of the early leakage detection system, showing the integration of site characterization, monitoring, and forward and inverse modeling, and the system components of (1) early detection of brine leakage, (2) CO$_2$ leakage prediction and monitoring, and (3) decision-making for risk management and mitigation.

If available, the high-frequency pressure monitoring at wells may be complemented by high-spatial-resolution InSAR surface-deformation monitoring. Advanced InSAR techniques can capture surface deformation as small as 1 mm with a pixel resolution of 10 m × 10 m over 100 km × 100 km for a track. For example, the InSAR monitoring techniques have been successfully used to track the transient surface deformation induced by injecting 4.3 million metric tonnes (Mt) of CO$_2$ over 7 years through three horizontal wells into a low-permeability sandstone formation at the In Salah site in Algeria (Vasco et al., 2008a,b). The surface deformation induced by injecting 1.13 Mt CO$_2$ at an injection well ranged from 2 mm to 18 mm in a region of 7 km × 11 km. In addition, the InSAR monitoring data at the In Salah site also revealed the dynamic opening of a fracture or fault zone induced by very high pressure buildup (Vasco et al., 2010;

Morris et al., 2011; Rinaldi and Rutqvist, 2013). Further InSAR applications to other GCS sites are expected from its extensive applications to subsidence or uplift induced by earthquakes (Massonnet et al., 1993; Massonnet and Feigl, 1998), groundwater pumping and recharge (Galloway et al., 1998; Amelung et al., 1999; Bawden et al., 2001; Hoffmann et al., 2001, 2003; Buckley et al., 2003; Schmidt and Bürgmann, 2003; Bell et al., 2008; Galloway and Hoffmann, 2007), oil and gas production (Fielding et al., 1998; Xu et al., 2001), and geothermal energy exploitation (Massonnet et al., 1997). The signature of mapped surface faults on the large-scale surface deformation has been clearly revealed in InSAR interferograms (e.g., Amelung et al., 1999; Bawden et al., 2001; Buckley et al., 2003; Schmidt and Bürgmann, 2003). These revealed faults may act as flow barriers and cause a cross-fault difference in pressure and surface deformation. This research found there are no reported detections of fluid leakage through wells and faults using InSAR interferograms in the literature. However, through the dynamic changes in GCS-induced deformation and fault-opening-induced deformation at the In Salah site, it is expected that InSAR monitoring can help capture localized surface deformations (i.e., anomalies) induced by fluid flow through seal imperfections (e.g., leaky faults, fracture zones, and clusters of abandoned wells) from the deep saline storage formation to shallow formations. Therefore, the high spatial resolution and large spatial coverage of InSAR monitoring can greatly improve the capability of the early-leakage-detection system in the presence of leaky structures.

2.2.2   Detection of Brine Leakage through Leaky Pathways

The time-dependent pressure and surface-deformation data can be used to detect brine leakage through leaky pathways. These pathways may not be in the vicinity of injection wells, because site characterization and small-scale pumping/injection tests are usually conducted to assure the near-field integrity of the storage formation. It may take some time for pressure buildup and surface deformation signals to propagate to these structures, and additional time for the monitoring data to show sufficiently strong anomalies induced by brine leakage through these structures to overlying/underlying aquifers. All these monitoring data can be used to calibrate the coupled hydro-mechanical model for a site-specific project. With time, the monitoring data show stronger signal anomalies, and the calibrated model can be further used to detect these leaky pathways using monitored pressure and deformation and their anomalies. The leakage detection objective is to estimate the location of the leaky pathways and their hydro-mechanical properties, such as well/fault permeability. The detection may reveal multiple leaky pathways at different times (e.g., $T_1(i)$, $i = 1$, n_f in Figure 4, where n_f is the number of leaky pathways). Note that the detection is based on the fast-propagating pressure and surface-deformation waves, and the brine leakage is used to detect the leaky pathways. With time, as more monitoring data become available, the detected locations and estimated permeability of the leaky pathways can be further refined with less uncertainties, and may converge to their true solutions.

2.2.3   Prediction of CO$_2$ Leakage through Model Calibration

The time-dependent risks of CO$_2$ leakage can be (1) predicted using multiphase flow and multicomponent transport modeling, and (2) monitored by conventional CO$_2$-based monitoring techniques (e.g., geophysical imaging). The modeling is conducted to simulate the migration and trapping of injected CO$_2$ in the form of free phase and dissolved CO$_2$. The monitoring of pressure, temperature, CO$_2$ saturation, and the arrival time of CO$_2$ plume to monitoring wells, as well as geophysical monitoring data, can be used to calibrate the two-phase CO$_2$-brine flow model (e.g., Doughty et al., 2008; Commer et al., 2014; Doetsch et al., 2013). The model

calibration can help gain confidence on the modeling results on CO$_2$ migration. The calibrated model can be also used to predict with confidence the arrival times of CO$_2$ to the leaky pathways detected by monitoring of brine leakage in Section 2.2.2. More importantly, the calibrated model can be used to plan whether and at which time injection should stop in order to keep the risk of CO$_2$ leakage below a certain level. One relevant task is to estimate the injection stop time for which there is no CO$_2$ leakage through the detected leaky pathways because of the trapping of CO$_2$ within the storage formation, referred to as T_2 in Figure 5. Note that the calibrated model should be further refined as additional monitoring data become available, and the estimates for injection stop time should be updated, with less uncertainty in its prediction.
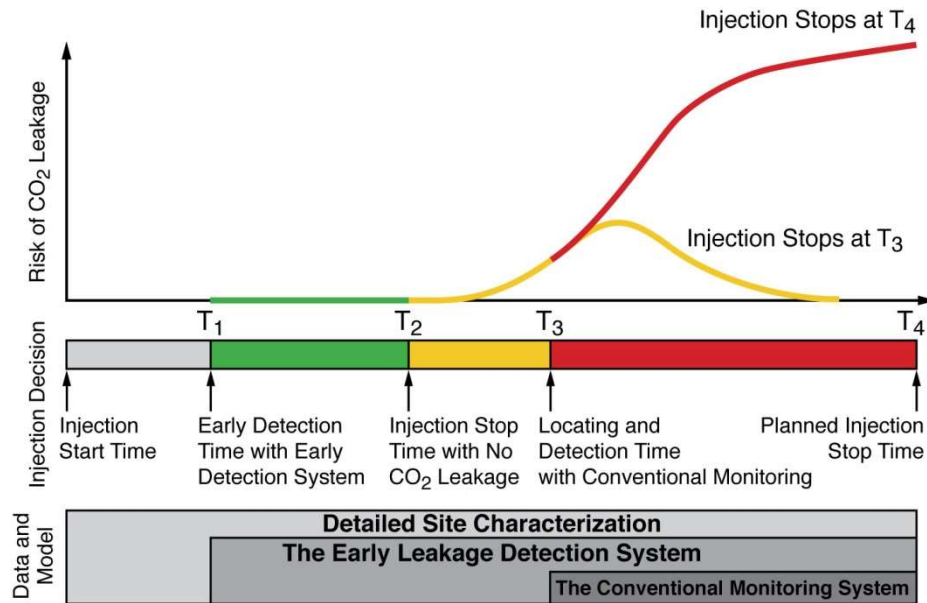
Figure 5: Time-dependent risk of CO$_2$ leakage associated with different decision-making scenarios based on (1) the detailed site characterization (i.e., injection stop at T_4), (2) the conventional CO$_2$-based detection techniques (i.e., injection stop at T_3), and (3) the proposed early leakage detection system (i.e., injection stop at T_2, with no or little risk of CO$_2$ leakage).

2.2.4   Risk Management and Benefits of Early Leakage Detection

If leaky pathways are present within the future extent of the CO$_2$ plume, the entire system of early leakage detection is important as shown in the decision-making component for risk management and mitigation (see Figure 4). The benefits of this system can be understood through Figure 5 by comparing the different risk of CO$_2$ leakage for the decision-making scenarios based on: (1) the detailed site characterization alone, (2) the combined site characterization and conventional CO$_2$-based monitoring and detection, and (3) the early leakage detection system. Without any monitoring in place, CO$_2$ injection would stop only when the planned project duration has ended, leading to the highest risk of CO$_2$ leakage. With conventional CO$_2$-based detection and modeling in place, it may take a considerable amount of time to locate and identify the leaky features after CO$_2$ leakage occurs. Operators would stop CO$_2$ injection at time T_3, and would take certain mitigation measures. However, the leakage risk may increase further for a while after injection stops because mobile free-phase CO$_2$ continues to

migrate to the detected leaky pathways. With the early leakage detection system in place, and with a good basis for risk management and mitigation planning, operators may be able to continue CO$_2$ injection until T$_2$ without any risk of CO$_2$ leakage, or until sometime between T$_2$ and T$_3$ if an insignificant amount CO$_2$ leakage is tolerable. That CO$_2$ leakage is indeed insignificant could be demonstrated with tailored CO$_2$-based monitoring based on the early detection of leaky features, and the monitoring data can then be used for model verification. The benefit of the early detection system is: (1) that the period between the time of hydro-mechanical detection of leaky seal imperfections (T$_1$) is much shorter than with conventional monitoring techniques, and (2) that therefore the risk of significant and lasting CO$_2$ leakage is reduced considerably. Note that it is assumed that detailed site-characterization can assure no leaky features are located near injection wells, so that no CO$_2$ leakage risk is shown until detection time T$_2$.

2.3 INVERSION MODELING METHODOLOGY

An efficient inverse modeling methodology was developed for early leakage detection using pressure and deformation monitoring data (Section 2.3.1). Predictions of pressure and surface deformation were obtained either through a fast semi-analytical solution described in Section 2.3.2 for methodology demonstration, or through numerical modeling of coupled two-phase flow and geomechanics described in Section 2.3.3 for real applications. The new methodology was applied to four synthetic examples in Section 3 and one real application in Section 4.

2.3.1 <u>Inverse Modeling for Early Leakage Detection</u>

The objective of the early leakage detection via inverse modeling is to locate the leaky pathway (i.e., determine the coordinate of a leaky well) and to calibrate the leaky well permeability. A large-scale CO$_2$ injection project may cause pressure changes exceeding tens of bars in the storage formation, and may induce surface deformations as high as a few centimeters. In an effort to calibrate formation parameters via inverse models, one would directly use these pressure or surface-deformation monitoring data which reflect the absolute changes from the initial site conditions. However, for the formulation of the leakage inverse problem, it may be more valuable to invert for pressure and deformation anomalies. These anomalies are obtained by calculating the difference (i.e., anomaly) between the "monitored" system response (induced by both injection and leakage) and the "expected" system response (induced by injection only). That is, for a leakage scenario with a leaky well, the pressure anomaly is defined as the difference between a case with well leakage and a case without well leakage ($= h_w - h_{wo} = \Delta h_{w-wo}$). The deformation anomaly is defined as the difference of deformation on the ground surface between a case with well leakage and a case without well leakage ($= b_w - b_{wo} = \Delta b_{w-wo}$). Using anomalies rather than absolute values may ensure that the leakage signals are more clearly brought out in the inversion process. Particularly in the case of the pressure data, pressure anomalies in the storage formation become of similar magnitude to those in the overlying aquifer, which may help improving the inverse problem solution.

The inverse modeling, as well as the sensitivity analysis described in the Section 2.4.2, was conducted with iTOUGH2-PEST (Finsterle, 2011; Fisterle and Zhang, 2011). iTOUGH2 is a computer program for parameter estimation, sensitivity analysis, and uncertainty propagation analysis (Finsterle, 2005, 2007), and developed for use with the TOUGH2 forward simulator for nonisothermal multiphase flow in porous and fractured media (Pruess et al., 1999). While

iTOUGH2-PEST inherits all the capabilities of iTOUGH2, it utilizes the PEST protocol (Doherty, 2007a,b) as a way to communicate with any generic forward model (e.g., the analytical pressure and deformation models described in Section 2.2.2), and therefore can be used as a model-independent parameter estimation, sensitivity, and uncertainty propagation code. For the estimation of the location and permeability of a leaky well, iTOUGH2-PEST seeks to minimize the misfit between the "monitored" and the "expected" system responses (i.e., pressure and surface-deformation anomalies) at selected calibration points in space and time:

$$S = \sum_{j=1}^{n} \frac{r_j^2}{\sigma_j^2} = \sum_{j=1}^{n} \frac{(z_j^* - z_j)^2}{\sigma_j^2} \tag{1}$$

where S is the objective function, r_j is the difference (residual anomaly) between the measured anomaly z_j^* and the computed anomaly z_j at calibration point j (= 1, … , n), and σ_j^2 is the variance of the observations, whose inverse acts as a weight factor for each data type. The calibration points included the pressure anomalies available at all pressure gauges installed in the monitoring wells and the surface-deformation anomalies available within the spatial extent of the storage system. The objective function was minimized by iteratively adjusting the location and permeability of the leaky well. The Levenberg-Marquardt method, which is based on the calculation of the second-order derivatives of the function, was used to find the minimum of the objective function (Levenberg, 1944; Marquardt, 1963). It should be noted that iTOUGH2 provides a number of other objective functions and minimization algorithms in addition to the ones used in this study.

2.3.2   Efficient Forward Modeling of Pressure Buildup and Surface Deformation

For methodology demonstration, this study was interested in efficient predictive tools for simulating transient pressure buildup in multiple formations and the associated surface deformations in response to large-scale CO_2 injection and storage. During the early stage of brine leakage (before the arrival of CO_2 plume at leaky wells), the brine flow and pressure changes outside of the CO_2 plume can be described with reasonable accuracy by analytical or numerical models for single-phase flow (Cihan et al., 2013; Nicot, 2008), thus significantly reducing the computational cost compared to more complex multiphase process models typically used for risk assessment and management of a GCS site. Similarly, the calculation of surface deformation does not require high-resolution CO_2 plume modeling at early times after the start of CO_2 injection. In some of the examples described in this report, a semi-analytical solution was used by Cihan et al. (2011) to calculate pressure changes induced by well injection and leakage in an idealized multilayered aquifer-aquitard system. Surface deformations were subsequently estimated based on the simulated pressure changes using the semi-analytical solution and the geomechanical properties of each aquifer and aquitard. The semi-analytical solution allows for multiple injection/pumping wells into/from aquifers and accounts for both diffuse leakage through aquitards and focused leakage through multiple leaky wells. Each aquifer/aquitard is homogeneous and isotropic with uniform thickness and infinite extent. Different layers may have different geometric and hydrogeological parameters. Flow in the aquifers was assumed to be horizontal and flow in the aquitards is assumed to be vertical.

Based on the pressure changes, the surface deformation is approximated by adding the vertical volumetric change in each formation from the impervious bottom boundary to the ground surface. For a homogeneous and laterally infinite aquifer, the vertical volumetric change at a given location can be calculated as (Fjær et al., 2008):

$$\frac{b}{B} = \alpha \frac{(1+v)(1-2v)}{(1-v)E} \Delta P$$

$$(2)$$

where b is the vertical expansion of the aquifer, B is the thickness of the aquifer, α is Biot's coefficient, v is Poisson's ratio, E is Young's modulus, and ΔP is the change in aquifer pressure. For a semi-pervious aquitard, the total vertical change can be calculated similarly by integrating the pressure changes along the vertical direction. The simplifying assumptions made in this calculation are that: (1) the formation deformation occurs only in the vertical direction, with negligible lateral deformation and without accounting for formation stiffness; (2) the vertical volumetric deformation in each formation is independent of the deformation in overlying or underlying formations; and (3) the effective stress varies as a function of pressure changes, without any change in the total stress from in situ conditions. It has been shown that this approximate method is sufficient to provide a reasonable estimate of a few-centimeter uplift observed at the In Salah CO₂ injection site (Rutqvist, 2012).

The semi-analytical solutions for pressure and surface deformation were used for an idealized storage system (Figure 6) for demonstrating sensitivity and detectability analysis (Section 2.3) and early leakage detection (Section 3).

2.3.3   Numerical Modeling of Pressure Buildup and Surface Deformation

In a real-world application of the early leakage detection method (Section 3), the multi-phase simulator TOUGH2-MP/ECO2N (Pruess et al., 1999; Pruess, 2005; Zhang et al., 2008) was used to simulate pressure perturbation and CO₂ saturation in response to both injection and leakage. When surface deformation data were available and used in the early leakage detection, the coupled hydro-mechanical simulator, TOUGH2-CSM, was used to simulate pressure perturbation, CO₂ saturation, and surface deformation. This simulator was developed by Colorado School of Mines (CSM) to extend the TOUGH2-MP simulator to model coupled hydro-mechanical (HM) processes and deformation (Winterfeld and Wu, 2011). In the fully coupled model, the pressure and saturation for CO₂-brine multiphase flow and the mean normal stress for geomechanical process were solved simultaneously for each numerical gridblock at every time.

2.4   SENSITIVITY AND DETECTABILITY ANALYSIS

In this first synthetic example, a sensitivity and detectability analysis was conducted for pressure monitoring data. The model system consisted of a target storage formation bounded by an impervious boundary at the bottom, the caprock of a semi-pervious aquitard, and an overlying aquifer bounded by an impervious boundary at the top. Fluid injection occurred through an injection well into the storage formation, and resident brine leaks through a distant leaky well into the overlying aquifer, a result of the hydraulic gradient caused by pressure increase in the

storage formation. Pressure was monitored in both the storage formation and the overlying aquifer at the injection and monitoring wells.

2.4.1 <u>Model Setup and Forward Modeling</u>

The injection well is located at the center of the model domain [0 km, 0 km], and the leaky well is located 2 km away from the injection well [2 km, 0 km] (see Figure 6b). Since a single-phase model is used for forward predictions, CO_2 injection is represented in this example by injection of an equal volume of brine. An industrial-scale CO_2 storage operation was assumed, which injects into the storage formation at a constant volumetric rate, $Q = 5,700$ m^3 d^{-1}. The time period of interest is 10 years after the start of injection. The radius of the injection and the leaky well is 0.15 m, and the leaky well permeability in the base case is $k_L = 2 \times 10^{-7}$ m^2. The geometric parameters and rock properties of the storage formation, the overlying aquifer, and the caprock in the base case are shown in Table 1. Note that the hydraulic conductivity for the two aquifers in Table 1 is equivalent to a permeability $k = 2 \times 10^{-13}$ m^2, assuming brine density of $\rho = 1,075$ kg m^{-3}, gravity acceleration of g = 9.8 m s^{-2}, and water viscosity of $\mu = 0.9 \times 10^{-2}$ Pa·s. The hydraulic conductivity of the aquitard is equivalent to a permeability $k = 2 \times 10^{-19}$ m^2. The specific storativity value for the aquifers corresponds to an aquifer pore compressibility of $\beta_p = 4.5 \times 10^{-10}$ Pa^{-1} and a porosity of 0.2, while the specific storativity value of the caprock corresponds to a pore compressibility of $\beta'_p = 9.0 \times 10^{-10}$ Pa^{-1} and a porosity of 0.1. All parameters are assumed to be homogeneous in the laterally infinite formations of uniform thickness, and the hydraulic conductivity (or permeability) is isotropic. The selection of formation properties is based on previous studies on large-scale storage of CO_2 (Birkholzer et al., 2009; Birkholzer et al., 2012; Zhou et al., 2009).

For now, it is assumed at this point that a "perfect" pre-calibrated forward model is available for predicting the CO_2 storage system behavior without leaky pathways. The term "perfect" here refers to a model that can predict without any error or uncertainty the "expected" behavior of the storage system in the absence of leaky pathways. That is, the formation parameters are known through site characterization and model calibration, and the inversion parameters to be calibrated are the location and effective properties of leaky pathways. The focus of this study is on testing the inversion method and its detection performance for different monitoring configurations, different formation and leakage characteristics, and different levels of data noise at different times during CO_2 injection.

2.4.2 <u>Parameter Sensitivity</u>

This study is interested in understanding the sensitivity of leakage signals to the input model parameters given in Table 1. A global sensitivity analysis was conducted to determine the parameters that have the most significant impact on pressure anomalies for a variety of conditions. A global sensitivity analysis assesses the response of the model output to changes in the model parameters varied over given parameter ranges. As shown in Table 1, parameter ranges were selected that are quite wide, with the intention of evaluating sensitivity over a variety of representative storage site characteristics (in contrast to assessing local sensitivity for one site with uncertain parameters). For example, the aquifer hydraulic conductivity varies by two orders of magnitude, the aquifer specific storativity varies by a factor of five, and the aquifer thickness varies between 30 m and 120 m. In total, ten model parameters were selected to be included in the global sensitivity analysis. In addition to the aquifer parameters stated above, the

respective properties of the aquitard and the leaky well permeability were varied. For the leaky well permeability, a range from 2×10^{-11} m^2 to 2×10^{-5} m^2 was considered. The upper bound of the range represents a very conservative leakage case with substantial leakage potential and impact, perhaps representative of an open borehole or a well in which typical abandonment methods either have not been implemented or have completely failed. The lower bound is within the upper range of leaky well permeabilities discussed in previous studies (Cihan et al., 2013; Celia et al., 2011), where leakage pathways along wells considered flow paths along the rock-cement interface, along the casing-cement interface, and through fractures or cracks within the cement or the surrounding rock. As the model output, the pressure anomalies Δh_{w-wo} were evaluated in the storage formation and the overlying aquifer at three monitoring-well locations: MW1, MW2, and MW3, which are at [1.5 km, 0 km], [4 km, 0 km], and [-2 km, 0 km] and are 0.5, 2.0, and 4.0 km away from the leaky well, respectively (see Figure 6b).

Table 1: The base-case, minimum, and maximum values of geometric and hydrogeologic parameters of the storage formation (SF), the aquitard, and the overlying aquifer (OA)

Parameters[*]	Variable	Base Case	Min	Max
Thickness of SF (m)	B_1	60	30	120
Thickness of OA (m)	B_2	60	30	120
Hydraulic conductivity of SF (m d^{-1})	K_1	0.2	0.02	2.0
Hydraulic conductivity of OA (m d^{-1})	K_2	0.2	0.02	2.0
Specific storativity of SF (1/m)	S_1	1.88E-6	1.00E-6	5.00E-6
Specific storativity of OA (1/m)	S_2	1.88E-6	1.00E-6	5.00E-6
Thickness of aquitard (m)	B'	100	50	200
Hydraulic conductivity of aquitard (m d^{-1})	K'	2.0E-7	2.0E-8	2.0E-6
Specific storativity of aquitard (1/m)	S'	1.47E-6	1.00E-6	5.00E-6
Leaky well permeability (m^2)	k_L	2.0E-7	2.0E-11	2.0E-5

The global sensitivity analysis was conducted using the elementary effects method (Morris, 1991; Saltelli et al., 2008). This method is widely used to screen parameters in models of large dimensionality, and its application does not rely on strict assumptions about the model behavior, such as linearity, additivity, and monotonicity of the model input-output relationship. The elementary elements method consists of r times of global sampling of all k model parameters within their defined ranges of possible values and calculation of elementary effects for the parameters at the jth global sampling ($j = 1, ..., r$). The elementary effect (EE) of a model parameter is defined as the difference of the model output of interest caused by the local change in the respective parameter. For efficient sampling, instead of independently sampling a pair of points for each parameter, a total of $2rk$, ($k+1$) points are sequentially selected within the parameter space by changing the value of one parameter at a time in a random order, building a trajectory of ($k+1$) points, for a total of $r(k+1)$ sample points. The base point at each global

sampling j is randomly sampled within the range of each model parameter. From the distribution of EE obtained by a sufficient number r of global sampling, the elementary effects method provides both mean and standard deviation as two sensitivity measures for each model parameter. The mean value assesses the overall influence of a model parameter on the model output, while the standard deviation describes non-linear effects and interactions with other model parameters. In the example study, 100 global samples were used to calculate the EE values in each of the six cases of monitoring locations and aquifers, and the mean and the standard deviation were calculated as a function of injection time. The number of the global samplings was determined so that reasonable convergence of the mean EE could be achieved.

Figure 6 shows the temporal changes of the mean EE values of the pressure anomaly Δh_{w-wo} at three monitoring-well locations (MW1, MW2, and MW3) for five model parameters: hydraulic conductivity (K_1) and thickness (B_1) of the storage formation, hydraulic conductivity (K_2) and thickness (B_2) of the overlying aquifer, and the leaky well permeability (k_L). The mean EE values for the other five parameters are not shown because their influences on Δh_{w-wo} are relatively less significant. At MW1, the mean EE values for B_2 and K_2 are positive in the storage formation, but negative for B_1 and K_1. For a given constant injection rate, an increase in B_1 and K_1 will reduce the leakage rate and cumulative leakage volume through the leaky well since the driving force (pressure buildup in the storage formation at the leaky well) becomes smaller, resulting in negative mean EE values. When B_2 and K_2 increase, the resistivity of the overlying formation to impede well leakage becomes smaller, which lowers the pressure buildup in the overlying formation and thus leads to an increase in leakage rate and volume. Regardless of the sign of the mean EE values, their absolute magnitude consistently increases with time, suggesting that signal detectability should improve as injection continues. At a given time, the sensitivity of Δh_{w-wo} to the model parameters decreases with the increase of distance between the monitoring well and the leaky well (from MW1 to MW3). For example, at 5 years, the EE values of K_2 and B_2 for the storage formation change from 1.0 and 0.4 at MW1, to 0.5 and 0.2 at MW2, and to 0.3 and 0.1 at MW3.

Among the four formation parameters, K_1 is the most influential parameter affecting pressure signals in the storage formation, while B_1 is the next most influential model parameter (see Figures 6a-c). In the overlying aquifer (see Figures 6d-f), all four formation parameters have negative mean EE values, and the two most influential parameters are K_2 and K_1. Interestingly, the leaky well permeability k_L has a considerable influence on the pressure anomalies, but it is not the most sensitive parameter. In the storage formation, the pressure anomalies are less sensitive to k_L than to K_1 and B_1 over the entire time of injection, and to K_2 during the later time of injection. In the overlying aquifer, k_L is always less influential than all formation parameters. This suggests that accurate knowledge of the formation parameters will be critical to the success of well leakage detection. Note that the EE values of k_L are positive at all the tested locations, increase with time in both the storage formation and the overlying aquifer, and decrease with distance from the leaky well. Although the EE values for the storage formation are slightly higher than those for the overlying formation, their differences are not significant. This indicates that monitoring of pressure anomalies in both aquifers may be important for well leakage detection.
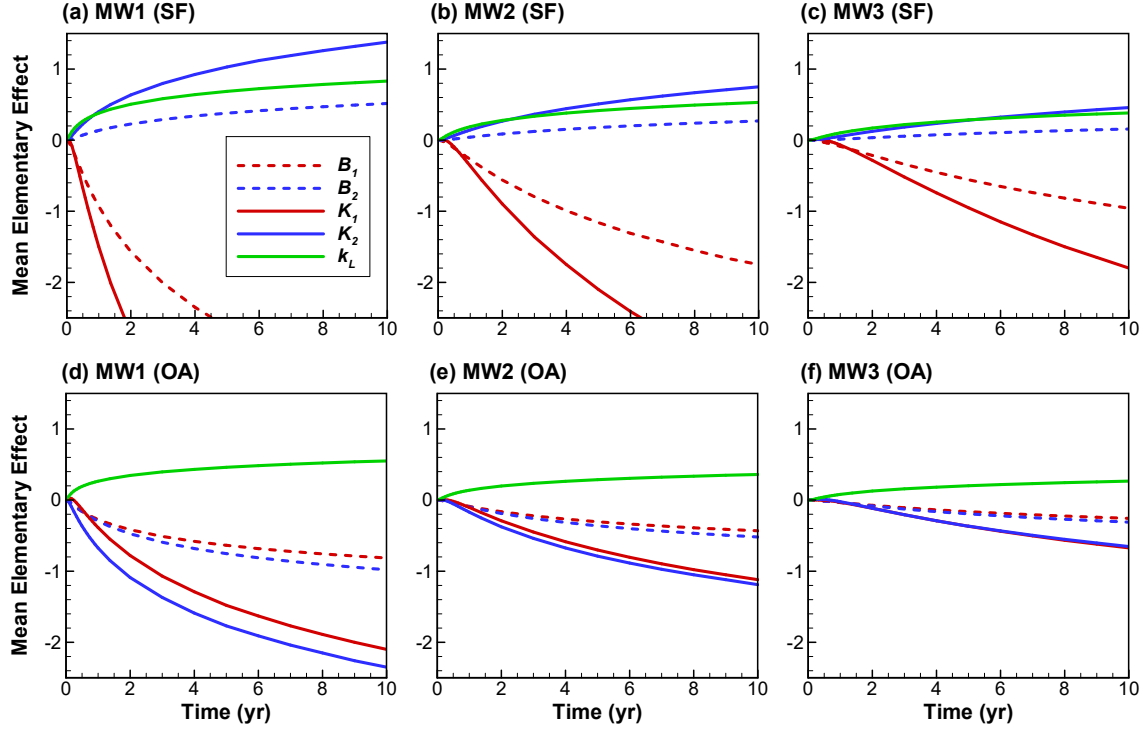
Figure 6: Transient mean elementary effect (EE) of the pressure anomaly in both the storage formation and the overlying aquifer at three different monitoring-well locations (MW1, MW2, and MW3).

2.4.3 Analysis of Detectability of Pressure Anomalies

Detectability analysis addresses the question whether and under which conditions leakage signals are sufficiently anomalous to be observable. In particular, this study was interested in determining the detection time T_D (the start time that the leakage signal at an observation point becomes larger than the detection limit) and the detection region (the area around a leaky well where the leakage signal at a given time becomes larger than the detection limit). That is, the detectability analysis aims to answer the following questions: (1) whether it is possible to detect leakage signals at available observation points, in consideration of measurements errors and detection limits; (2) what the detection time is and how the leakage signals at an observation point evolve with time; (3) how the detection region evolves with time; and (4) how the detection time and region are affected by variations in formation parameters and leaky well permeability and location. Based on the instrument measurement errors for pressure sensors and natural pressure variability expected in deep formations (Benson, 2006), a pressure anomaly detection limit of 0.1 bar was selected. For surface-deformation anomaly, a detection limit of 1 mm was selected assuming that currently available InSAR technology was applied.

Figure 7 shows the leakage-induced pressure anomalies Δh_{w-wo} in the overlying formation as a function of time, for five monitoring well locations that are, respectively, 0.1, 0.5, 1, 2, and 5 km away from the leaky well. With focus on the most sensitive parameter identified in the sensitivity analysis, detectability analysis was conducted for three different values of the hydraulic conductivity of the storage formation (K_1= 0.02, 0.2, and 2.0 m d⁻¹). Since the leaky well

permeability is unknown before well leakage detection but has a significant impact on the pressure anomalies, detectability was also evaluated for two different values of the leaky well permeability. All other parameters are the base-case values given in Table 1. As expected, the strength of the well-leakage signals depends on the distance of an observation point from the leaky well and on the hydraulic conductivity of the storage formation (see Figure 7). All Δh_{w-wo} values increase with injection time.
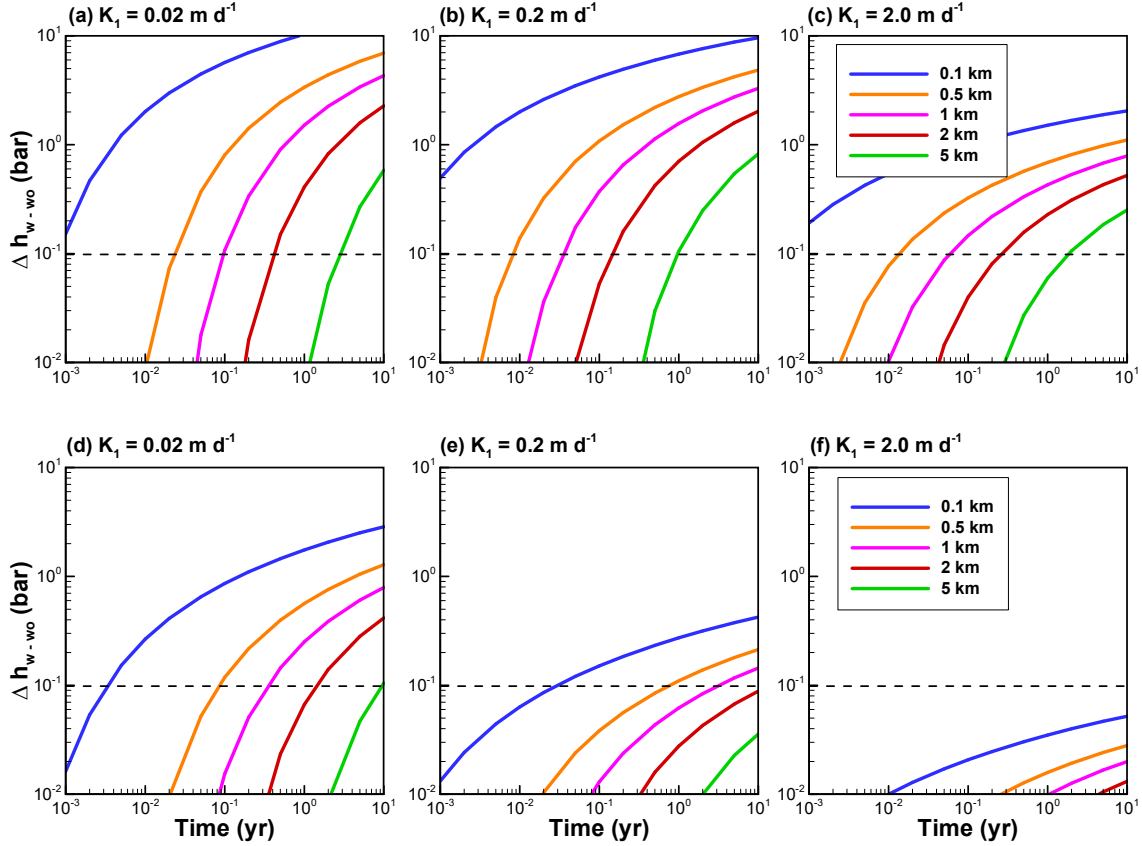
Figure 7: Leakage-induced pressure anomaly (Δh_{w-wo}) in the overlying aquifer at different monitoring-well locations (0.1, 0.5, 1, 2, and 5 km away from the leaky well), as a function of aquifer hydraulic conductivity (K_1= 0.02, 0.2, and 2.0 m d^{-1}) and leaky well permeability (k_L = 2 × 10^{-7} m^2 in the upper panel, and k_L = 2 × 10^{-10} m^2 in the lower panel). The dashed line represents the detection limit of pressure anomaly (= 0.1 bar).

In the high leaky well permeability case (k_L = 2 × 10^{-7} m^2), the signal strength increased to sufficient values (above the detection limit) at all monitoring well locations. For the base-case reservoir conductivity (K_1 = 0.2 m d^{-1}, Figure 7b), the pressure anomalies can be detected within 1 year at all observation points, even at the most distant one (5 km away from the leaky well). In the case of K_1 = 0.02 m d^{-1} (Figure 7a), the detection time was slightly delayed, because the pressure propagation was slower than that in the base case. However, the pressure anomalies at the observation points relatively close to the leaky well were more significant than those in the

base case as a result of higher leakage rates. The case with a higher reservoir conductivity of K_1 = 2.0 m d^{-1} (Figure 7c) shows the opposite trend, slightly faster detection, but overall smaller signal strength.

When the permeability of the leaky well is smaller (i.e., $k_L = 2 \times 10^{-10}$ m^2), the pressure anomalies become weaker, both in terms of signal strength and delay of signal. In the base case, it takes about 1 year to have detectable pressure anomalies when the leaky well is located 0.5 km away, and Δh_{w-wo} is below the detection limit for the entire 10 years of injection/monitoring if the sensor is 2 or 5 km away from the leaky well (see Figure 7e). In the higher hydraulic conductivity case ($K_1 = 2.0$ m d^{-1}, Figure 7f), the pressure anomaly in the overlying aquifer is too small to detect even at a very close distance to the leaky well. That is, a pressure-based early leakage detection method can only be successful if the well permeability is large and the leakage rate is substantial.

Figure 8 quantitatively assesses the detection region ($\Delta h_{w-wo} \geq 0.1$ bar) in the overlying formation as a function of injection time, reservoir conductivity, and leaky well permeability. For the base case, this region at a given injection time is illustrated by the contour line of $\Delta h_{w-wo} = 0.1$ bar centered at the leaky well (see Figure 8a). If a monitoring well is located within this region, the pressure anomaly measured at time T_D is detectable. The size of the detection region and its temporal trends depend on the hydraulic conductivity of the aquifer (Figure 8b). The detection region in the case of $K_1 = 0.02$ m d^{-1} is smaller than that in the case of $K_1 = 0.2$ m d^{-1} because of the slower pressure propagation. On the other hand, in the case of $K_1 = 2.0$ m d^{-1}, the pressure changes quickly propagate, but the changes themselves are not as strong, resulting in the slower increase of the detection region.
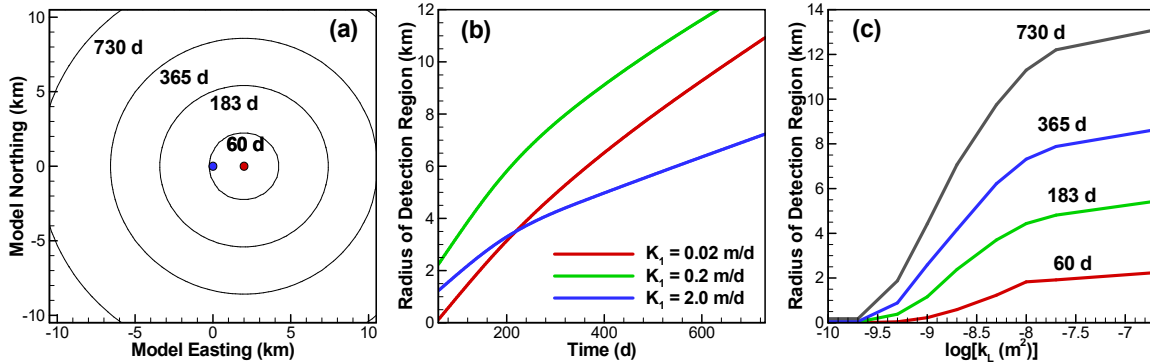
Figure 8: (a) Time-dependent detection region in the overlying aquifer, defined by contour lines of $\Delta h_{w-wo} = 0.1$ bar in the base-case condition, (b) changes in radius of the detection region over time for different aquifer hydraulic conductivities ($K_1 = 0.02$, 0.2, and 2.0 m d^{-1}), and (c) changes in radius of the detection region as a function of the leaky well permeability at different times.

In addition, the detection region is greatly affected by the leaky well permeability; the detection region at a given time shrinks considerably with decreasing leaky well permeability (Figure 8c). This becomes quite obvious when the leaky well permeability is small. For example, in the case

of $k_L = 2 \times 10^{-10}$ m², the detection region at 10 years of injection time is only 1.3 km in radius (not shown). Correspondingly, the maximum leakage rate is 595 m³/d (10.4% of the injection rate) in the case of $k_L = 2 \times 10^{-7}$ m², and 26 m³/d (0.5% of the injection rate) in the case of $k_L = 2 \times 10^{-10}$ m². In this latter case, it is unlikely for early leakage detection to be successful because (1) the detection region is too small to have a monitoring well near the unknown leaky well and (2) the detection time is too long to provide information about well leakage early enough. It is worth noting that further increases in the detection region are not significant for leaky well permeabilities higher than 10^{-8} m². This indicates that the leakage rate and the corresponding pressure anomaly become less sensitive to leaky well permeability once the permeability is sufficiently large. The effect of this moderate sensitivity on estimation of the leaky well permeability is further discussed in the next section.

2.5   CONCLUSIONS

Current techniques for CO_2 leakage detection are based on the physical, geophysical, or/and geochemical signatures that are induced by migrating CO_2 and that can be observed in the deep and shallow subsurface, at the land surface, and in the atmosphere. Many of these techniques have relatively low spatial resolution and coverage, in comparison to the footprint of CO_2 plumes, and all these techniques can only detect anomalous CO_2 signals long after CO_2 leakage has first occurred.

To provide an early indication of potential CO_2 leakage before it occurs, a concept and framework of early leakage detection was proposed. The framework of the early leakage detection consists of four key components: site characterization for known surface faults and abandoned wells, early detection of brine leakage via inversion of pressure and surface deformation, CO_2 leakage prediction and monitoring, and decision-making for risk management and mitigation.

The basic idea of using pressure and surface-deformation anomalies for early detection of potential CO_2 leakage is based on the fact that leakage-induced pressure signals travel much faster than the migrating CO_2; thus such anomalies may be detected early enough for risk management measures taking effect in avoiding substantial CO_2 leaks. The early detection methodology involves automatic inversion of anomalous brine leakage signals with efficient forward pressure and surface-deformation modeling tools to estimate the location and permeability of leaky features in the caprock. A global sensitivity analysis was conducted to better understand under which conditions pressure anomalies can be clearly identified as leakage signals, and evaluated signal detectability for a broad parameter range considering different detection limits and levels of data noise.

3. DEMONSTRATION OF EARLY LEAKAGE DETECTION METHODOLOGY

In this section, the methodology for early leakage detection developed in Section 3 is applied to four examples with idealized systems of homogeneous storage formation, caprock, and above zone or overlying aquifer (see Figure 9). Because this study was only interested in the single-phase brine flow for methodology demonstration, the semi-analytical solutions are used to calculate pressure and surface deformation. The first three examples (Section 3.1, 3.2, and 3.3) are used to demonstrate the leakage detection using pressure data only, with small pressure data noises, with large data noises, and with errors in rock properties, respectively. For these examples, the model setup and base-case parameters have already been described in Section 2.4.1. Figure 9 shows the location of several monitoring wells used for leakage detection in varying combinations. The last example (Section 3.4) is used to demonstrate the leakage detection using both pressure and surface-deformation monitoring data.
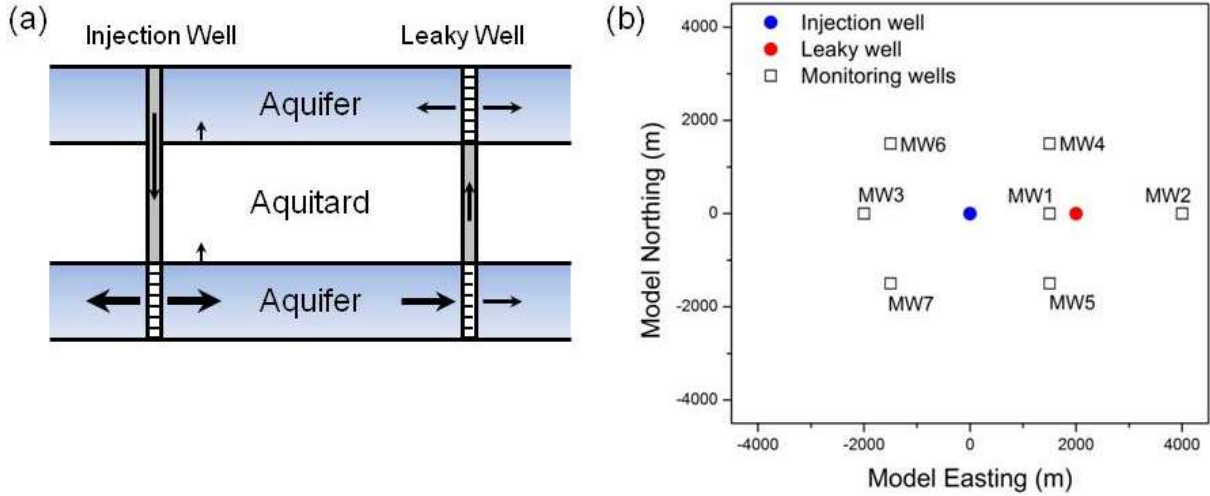
Figure 9: An idealized storage system consisting of a storage formation, a caprock (aquitard), and an overlying aquifer bounded by impervious boundaries at the top and the bottom, with an injection well and a leaky well (2 km apart), in (a) the vertical section along the injection and the leaky well, and (b) a plan view with the locations of the monitoring wells used in sensitivity analysis and inverse modeling.

3.1 WELL LEAKAGE DETECTION WITH SMALL PRESSURE DATA NOISE

In Example 1, the success and accuracy of the inversion methodology is investigated for different monitoring scenarios with varying number and locations of monitoring wells (see Table 2), with single-well monitoring Cases S1 and S2 and two-well monitoring Cases D1, D2, and D3. The monitoring wells that are investigated in different combinations of single-well and dual-well scenarios are MW4, MW5, MW6, and MW7 in Figure 9b at [1.5 km, 1.5 km], [1.5 km, -1.5 km], [-1.5 km, 1.5 km], and [-1.5 km, -1.5 km], respectively.

In the first two monitoring scenarios (S1 and S2 in Table 2), with pressure monitoring at only one monitoring well and the injection well, the success of the leaky well location search depends strongly on the initial guess. Generally, the detection is more successful when the initial guess is

closer to the actual leaky well location. In Case S1, where the monitoring well is located at [1.5 km, 1.5 km], the three initial leaky well location guesses at [1 km, 1 km], [1 km, -1 km] and [-1 km, -1 km] produce the exact location of the leaky well [2 km, 0 km], while the initial guess of [-1 km, 1 km] produces a wrong location at [0 km, 2 km]. All inverse solutions arrive at the correct permeability of the leaky well. The match between the simulated and the measured pressure anomalies is excellent regardless of the estimated location, indicating that the two estimated locations are non-unique solutions of the detection problem with one monitoring well. These findings are similar in Case S2 where the monitoring well is located at [-1.5 km, 1.5 km]. Again, two locations, [0 km, -2 km] and [2 km, 0 km], are identified as possible solutions, the leaky well permeability is accurately calibrated, and the match between the simulated and the measured anomalies at the monitoring locations is perfect.

Table 2: Number of monitoring wells (MWs) and their locations in different monitoring scenarios and detection of the leaky well using only pressure anomalies with small data noise

| Case | # of MWs | MWs | | Initial guesses | | | |
		Location [X (km), Y (km)]	Names	Run1	Run2	Run3	Run4
S1	1	[1.5, 1.5]	MW4	Y	Y	N	Y
S2	1	[-1.5, 1.5]	MW6	Y	N	Y	Y
D1	2	[1.5, 1.5], [1.5, -1.5]	MW4, MW5	Y	Y	Y	Y
D2	2	[1.5, 1.5], [-1.5, 1.5]	MW4, MW6	Y	Y	Y	Y
D3	2	[1.5, 1.5], [-1.5, -1.5]	MW4, MW7	Y	N	N	Y
D3-1	2	[1.5, 1.5], [-1.0, -1.5]	MW4, MW7	Y	Y	N	Y
D3-2	2	[1.5, 1.5], [-0.5, -1.5]	MW4, MW7	Y	N	N	Y

With two monitoring wells (Cases D1 and D2), the inverse model uniquely and accurately estimates the correct leaky well location at [2 km, 0 km] and also finds the correct leaky well permeability, regardless of the initial guess. This indicates that the well leakage detection problem in Cases D1 and D2 has a unique solution. In contrast, when the two monitoring wells and the injection well are aligned as shown in Figure 9b (Case D3, with M4 and M7 as monitoring wells), the detection problem does not have a unique solution; i.e., the leaky well location is correctly estimated in two of the four initial guesses. In all runs, however, the estimated well permeability is correct. Note that this non-uniqueness in Case D3 is resolved by using both pressure and deformation data, which is discussed in Section 3.4.4.1.

The comparison of the detection results in these three cases indicates that it is important to appropriately arrange monitoring wells with respect to the injection well in order to accurately detect a leaky well and enhance the inversion accuracy. The topography of the objective function supports this difference in performance. Figure 10 shows the contours of the objective function in the parameter plane of the easting and northing of the estimated leaky well location at $k_L = 2 \times 10^{-7}$ m^2. The inverse modeling finds the global minimum of the objective function in Cases D1 and D2 (see Figures 10a and 10b). However, the inverse problem has two global minima in Case

D3 (see Figure 10c), explaining the dependency of the leakage detection on the initial guess of well location.
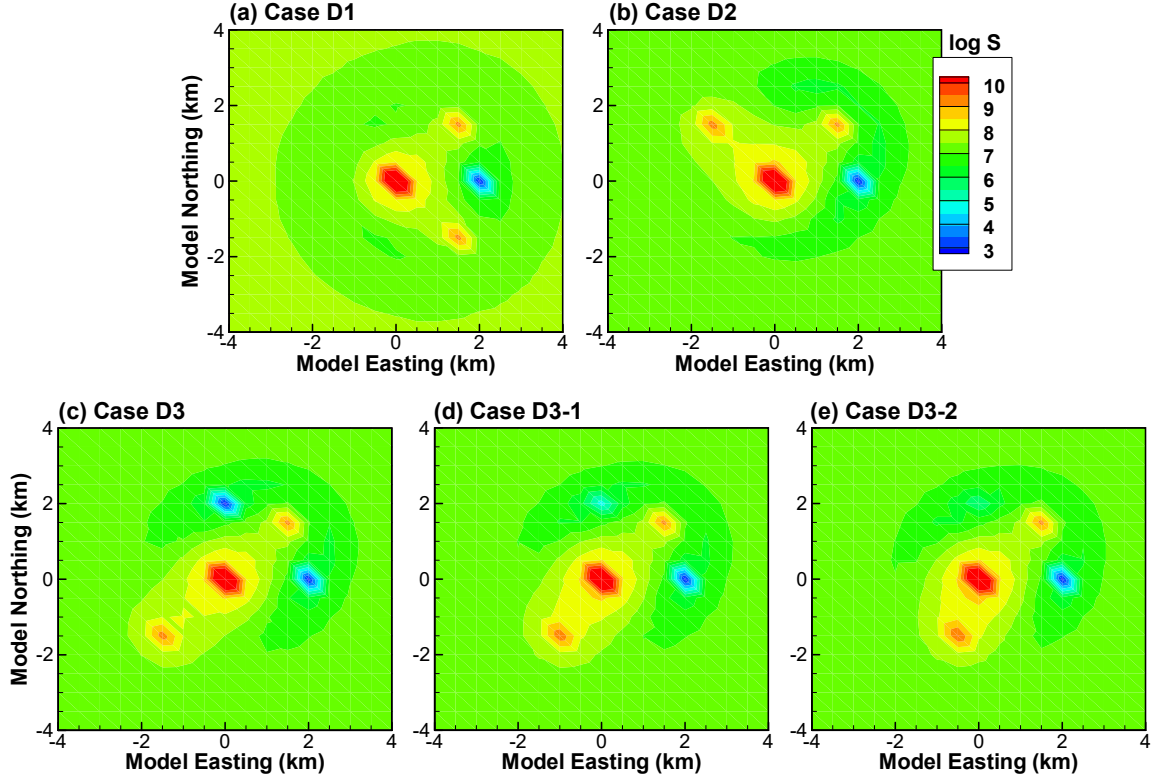
Figure 10: Contours of the objective function *S* in the parameter plane of the easting and northing of the leaky well. The plane intersects the parameter space at $k_L = 2 \times 10^{-7}$ m².

Above monitoring scenarios all involve a regular well configuration. The inverse model in these cases detects either the leaky well or an "image" well (relative to the straight line along the injection and the monitoring well) and accurately calibrates the leaky well permeability, thus producing an excellent match between the actual and the estimated pressure anomalies (see Figure 11a). Two additional monitoring scenarios (Cases D3-1 and D3-2 in Table 2) were investigated with arbitrary locations of the two monitoring wells. In these cases, the inverse model accurately estimates both the well location and well permeability in two or three out of the four initial guesses; in other words, the search algorithm accurately finds the global minimum of the objective function shown in Figures 10d and 10e. For the failed trials, the estimated leaky well location does not coincide with the image well location. For instance, in Case D3-2 with the initial guess of [-1 km, - 1 km], the estimated leaky well location is at [-1.2 km, 1.1 km] and the estimated permeability of the leaky well is $k_L = 4 \times 10^{-6}$ m², implying that the search algorithm is not able to find the global minimum due to the presence of multiple local minima. In Cases D3-1 and D3-2, unless the leaky well location and permeability is correctly estimated, the simulated pressure anomalies are systematically lower or higher than the measured ones (see Figures 11b and 11c), indicating the misfit between the model and the observed data is not appropriately appraised. In addition, the marginal standard deviation of the estimated parameters increases for the failed trials, and the increase is particularly notable in the leaky well permeability. Such plots shown in Figure 11 may be useful in evaluating the accuracy of the inverse solution. If

discrepancies remain between the actual and the estimated pressure anomalies, the leaky well location and permeability should either be re-calibrated using different initial guesses of the well location, or more sophisticated global minimization algorithms should be used.

In all monitoring scenarios, the pressure anomalies measured at the monitoring locations are sufficiently large ($\Delta h_{w-wo} > 0.1$ bar) within 0.5 years of fluid injection. With small data noise, the pressure anomalies observed at an early stage of injection are sufficiently strong and clear to accurately detect the leaky well. In the failed cases, the misfit between the model prediction and the measurements is evident, which allows easy detection of unsuccessful inversion. This suggests that early leakage detection can be achieved through inverse modeling of pressure anomalies in cases where noise in pressure monitoring data is small and the calibrated formation parameters are accurate.
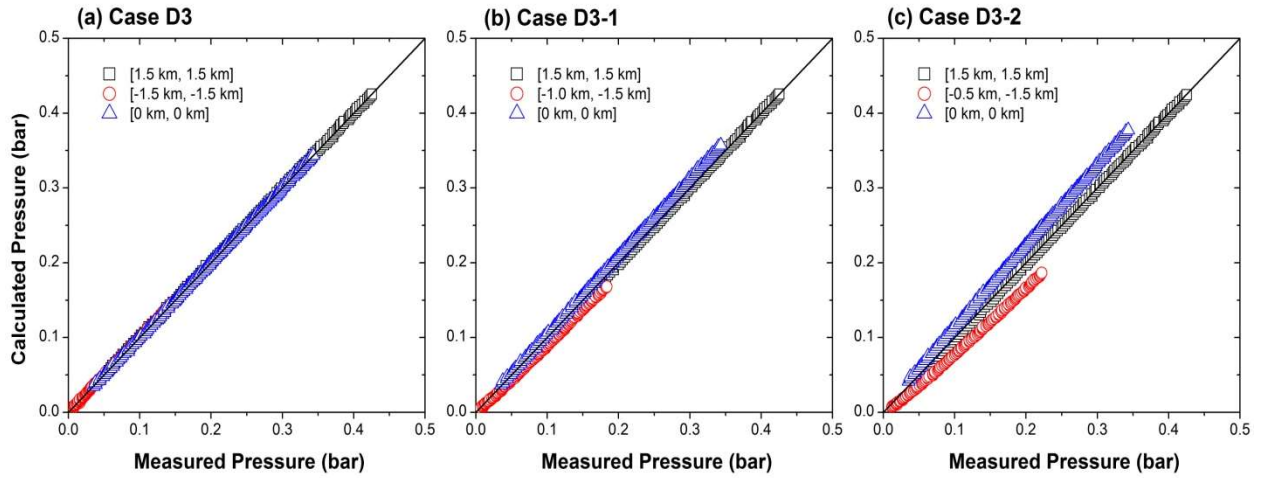
Figure 11: Comparison between the actual pressure anomalies (data) and the estimated pressure anomalies in the overlying aquifer in the monitoring scenarios: (a) Case D3, (b) Case D3-1, and (c) Case D3-2. Shown are the pressure-anomaly values at the injection well (= [0 km, 0 km]) and two monitoring wells. The location of the initial guess is at [-1 km, 1 km] and the estimated leaky well location is [0 km, 2 km] in all cases. The solid line is the unit-slope line.

3.2 WELL LEAKAGE DETECTION WITH LARGE PRESSURE DATA NOISE

In Example 2, Cases D1 and D2 (with two monitoring wells) were used to test the inverse modeling method for pressure data with large data noise. In particular, the effect of incremental monitoring (and injection) duration on the accuracy and convergence speed of leakage detection was examined. Figure 12 shows the estimated leaky well location and estimated well permeability when pressure-anomaly data of the incremental monitoring periods of 1, 2, 3, and 6 years are used. In Case D1, it was observed that even with large data noise the estimated leaky well location is already fairly accurate [1.8 km, ~0 km] at the end of the first year; it converges to [2 km, ~0 km] by the end of the third year. In Case D2, the estimated leaky well location is inaccurate during the first few years, but eventually converges to the true solution with 6 years of monitoring data available. This different behavior can be attributed to the spatial configuration of

the monitoring wells. In Case D1, the two monitoring wells are both 1.6 km away from the leaky well, while in Case D2 one well is at a distance of 1.6 km and the other at a distance of 3.8 km. Due to the relative proximity of the monitoring wells in Case D1, the anomalies in the pressure data are sufficiently strong even when taking into account large data noise.
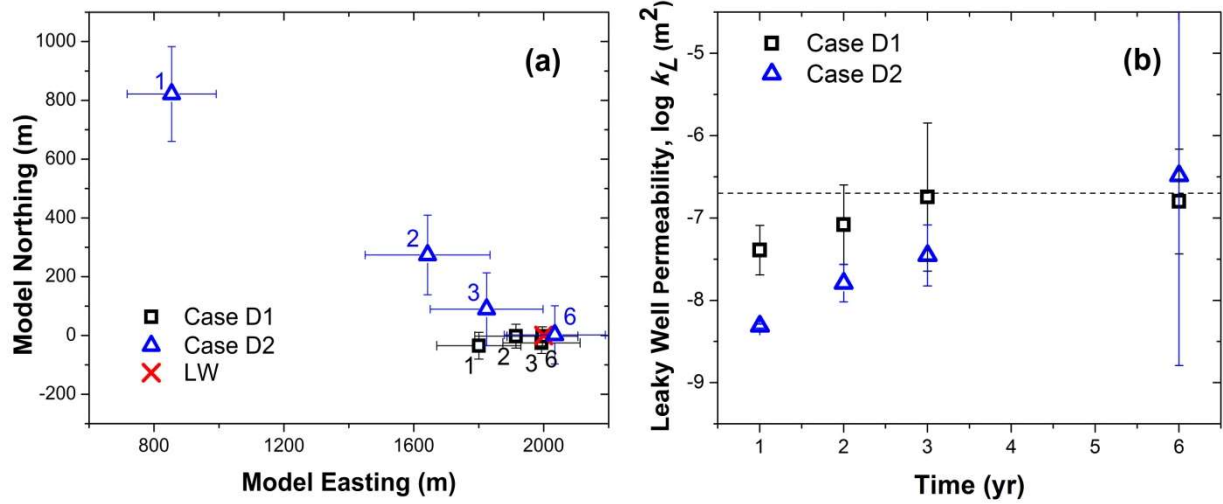
Figure 12: Convergence of (a) estimated location and (b) estimated permeability of the leaky well using the incremental pressure-anomaly datasets of 1, 2, 3, and 6 years in two different monitoring scenarios (Cases D1 and D2 in Table 2). Also shown are the marginal standard deviations of the estimated leakage parameters. In Figure 12a, the number on each point represents the end year of the incremental monitoring period.

The estimated leaky well permeability values follow a trend of increasing accuracy with time that is similar to that of the estimated locations (see Figure 12b). For instance, the leaky well permeability at the end of the first year is off by almost one order of magnitude (Case D1) or two orders of magnitude (Case D2), but converges to the true value (or close to the true value) after 3 and 6 years, respectively. That is, in the early monitoring and inversion stages, the inversion result may not only estimate a wrong leakage location, but may also infer an inaccurate leaky well permeability, which means that the potential magnitude of leakage would be incorrectly assessed (in Cases D1 and D2, it would be underestimated). It is interesting to note that the marginal standard deviation of the estimated leaky well permeability actually increases with time, a trend opposite to the improving accuracy of the permeability estimate. This might be due to the reduced sensitivity of the leakage rate (and the resulting pressure anomaly) to leaky well permeability at high permeabilities.

3.3 WELL LEAKAGE DETECTION WITH MODEL CALIBRATION ERRORS

Examples 1 and 2 assumed that the forward model used in the inversion scheme for pressure and surface-deformation anomalies is able to predict the "expected" behavior of the storage system without any error or uncertainty; in other words, all formation parameters are known and the only unknown parameters in the inversion scheme are the location and permeability of the leakage pathways. In practice, however, the forward model may not be "perfect" to accurately predict the pressure evolution profiles, because: (1) the data on site characterization and field

tests prior to CO_2 injection are insufficient to perfectly calibrate a forward model; (2) multiscale heterogeneity of hydrogeological properties affects the pressure responses in a complicated way that can never fully be known; and (3) the field data used for model calibration may already comprise signatures of unknown leaky pathways near the injection zone. Since a small error in the model parameters can have more significant impact on identifying leakage pathways than measurement noise, more complex inversion problems were tested in which not only the leakage parameters are unknown but also relevant formation parameters are uncertain. The errors stemming from uncertain model parameters are accounted for by including those model parameters as the parameters to be estimated during the inversion procedure and simultaneously estimating them with leakage parameters.

In Example 3, it was assumed that the hydraulic conductivity (K_2) and specific storativity (S_2) of the overlying aquifer include 50% error, assuming that no site-specific data are available and initial guesses need to be based on the literature. It was furthermore assumed that the hydraulic conductivity (K_1) and specific storativity (S_1) of the storage formation have been estimated from a pumping test conducted before CO_2 injection so that uncertainty is smaller. The monitoring well used is located 100 m away from the injection well. The estimated K_1 and S_1 are 9.78E-2 and 2.14E-6, and are 2.2% underestimated and 13.8% overestimated, respectively.

Figure 13 shows the pressure evolution "measured" in the storage formation and the overlying aquifer at MW4 along with the initial "calculated" model prediction. Since this is a synthetic example, the "measured" evolution is based on executing the forward model with the leaky well and the actual model parameters. The "calculated" model predictions is also conducted with the forward model, but incorporating the errors in the model parameters and not accounting for the leaky well (since it is unknown). The pressure increases in the storage formation are rapid and strong, and those in the overlying aquifer are delayed and much more moderate, which is shown in the inset figure in Figure 13b. This inset figure provides a close look of the first year of monitoring, and it takes about 50 days to observe a sufficiently large pressure buildup in the overlying aquifer that can be considered as leakage signal. Even though the model does not take into account the leaky well and includes some errors in the model parameters, the model prediction seems to be sufficiently close to the measured data in the storage formation up to about 1 year, and the deviation from the measurements becomes distinct after that. On the other hand, the model prediction in the overlying aquifer is clearly off from the measured data since in our model condition, the diffuse leakage alone cannot result in sufficient pressure buildup in the overlying aquifer within the given time frame. Therefore, the presence of a leaky pathway can be hypothesized from this pressure anomaly observed in the overlying aquifer.
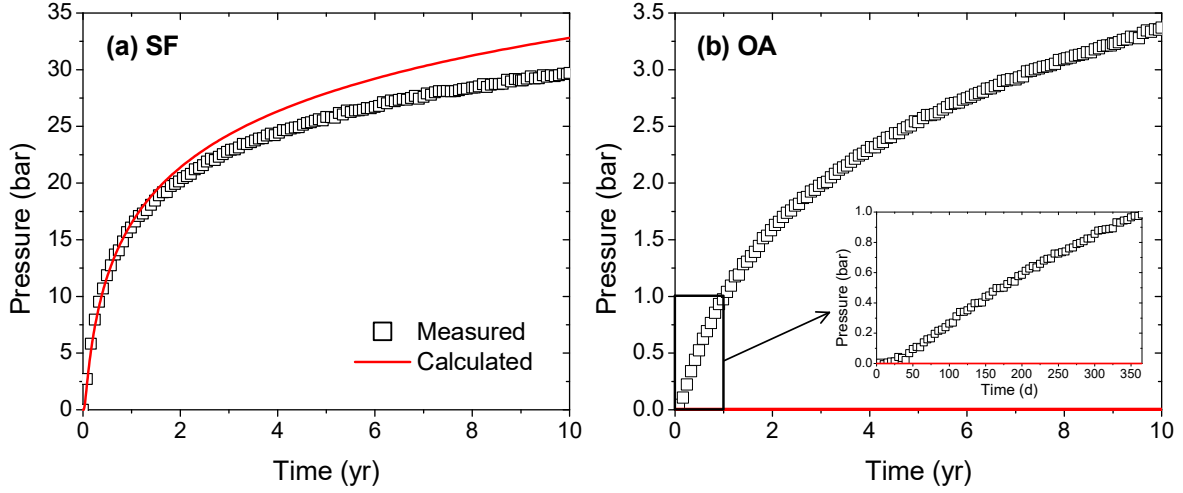
Figure 13: Pressure buildup in (a) the SF and (b) the OA at MW4.

Figures 14 and 15 show the estimated leaky well location and permeability when the uncertain model parameters K_1, K_2, S_1, and S_2 are also included as the parameters estimated through the inversion. The pressure data of the incremental monitoring periods of 1, 2, 3, and 6 years are used. The two cases, i.e., (a) only using the pressure data in the overlying aquifer (Case E1), and (b) using the pressure data in both the overlying aquifer and the storage formation (Case E2) are compared in terms of the accuracy and convergence speed of leakage detection. Also, among four different initial guesses, the results of RUN1 and RUN4 are presented.

In Case E1, the estimation of the leaky well location improves with time, but either has high standard deviations (RUN1) or is still inaccurate (RUN4). In Case E2, it was observed that the estimated leaky well location converges close to the actual location as the monitoring period increases. Particularly, for RUN4, the estimated location has converged to the true location in 2 years. The accuracy of the estimated leaky well permeability also shows the similar trend. With the pressure data only from the overlying aquifer, the accuracy is in generally poorer than that with the data from both the overlying aquifer and the storage formation. In most trials, the estimated value is off by 1–2 orders of magnitude. Moreover, the marginal standard deviation of the estimate is sometimes too large so that the range cannot be shown in Figure 15, in which cases the symbols are marked with an asterisk (*). The sensitivity of the pressure response to the leaky well permeability significantly decreases when the permeability is sufficiently large (i.e., 10^{-8} m^2) (Jung et al., 2013). Thus, the high uncertainty, particularly in the overestimated cases, is not surprising, regarding also the uncertainties in the model parameters.
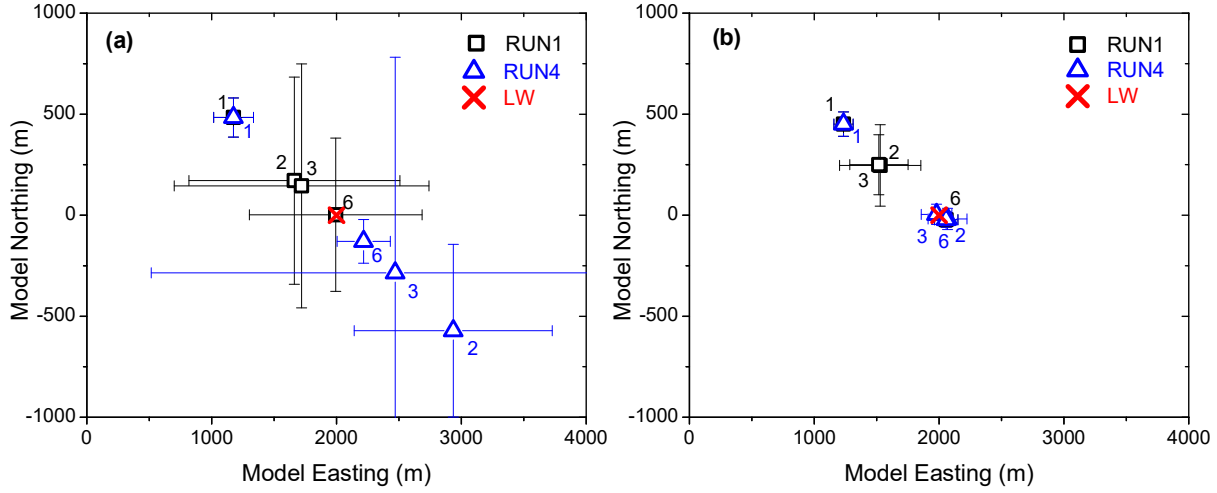
Figure 14: Convergence of the estimated leaky well locations using the incremental pressure monitoring datasets of 1, 2, 3, and 6 years when (a) only using the pressure data in the overlying aquifer, and (b) using the pressure data in both the overlying aquifer and the storage formation. Also shown are the marginal standard deviations of the estimated leakage parameters. The number on each point represents the end year of the incremental monitoring period.
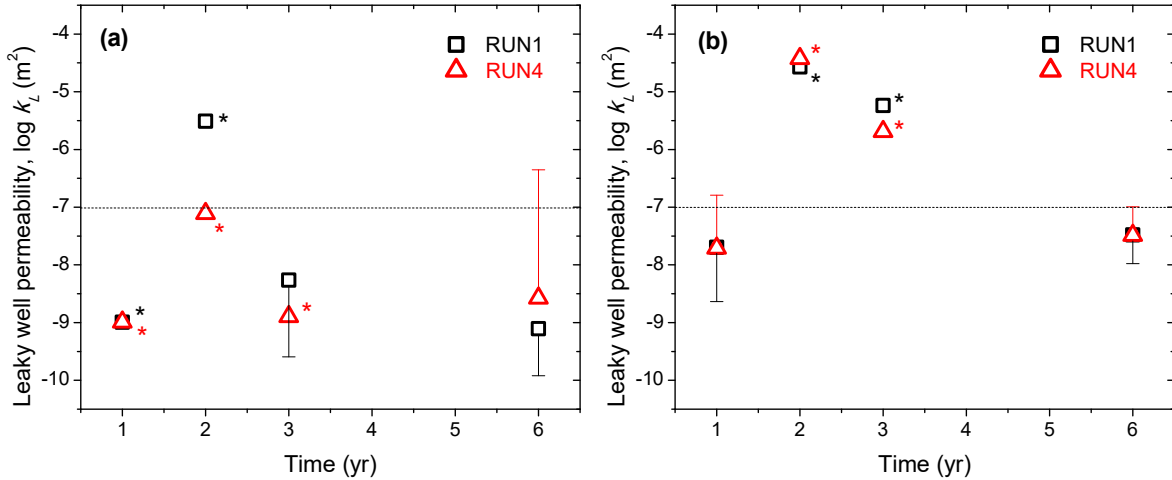
Figure 15: Convergence of the estimated leaky well permeabilities using the incremental pressure monitoring datasets of 1, 2, 3, and 6 years when (a) only using the pressure data in the overlying aquifer, and (b) using the pressure data in both the overlying aquifer and the storage formation. For illustration purpose, only the minus direction of the marginal standard deviation is shown for RUN1, and the plus direction for RUN4. Also, the asterisk symbol (*) means that the marginal standard deviation of the estimate is omitted because it is too large to be included in the figure.

Even though the estimated location and permeability of the leaky well are not accurate in Case E1, the match between the measured and calculated pressure is good regardless of the monitoring time, indicating that the estimates are non-unique solutions of the detection problem. This non-

uniqueness is not favorable for successful risk assessment, and may result in an ineffective management plan. For instance, it is assumed that the leaky well can be located based on the estimated leaky well location in Case E1 with the 6 years of monitoring data. The continuous pressure monitoring after the first 6 years shows that the calibrated model, which now includes the leaky well, accurately predicts the pressure evolution at all monitoring wells. However, due to the inaccurate leaky well permeability, the predicted cumulative leakage is about three times smaller than the actual leakage, and the risk management plan based on this underestimation will not be able to prevent the damage and hazard by excessive leakage.

This hypothetical study shows that (1) the above-zone monitoring is important for the early leakage detection, particularly when the model uncertainties cannot be ruled out, and (2) the model uncertainties can be successfully parameterized and estimated simultaneously with the leakage parameters. It is also important to note that pressure monitoring in the storage formation and its use for the inverse modeling is critical to improve the accuracy and convergence speed of the estimation.

3.4 WELL LEAKAGE DETECTION USING PRESSURE AND SURFACE-DEFORMATION MONITORING DATA

3.4.1 Model Setup and Forward Model

In Example 4, this study attempted early leakage detection using pressure monitoring data *and* surface-deformation data. As explained in Section 2.3.2, the surface deformation is approximated via vertical integration of the pressure-induced volumetric changes in aquifers and aquitards, using Equation 2. Similar to the pressure anomalies, the surface-deformation anomalies due to leakage are obtained by calculating the difference Δb_{w-wo} between the "monitored" system response (induced by both injection and leakage) and the "expected" system response (induced by injection only).

Note that approximate surface-deformation anomalies may cancel out in a storage system like the first three examples where the storage aquifer and the overlying aquifer have similar thickness and compressibility. This is because the volumetric vertical expansion induced by the fluid leakage into the overlying aquifer is similar to volumetric vertical contraction caused by leakage out of the storage formation. In order to examine storage site conditions where leakage-induced surface deformations are detectable, the thickness of overlying aquifer increased from 60 m to 120 m and modified the pore compressibility of the overlying aquifer from 4.5×10^{-10} Pa^{-1} to 18.0×10^{-10} Pa^{-1}. In other words, a less consolidated overlying aquifer is representative of a shallower formation. (For consistency, the caprock thickness also increased to 600 m.) As a result of these modifications, the uplift induced by the fluid leakage into the overlying aquifer is now larger than the leakage-induced subsidence in the storage formation, leading to detectable deformation anomalies at the ground surface. All other model parameters and the configuration of the injection well, the leaky well, and the two monitoring wells in Cases D1, D2, and D3 are the same with the first three examples. The permeability of the leaky well is $k_L = 2 \times 10^{-7}$ m^2.

3.4.2 Detectability of Surface Deformation

To obtain sufficient spatial coverage, the surface-deformation anomalies were calculated with a spatial resolution of 500 m × 500 m at a few selected times of interest during injection and

monitoring. Figures 16a–c show the contours of surface deformation, b_w, at 2, 5, and 10 years after injection starts, respectively. Figure 16d shows how the deformation anomalies, Δb_{w-wo}, evolve as a function of time, using the 1-mm contour line as the cut-off value above which detection is possible. Leakage signals in the surface deformation can be detected as early as 2 years after the start of fluid injection, i.e., the contour lines in Figures 16a–c start deviating from the perfectly circular lines in the case of no leakage. The surface-deformation anomalies in Figure 16d are clearly noticeable. The anomalous signals are centered at the leaky well, and the radius of the signals increases as a function of time. This study concluded that leakage-induced deformation anomalies may be useful for leakage detection as a monitoring tool with dense spatial coverage. However, strong deformation anomalies are expected only for relatively large leakage rates. For instance, in the case of $k_L = 2 \times 10^{-10}$ m², Δb_{w-wo} never exceeds the 1-mm cutoff value during the 10-year injection period.
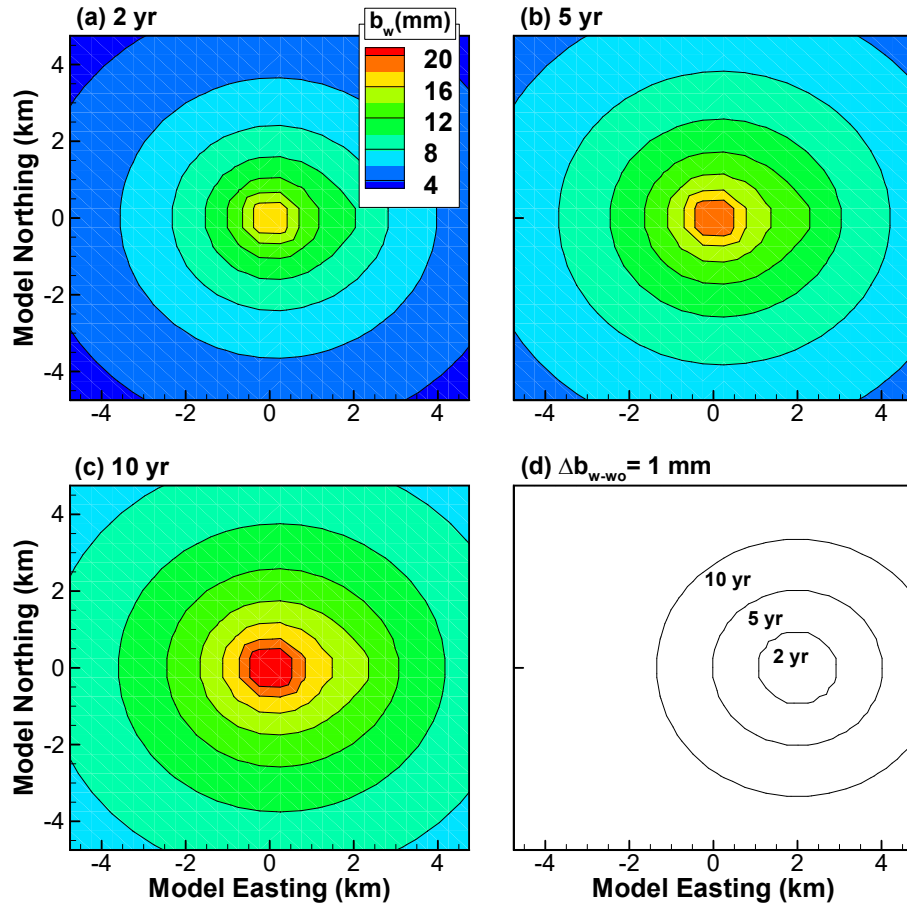
Figure 16: Contour plot of b_w at (a) 2 yr, (b) 5 yr, and (c) 10 yr, and (d) time-dependent contour lines of $\Delta b_{w-wo} = 1$ mm for $k_L = 2 \times 10^{-7}$ m².

3.4.3 Inverse Modeling for Well Leakage Detection

This study assessed the performance of inverse modeling for detecting the leaky well using pressure *and* surface-deformation monitoring data in Cases D1, D2, and D3, and compared the detection results with those using *only* pressure data. Case D3, which is an otherwise non-unique inverse problem when only pressure data are available, was used to demonstrate the improvement in detection capability by jointly inverting for pressure and deformation. Cases D1 and D2 (with large data noise for pressure) were used to demonstrate the enhanced convergence speed. The pressure data noise was introduced to the data in the same way as described in Sections 3.1 and 3.2. Similar to the pressure data noise, the deformation data noise was also introduced to the measured surface-deformation data. Since the pixel size of 500 m × 500 m used for the deformation data is rather large and each pixel contains aggregated information for the inverse modeling, it was assumed the data noise with a small standard deviation of 0.1 mm.

3.4.3.1 Detection with Small Data Noise

In Case D3, when using only pressure data, the solution of the detection problem is non-unique, with the estimated locations depending on the initial guess for the leaky well location. This non-uniqueness is resolved when using both pressure and deformation data. The leaky well location and the well permeability are accurately estimated for all initial location guesses as early as 1 year after fluid injection. This study concluded that surface-deformation data, which provide dense spatial information, can effectively complement pressure data that are typically measured at a limited number of monitoring wells.

3.4.3.2 Detection with Large Data Noise

Figure 17 shows the estimated leaky well location for different incremental monitoring periods for Cases D1 and D2, and compares the inverse modeling results using both pressure and surface-deformation data with the results obtained using only pressure data. In the latter case, the estimated well locations are [1.8 km, ~0 km], [1.9 km, ~0 km], [2.1 km, ~0 km], and [2.1 km, ~0 km] in Case D1, and [0.9 km, 1.2 km], [0.8 km, 1.1 km], [1.9 km, 0.2 km] and [1.1 km, 0.6 km] in Case D2, for incremental monitoring periods of 1, 2, 3, and 6 years, respectively. In Case D2, the estimated location with 6 years of monitoring data is even less accurate than the one estimated using 3 years of monitoring data. In both Cases D1 and D2, the estimated leaky well location is still off from the exact location at [2 km, 0 km] when using up to 6 years of monitoring data. Note that these estimates of the leaky well location are generally less accurate than those in Section 3.2 (Figure 12), which is due to weaker pressure anomalies resulting from the modifications made in terms of pore compressibility and aquifer thickness.
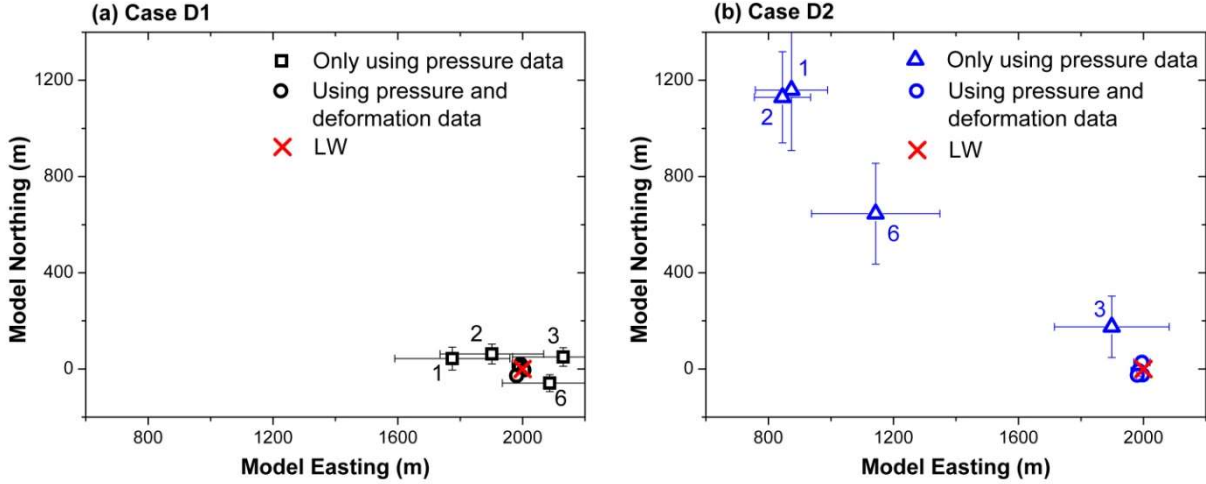
Figure 17: Comparison of the convergence of estimated leaky well locations with increase in incremental monitoring period in (a) Case D1 and (b) Case D2, obtained using inversion of pressure data only and using joint inversion of pressure and surface-deformation data.

In contrast, when both pressure and deformation data were used in the inverse modeling, the leaky well was detected much earlier and more accurately. For example, all estimated well locations were within 34 m from the exact well location [2 km, 0 km] in Case D1, and within 33 m in Case D2 (Figure 17). This clearly shows the advantage of using both pressure and surface-deformation monitoring data for early detection of leakage pathways. In addition, the results of leakage detection are less affected by the suitability of the monitoring well configuration. It should be noted, though, that the successful detection of unknown leakage pathways using surface deformation was achieved here for an idealized storage system and a relatively small detection limit. While this study demonstrates the potential benefit of using surface-deformation data in addition to pressure data, these findings need to be confirmed in real GCS applications.

3.5 CONCLUSIONS

The inversion methodology for early leakage detection was used to estimate leakage parameters (i.e., the location and permeability of the leaky well) in four synthetic examples of idealized two-aquifer-and-one aquitard storage systems, with an injection well and a leaky well, for different monitoring scenarios. In Example 1 with formation parameters and pressure data of no uncertainties and errors, the inversion methodology can produce accurate leakage estimates, no matter whether the detection problem itself is unique or non-unique depending on the number and configuration of monitoring wells. In a random configuration of two monitoring wells, the inversion methodology may need different initial guesses to have accurate estimates of leakage parameters and a best match for pressure data. The detection is stable after the first half year of injection and monitoring.

In Example 2 with two monitoring wells and large pressure data noises, the inversion methodology can improve the estimation accuracy of the leakage parameters with incremental monitoring time and data used in the inversion. The detection accuracy and convergence speed with monitoring time depend on the actual configuration of the two monitoring wells. For an

optimal configuration, an accurate detection can be achieved within the first 2–3 years of monitoring. When the formation parameters are uncertain and the pressure data have large noise (Example 3), the detection accuracy and convergence speed decrease, but can be improved by simultaneously calibrating the formation parameters and leakage parameters using data of pressure anomalies in the overlying formations as well as the storage formation.

As shown in Example 4, joint inversion of pressure and surface-deformation measurements can significantly improve the speed of convergence toward the true solution of the leakage parameters and enable earlier, accurate detection of the location of the leaky well. This example demonstrates how high-resolution deformation data can help identify the leakage location and how the pressure data from a limited number of monitoring wells can help estimate the permeability of a leaky well or the leakage rate.

4. APPLICATION OF EARLY LEAKAGE DETECTION METHODOLOGY TO THE KETZIN SITE IN GERMANY

This section presents an application of the early leakage detection method, developed in Section 2 and demonstrated in Section 3, to the Ketzin CO_2 pilot test site in Germany. This application includes the three components of the framework of the leakage detection system: site characterization, model calibration, and leakage detection (see Figure 4). The leakage detection is demonstrated in Section 4.3 using a hypothetical example with an (assumed) leaky well located at 675 m from the injection well. The model calibration is demonstrated in Section 4.2 using the cross-well pumping tests between one injection and two monitoring wells conducted prior to CO_2 injection. The site characterization is presented in Section 4.1 with well locations, core data, and geologic model.

4.1 SITE CHARACTERIZATION AT KETZIN, GERMANY

The CO_2 pilot test site at Ketzin, Germany, 25 km west of Berlin, is situated in the structure of the Roskow-Ketzin double anticline, and located in the Northeast German Basin between the Northwest German Basin and the Polish Trough (Figure 18).
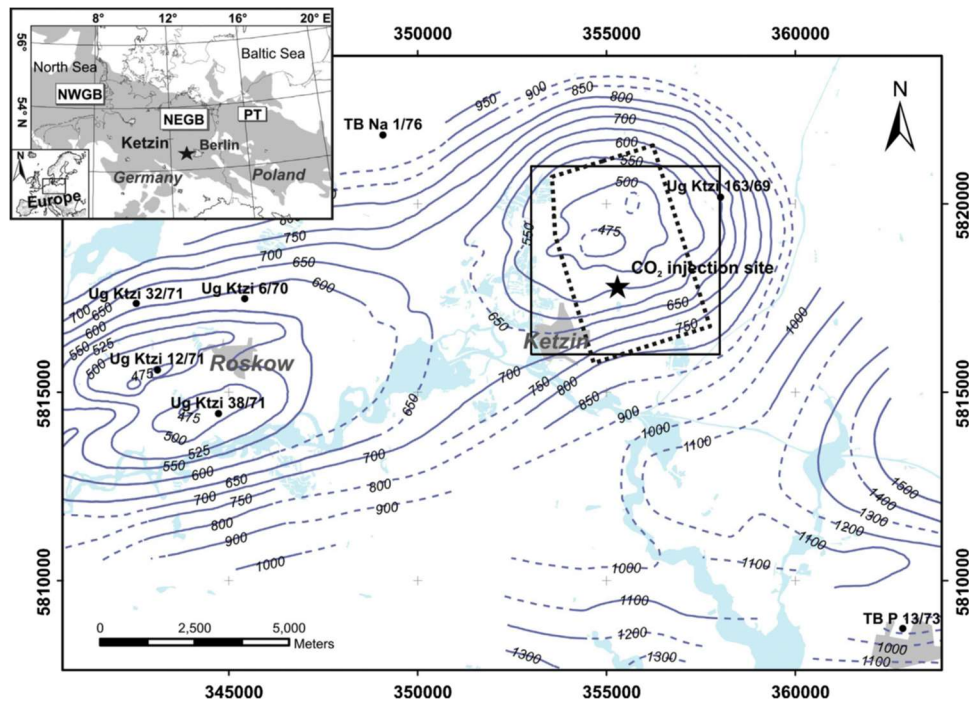
Figure 18: Structure of the Roskow-Ketzin double anticline, highlighted by the isolines (meters below ground level) of the strongest seismic reflector of the Triassic. Shown are the locations of former exploration boreholes penetrating the Stuttgart Formation (dots) and the location of the Ketzin CO₂ boreholes (star), the extension of the 3-D seismic data (stippled black lines), and the geologic model domain size (black square). Inlet map shows the extent of the European Permian Rotliegend Basin (grey-shaded) and the location of the Ketzin site in the Northeast German Basin (NEGB), which is situated between the Northwest German Basin (NWGB) and the Polish Trough (PT) (from Norden and Frykman, 2013).

For the pilot test, one injection well (Ktzi 201) and two monitoring wells (Ktzi 200 and 202) were drilled into the Stuttgart formation (the storage formation), and one shallow monitoring well (P300) was drilled at a depth of 440 m into the Exter formation, whose sandstone layers are collectively called as the "above-zone" for pressure monitoring (Figure 19). P300 has not experienced any pressure anomalies since August 2011 (completion of the drilling), indicating that there is no leakage through the wells. As a result, a hypothetical leakage scenario was formulated for the leakage-detection application by assuming a leaky well is located at 675 m away from the injection well (Section 4.3).
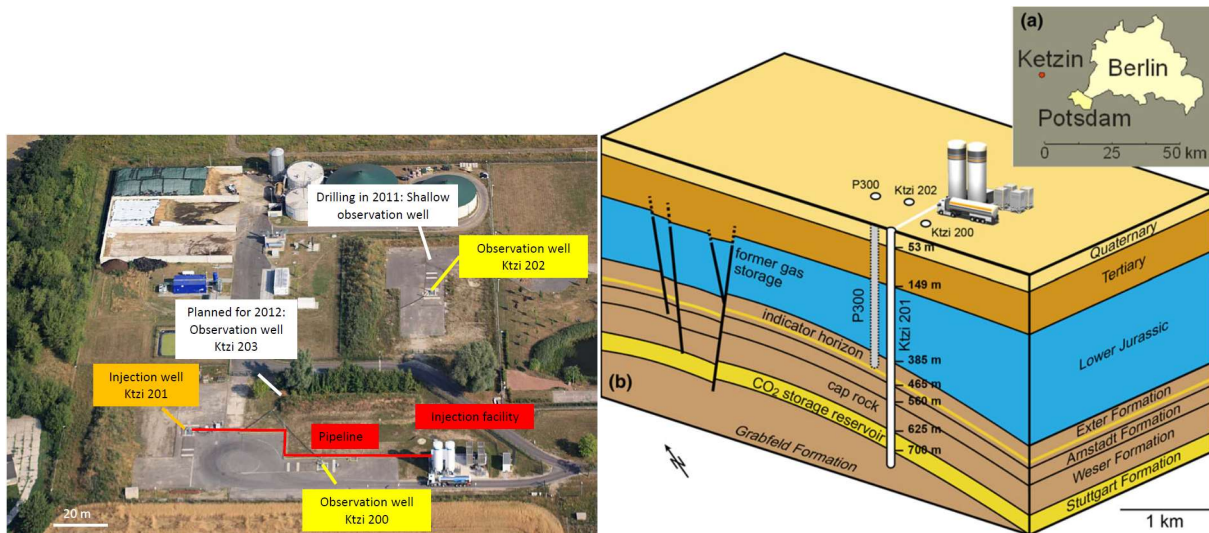
Figure 19: Left shows the facility of CO₂ injection and monitoring at Ketzin, Germany: the injection well (Ktzi 201), the two observation wells (Ktzi 200 and 202) in the Stuttgart formation, the shallow observation well (P300); the right shows the stratigraphic column for the storage formation (Stuttgart), the caprock (Weser and Amstadt) and the above zone (Exter formation) (from Martens et al., 2012).

The site characterization, mainly conducted by Geoforschungszentrum Potsdam (GFZ), includes the drilling, geophysical logging, and coring and measurements, pumping tests prior to CO₂ injection, and development of a 3-D geologic model. Here the nature of the storage formation is briefy described, and the geologic model used for this applictation.

The Stuttgart formation, situated at depths between 630 and 710 m, was selected for CO₂ injection (Förster et al., 2006; Kempka et al., 2010). It is highly heterogeneous in lithology, where sandy string-facies rocks of fluvial origin are alternated with muddy floodplain-facies rocks (Förster et al., 2006; Kempka et al., 2010), reflecting a change in depositional style from playa to fluvial environment (Beutler et al., 1999). In the Stuttgart formation, layers of individual sandstone bodies are stacked into units of several meters thick, forming elongated channel belts (Förster et al., 2010). The lateral extension of the channel belts was estimated to vary from tens to hundreds of meters (Förster et al., 2010; Wurster, 1964). The distribution of the sandstone channels is difficult to predict on a regional scale (Frykman et al., 2006). Above the Stuttgart formation are the Weser and Arnstadt formations that have playa-type facies (Förster et al., 2006; Kempka et al., 2010), which mainly consist of claystone, silty claystone, and anhydrite. These formations have an average thickness of approximately 210 m providing good sealing properties for the CO₂ injection (Förster et al., 2006; Kempka et al., 2010).

Core samples are available from the three boreholes (Ktzi 200, Ktzi 201, and Ktzi 202) drilled into the Stuttgart formation at the Ketzin site (Prevedel et al., 2009). The core analysis (Figure 19) showed sandstone units of up to 9–20 m thickness are located in the top part of the formation and they are considered as typical channel facies; in the lower and middle parts there are sparsely distributed sandstone layers of 0.01–1 m thickness, and are considered as overbank facies (Förster et al., 2010). The thick sandstone units in the top of the formation are further subdivided into two layers with thickness of 5–8 m by a strongly cemented sandstone layer (Förster et al., 2010; Wiese et al., 2010). The core has porosity and permeability varying in large ranges, with the porosity from 5 to >35%, and the permeability from 0.02 to >5,000 mD (Norden et al., 2010). The arithmetic average of the horizontal core permeabilities of the sandstone unit are in a range of 500–1,100 mD (Norden et al., 2010; Wiese et al., 2010). The permeability of the mudstone layer is at the level of microdarcy (Norden et al., 2010; Wiese et al., 2010).
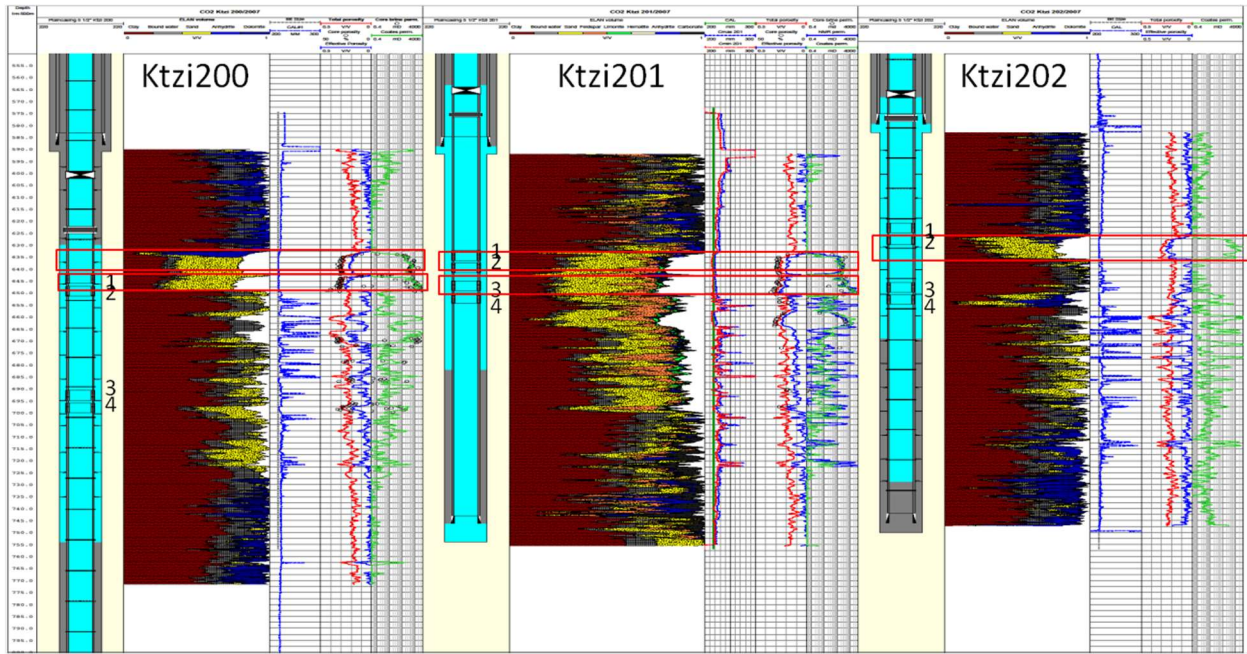
Figure 20: Well configurations, lithological profiles, and measured rock properties of the cores from Ktzi 200, 201, and 202. The first column shows the borehole configuration (Prevedel et al., 2009) with the consolidated casing cements in grey. The second column is the lithological profile (Förster et al., 2010), the third column represents the caliber log, the fourth and fifth columns show the measured porosity and permeability (Norden et al., 2010). The circles refer to measured values from core samples, the green line is the estimated value from Coats equation, and the blue line is the NMR permeability.

The geological model for this simulation study was provided by GFZ. It was generated using a geostatistical approach, based on a collection of measurement data including seismic profiles, stratigraphic and lithological information from boreholes, and CO₂ arrival time (Förster et al., 2006; Kempka et al., 2010). The permeability and porosity distributions used in this application are interpolated from the geological model using the inverse-distance approach.
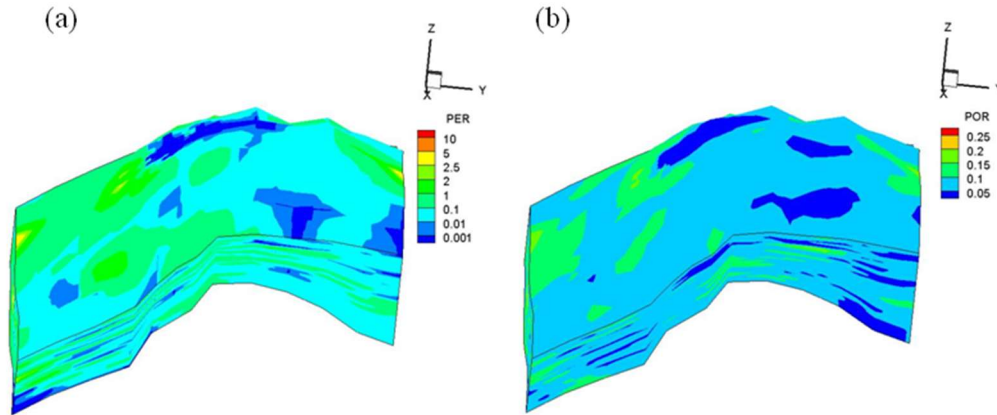
Figure 21: Permeability (a) and porosity (b) distributions in the geologic model.

4.2   MODEL CALIBRATION OF PUMPING TESTS

4.2.1   Pumping Test Data

Pumping tests were conducted in the wells Ktzi 201, Ktzi 200, and Ktzi 202 sequentially from September 2007 to January 2008 (Wiese et al., 2010). Three pumping events have occurred in Ktzi 201. After 10 days, the pumping started in the Ktzi200. The last pumping test was conducted in Ktzi 202 after more than 95 days. Pumping rate varied with time and was recorded during the tests. For each pumping test, pressures were measured simultaneously in the pumping well and two corresponding observation wells (Wiese et al., 2010). Two transducers were installed in the pumping well: one close to the pump and the other (high-resolution gauge) close to the screen (Wiese et al., 2010). Similar drawdown readings were obtained from the two transducers, except in the early stage of pumping (Wiese et al., 2010). Possible explanations for the discrepancy include unstable flow conditions in the early stage, wellbore storage, and the difference in density between the original fluid filled in the wellbore and the formation brine (Zettlitzer et al., 2010). Pressure in the observation wells was measured with a transducer 5–15 m below the water table (Wiese et al., 2010).

The three wells (Ktzi 200, Ktzi 201, and Ktzi 202) form a right triangle, with Ktzi 201 and Ktzi 200 being 50 m apart and Ktzi 200 and Ktzi 202 being 100 m apart (see Figure 22). The boreholes have a diameter of 0.21 m. The casings are 0.12 m in diameter. Pre-perforated sand filter segments were implemented. The wells, however, are completed without cementation in the section of the Stuttgart formation. Thus, the annular spaces provide good connections between the well and the formation layers at different depths. The pumping tests were designed to serve multiple purposes; among them was to remove the drilling fluid from the wellbore and replace it with formation water (Wiese et al., 2010; Würdemann and Zimmermann, 2010). As such, the pumping tests were not optimized for hydraulic tests and packers were not used in the tests.
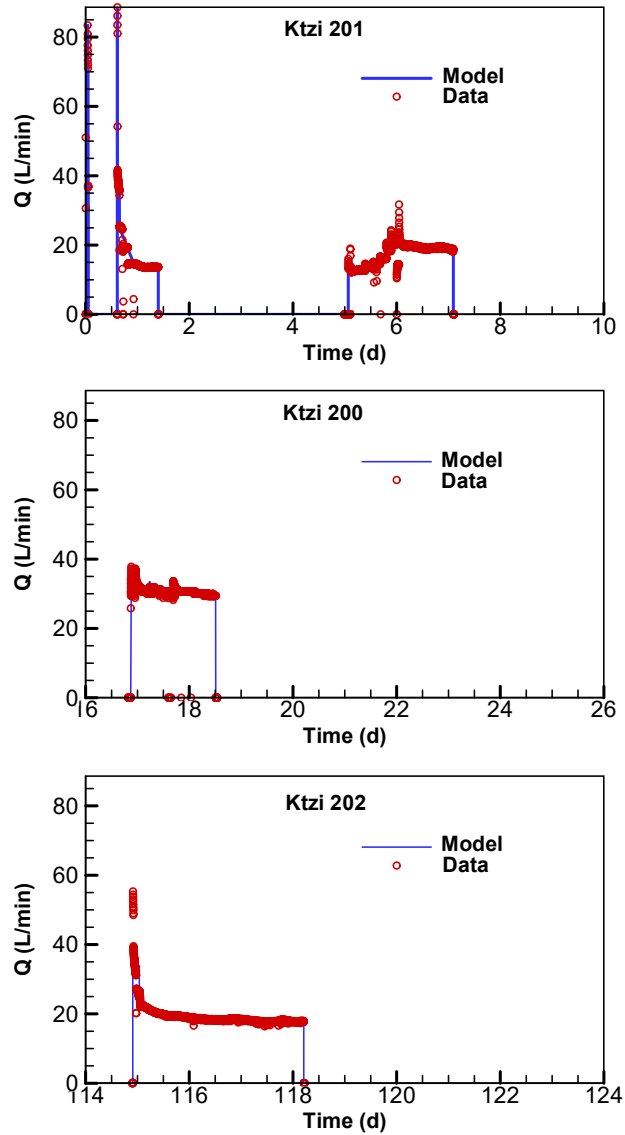
Figure 22: Measured pumping rates and actual value used in model.

4.2.2   Forward Modeling of Pumping Tests

The forward model for the pumping tests was constructed for TOUGH2, using the module EOS9 that solves the Richards equation for isothermal saturated and unsaturated flow (Finsterle, 1999; Pruess et al., 2011). A fluid viscosity of 1.257×10^{-3} Pa·s and a fluid density of 1.157×10^{3} kg/m^3 was assigned to represent the in-situ properties of the formation brine with a salt mass fraction of 0.22 wt% and at 34ºC.

A 3-D mesh covering an area of 1,400 m × 1,400 m was generated using WinGridder (Pan, 2007) (see Figure 23). The well elements have a diameter of 0.21 m, the same as the borehole diameter. To capture the pressure evolution and fluid flow around each well, a radially discretized submesh was created, the radial increments of which increase from 0.108 m to 6 m. This high-resolution submesh that has a radius of 10 m surrounding each well ensures an

accurate simulation of the near-well fluid flow and pressure propagation. The well screens are considered by keeping the horizontal connections of the well elements within the screen intervals. For those elements outside of screen intervals, the horizontal connections are removed and only vertical connections are allowed. Outside of the submeshes are uniform columns of 10 m × 10 m, which are increased to 50 m × 50 m, and then, 100 m × 100 m in the far-field areas. The Stuttgart formation at the Ketzin site has an average thickness of approximately 72 m. In the vertical direction, the mesh covers the whole Stuttgart formation and has a thickness slightly varying spatially, depending on its location in the anticline structure. The core logging data showed a permeable sand layer of approximately 17 m thickness is located in the upper part of the Stuttgart Formation (Norden and Frykman, 2013). To ensure mesh that is fine enough to accurately capture the flow in the sand layer, the top 24 model layers have an average thickness of approximately 1 m. Below the sand layer is the mudstone layer of low permeability. Relatively larger thicknesses are used for these model layers: 3 m for the middle 6 model layers, and 5 m for the bottom 6 model layers. The entire 3-D mesh consists of 47,772 gridblocks.
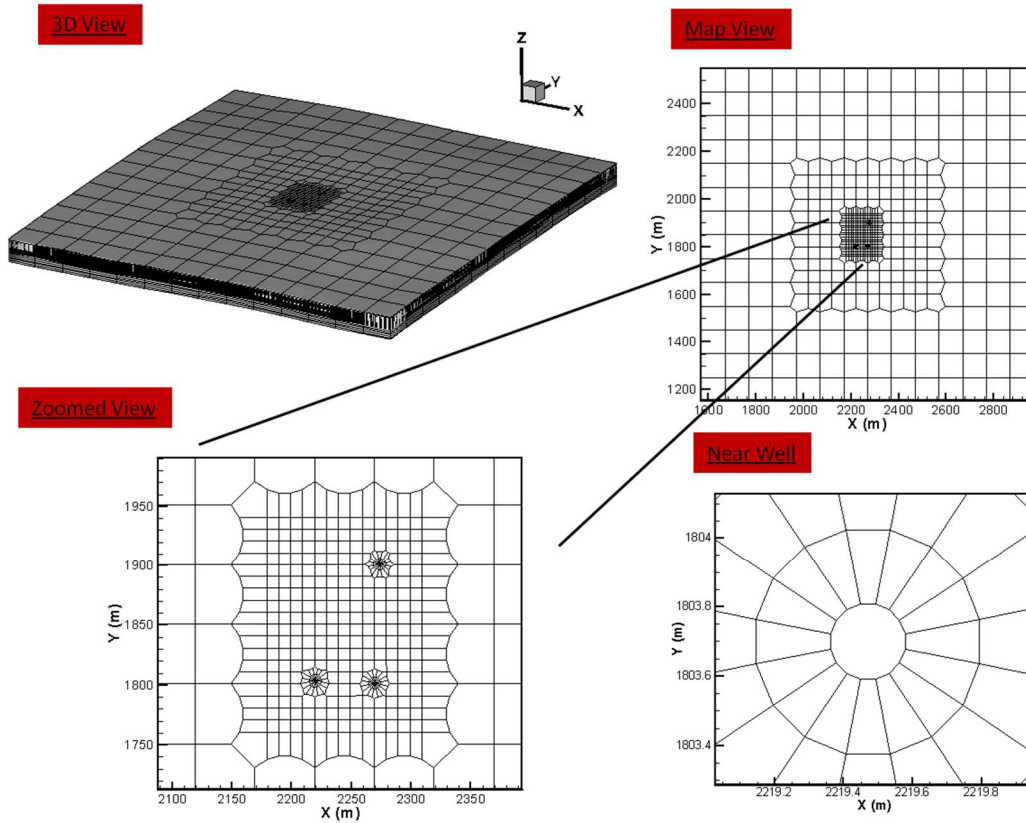
Figure 23: Mesh in 3-D view, map view and zoomed view in the near-well region.

The porosity of sandstone layers was assigned with a fixed value of 0.2 and those of mudstone and shale layers are assigned with a fixed value of 0.1. A fixed permeability value of 1×10^{-15} m^2 was applied to the mudstone layers and 1×10^{-16} m^2 to the shale layer. The well elements had a high permeability of 4.98×10^{-8} m^2. Change in pressure in the top element of each well was used for comparison with the corresponding measured changes.

A simulation was first run to obtain the equilibrated pressure profile with the in-situ density of formation brine, which served as the initial condition for the system. For the duration of the pumping tests, the changes in pressure are rather small at the far-field boundary of the model domain. Thus, a no-flow boundary condition was used in the model. Time-dependent pumping rates were formulated to represent the measured pumping rates Inversion of Pumping Tests Using iTOUGH2

The inverse modeling tool iTOUGH2 was used for automatic model calibration (Finsterle, 1999). The model domain was parameterized using multiple zones, with each zone assumed to have uniform rock properties. Three parameterization schemes were considered, reflecting three different conceptualizations of the system. As a global measure of misfit between measured values and calculated system response, the objective function was calculated using weighed least square of residuals by considering the measurement error (Finsterle, 1999). In the pumping tests, the pressure perturbation in the pumping well was an order of magnitude greater than in the observation well. The weight of each pressure dataset was then normalized to its maximum drawdown, so that each pressure dataset gets roughly the same weight. The Levenberg-Marquardt minimization algorithm was applied to find the minimum of the objective function through multiple iterations (Finsterle, 1999). A constant perturbation factor of 0.1 was specified for the numerical computation of the Jacobian matrix. Calculation of the elements of the Jacobian matrix for sensitivity analysis was conducted using a forward finite different quotient. Here only the inversion and results are presented for the first case, for details of other cases, refer to Chen et al. (2013).

This study honors the shale layer subdividing the sandstone unit into two layers. This concept was adopted from the observation of the core logs in both Ktzi 200 and Ktzi 201: a low-permeability layer (0.1–1 mD) of about 2-m thickness subdivides the sandstone unit into two layers at the depth of 643 m (Norden et al., 2010). The model has the upper and lower sandstone layers, a shale layer in between, and an underlying mudstone layer (Figure 5-7). Since the wells are not cemented in the reservoir section, the model has the Ktzi 200 and Ktzi 201 wells connected to both the upper and lower sandstone layers. Ktzi 202 has only a layer of permeable sandstone approximately 8-m thick, located at depths between 628 m and 636 m (upper sandstone layer). At the depths where it would have been expected the lower sandstone layer to be located, it is instead composed of low permeability mudstone, based on core data. Therefore, only horizontal connections were provided between Ktzi 202 and the surrounding reservoir in the upper sandstone layer.

The upper and lower sandstone layers were parameterized using multiple zones in each layer (Figure 23). The near-well 90 m × 180 m region was uniformly parameterized into nine zones in the upper sandstone layer, and seven in the lower sandstone layer. Surrounding this region are four zones in the eastern, western, southern, and northern directions, which may or may not serve as hydraulic boundaries depending on their assigned (or estimated) permeability values. The logarithm permeability values of the 24 zones were subject to calibration and have a uniform initial guess of -13.5. The permeability of the shale layer was fixed to 1×10^{-16} m^2, and that of the muddy layer was fixed to 1×10^{-15} m^2. While keeping other hydraulic parameters fixed (e.g., specific storativity and porosity), the logarithm permeability values were calibrated against the observed pressure changes in all the wells of all the pumping events.
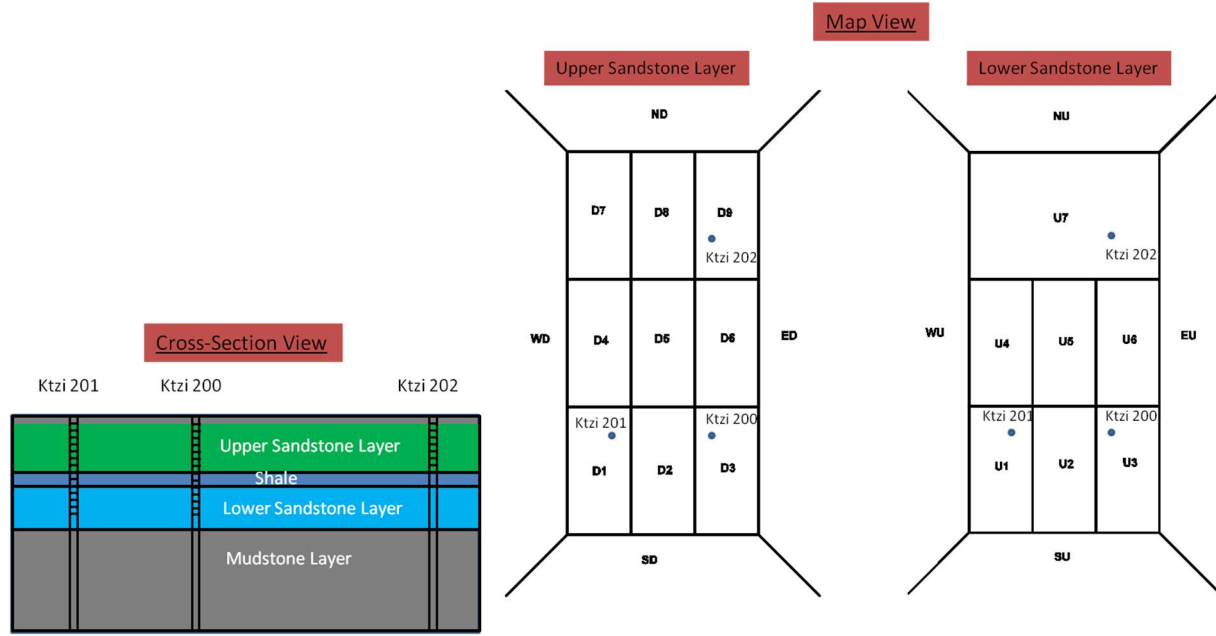
Figure 24: Parameterization for inversion.

4.2.3   Inversion Results and Discussion

The calibrated model produced calculated pressure drawdown in excellent agreement with the measured data (Figure 25). The objective function of the model was 0.123×10^5. The calculated system responses match the data well except for dataset P201O200, where measured pressure in Ktzi 200 was extremely small as pumping was conducted in Ktzi 201, and for the recovery period (after ~18.5 days) in dataset P200O200. Regarding dataset P201O200, the maximum drawdown in Ktzi 200 was approximately 1/10 of that in the other observation well (Ktzi 202), and the model overpredicts the pressure drawdown Ktzi200. The discrepancy might be caused by measurement error or local heterogeneity near the wellbore that was not captured in the model. Nonetheless, the overall excellent match between the calculated system response and measured data indicates that this model captures the essential elements to describe the flow between wells induced by the pumping tests in the Stuttgart formation.

The estimated spatial distributions of log$k$ in the upper and lower sandstone layers are shown in Figure 24. Zones of relatively higher permeability are observed between Ktzi 201 and Ktzi 202 and between Ktzi 200 and Ktzi 202, compared to a less permeable zone that is between Ktzi 200 and Ktzi 201. For example, in the upper sand layer, a permeable "channel" (U4, U7, and U8) with estimated permeability ranging between 100–1,000 mD connects Ktzi 201 and Ktzi 202. The zone U6 connecting Ktzi 200 and Ktzi 202 has an estimated permeability of 67 mD. However, a relatively low permeability zone is located between Ktzi 200 and Ktzi 201 and the estimated permeability values of U2 and U5 are 23 mD and 0.01 mD, respectively. In the lower sandstone layer, the zones D2 and D5 have estimated mean permeabilities of 0.001 mD and 0.015 mD, respectively.

Most boundary zones are estimated to have low permeabilities with only a few exceptions. In the upper sandstone layer, low permeabilities are observed in the northern (NU, 0.73 mD), western

(WU, 5.2 mD), and eastern boundary zones (EU, 5.2 mD). The southern boundary zone (SU), however, is a quite permeable (169 mD). The lower sandstone layer shows a different pattern of log$k$ distribution in the boundary zones. As the southern and northern boundary zones are less permeable, the permeabilities of the eastern and western boundary zones are in a range of 75–138 mD.
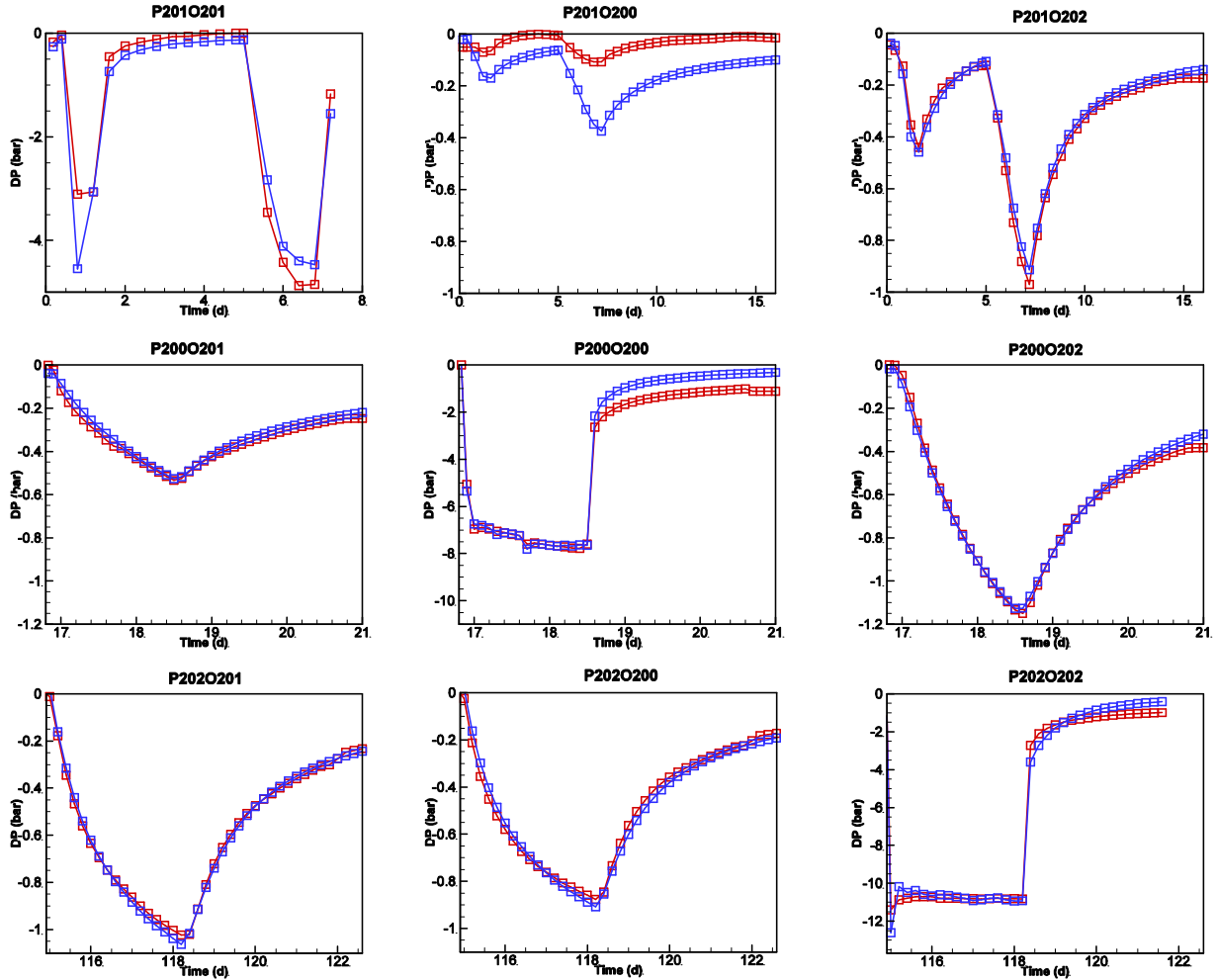
Figure 25: Calculated (blue squares) and measured (red squares) pressure drawdown.

Even though the estimated permeabilities in the zones where the wells are located (in the near-well region, as described above) actually represent spatially averaged (effective) values for the entire zone, these estimated values are compared to the measured core permeability data available at these wells. Similar to their corresponding core logs, the calibration results show that in Ktzi 201 and Ktzi 200 the upper sandstone layer is less permeable than the lower sandstone layer (log$k$ of U1 is less than for D1 and log$k$ for U3 is less than for D3). The zones U1 and D1 (where Ktzi201 is located) have calibrated permeabilities of 38 and 127 mD, respectively. Those of U3 and D3 (where Ktzi 200 is located) are 55 and 217 mD, respectively. The core logging in the Ktzi 202 borehole shows the presence of only one layer of high permeability sandstone, below which is the mudstone layer of low permeability. The calibration results are consistent with the measured core logging data, with the estimated permeability of the upper (U9) and

lower (D9) sandstone layers being 86 mD and 0.02 mD, respectively. While the estimates are generally lower than the geometric means of the measured core permeabilities, they are within an order of magnitude and show a consistent trend (Table 3). These are other results from literature will be further analyzed in the discussion section.
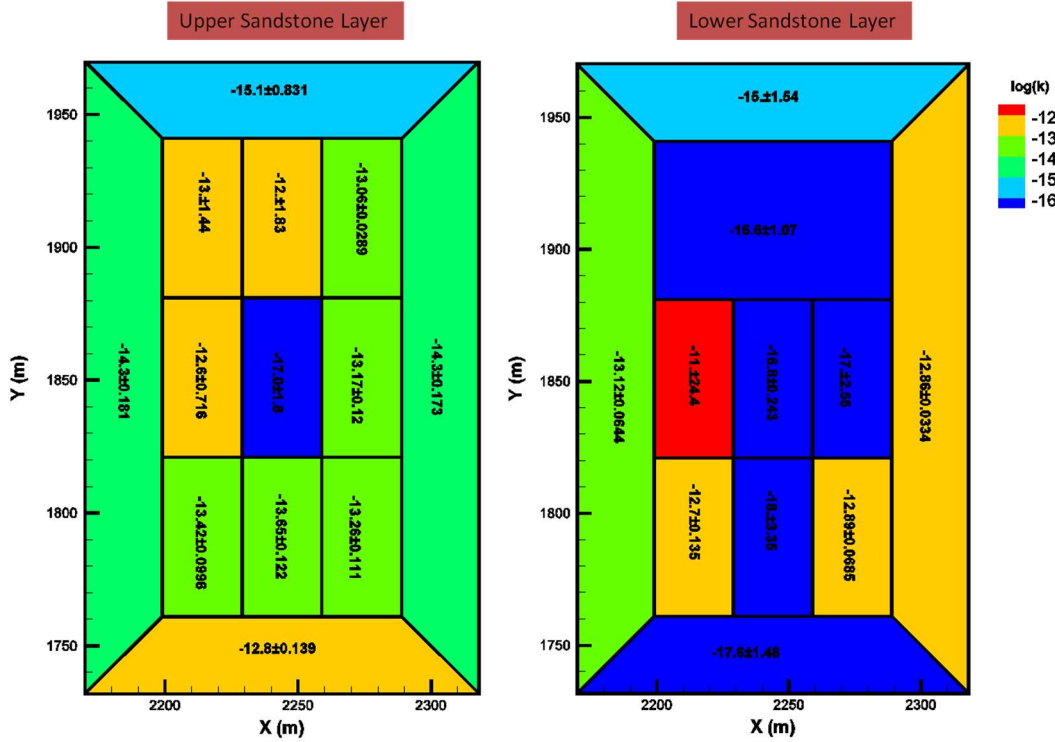
Figure 26: Estimated log(k) values and standard deviations (indicated after the +/-) for each zone in the upper and lower sandstone layers

The model produces calibrated values with relatively small standard deviations (i.e., low uncertainty). Due to increased sensitivity to the pressure data, the calibrated values close to the pumping wells in general have relatively smaller deviation, compared to those far away from the wells, with some exceptions for zones D2, D4, and D6. These zones may be less sensitive to the pressure data from the pumping tests because of their position relative to the pumping wells and having either very high or low permeability. For example, the estimate for D4 has a standard deviation of 24.4, which means this zone is not sensitive to the pressure data. The insensitivity of zone D4 may be related to the fact that flow in that zone is controlled by the surrounding low permeability zones. The relatively high uncertainty estimates for zones D2 and D6 may result from the log$k$ values for these zones being several orders of magnitude lower than for most other zones in the model, and the system response is not very sensitive to small changes in these low values; nonetheless, regions D2 and D6 can be categorized as low permeability.

The inversion results show that channels (adjacent zones of high permeability) are present between the Ktzi 202 and Ktzi 200/Ktzi 201 and a low-permeability barrier lies between the Ktzi 201 and Ktzi 200. The wells are located in a semi-closed system: the near-well region is bounded by low permeability zones in three sides with one or two sides (southern and/or western) open to

higher permeability regions. Modeling a semi-closed system is essential for reproducing the pressure responses of the pumping tests, and this required choosing a parameterization that allows for the characteristics of such a system to be estimated by inverse modeling.

4.2.4   Comparison of Inversion Results with Field CO$_2$ Injection Monitoring Data

4.2.4.1 Comparison with Values Reported in Literature, and Derived from Core Analysis

The estimated permeability is compared with the literature values and measured core permeability in Table 3. Wiese et al. (2010) analyzed the exact pumping tests data using analytical approaches. The calibrated permeability values near the well locations in this study are similar to their calibrated values from the build-up phase with applied boundary configurations (Wiese et al., 2010). Lengler et al. (2010) simulated the CO$_2$ injection test at this site and a good match in the bottomhole pressure of the injection well was obtained when a permeability of 90 mD was used. In this study, the permeability in Ktzi 201 to be 89 mD (in the case not shown) was estimated, which is very close to that reported by Lengler et al. (2010).

Table 3: Comparison of estimated permeability with the geometric and arithmetic mean permeability from core analysis (Norden et al., 2010), and the calibrated permeability in Wiese et al. (2010). Geometric and arithmetic means are calculated based on the permeability data determined from borehole logging using the Coates equation (Norden et al., 2010)

Core ID	Core Data (Norden et al., 2010)	Wiese et al. (2010)	This Study
Ktzi200	Overall (depth: 599.6–615.8m) geometric mean: 261 mD arithmetic mean: 560 mD harmonic mean: 4.25 mD Upper Layer (depth:599.6–608.3m) geometric mean: 312 mD arithmetic mean: 354 mD harmonic mean: 260 mD Lower Layer (depth: 609.9–615.8m) geometric mean: 706 mD arithmetic mean: 1,002 mD harmonic mean: 269 mD	Overall (thickness: 14.6 m) 63 mD	Overall Upper Layer (thickness: 8 m) 55 mD Lower Layer (thickness: 8 m) 217 mD
Ktzi201	Overall (depth:600.6–617.6m) geometric mean: 332 mD arithmetic mean: 755 mD harmonic mean: 33 mD Upper Layer (depth: 600.6–608.9m) geometric mean: 243 mD arithmetic mean: 506 mD harmonic mean: 74 mD Lower Layer (depth: 609.6–617.7m) geometric mean: 664 mD arithmetic mean: 1,062 mD harmonic mean: 184 mD	Overall (thickness:17.6 m) 90 mD	Overall Upper Layer (thickness: 8 m) 38 mD Lower Layer (thickness: 8 m) 127 mD
Ktzi202	Overall (depth: 593.7–610.7m) geometric mean: 15 mD arithmetic mean: 425 mD harmonic mean: 0.5 mD Upper Layer (depth: 593.7–602.3m) geometric mean: 525 mD arithmetic mean: 718 mD harmonic mean: 171 mD Lower Layer (depth: 602.3–610.7m) geometric mean: 0.39 mD arithmetic mean: 0.93 mD harmonic mean: 0.2 mD	Overall (thickness: 8 m) 109 mD	Overall Upper Layer (thickness: 8 m) 86 mD Lower Layer (thickness: 8 m) 0.02 mD

The permeability estimate for the top sandstone layer is lower than for the lower sandstone layer in Ktzi200 and Ktzi201, which is consistent with the core logging. In Ktzi202, the estimate for the lower layer has very low permeability and the top layer has a permeability of 86 mD, which is in a good agreement with the core logging. From the core logging of Ktzi202, there is only a layer of sandstone (high permeability) in this location; below the sandstone layer is mudstone of low permeability.
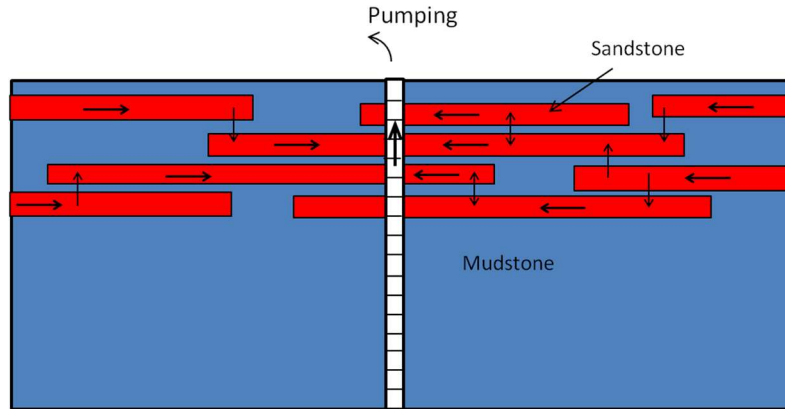
Figure 27: Conceptual view of the flow condition in the pumping tests in the Ketzin site.

The effective permeability (k_{eff}) is expected to be between arithmetic (k_A) and harmonic (k_H) means of the system (Matheron, 1967; Sanchez-Vila et al., 2006). When the fluid flow is parallel in a layered system, the k_{eff} tends to be close to the arithmetic mean of the layer permeabilities (Javandel and Witherspoon, 1969; Long et al., 1996). When the flow is perpendicular to the layers, the k_{eff} tends to close to the harmonic mean (Long et al., 1996). When k is a multi-lognormal stationary random function with isotropic correlation structure, Matheron et al. (1967) showed that k_{eff} is close to the geometric mean. The calibrated k_{eff} values in the near-well zones are between their harmonic and geometric means, indicating that the sandstone layers are not well connected horizontally and the fluid flow in vertical directions is significant. As described by Förster et al. (2010), the sandstone unit (channel facies) in the Stuttgart formation is composed of layers of individual sandstone bodies stacked together forming the elongated sandstone channel belt. Due to the finite volume of the individual sandstone layers near the wells, fluid flow through the vertical interfaces is necessary to reach the far-field regions (as shown in Figure 27).

4.2.4.2 Consistency of the Estimated Low-Permeability Barrier between Ktzi200 and Ktzi201 with CO₂ Injection Test Results

On the connectivity between the wells, previous wisdom was that Ktzi200 and Ktzi201 were well connected, belonging to the same channel, while Ktzi202 might not be well connected with Ktzi201/Ktzi200. Supporting this argument is that the Ktzi200 and Ktzi201 boreholes have similar lithological profiles, and that of Ktzi202 is different. The CO₂ injection test in Ktzi201 showed an early arrival of CO₂ in Ktzi200 (27 days), but a delayed arrival at Ktzi202 (271 days).

The pumping test results showed that when fluid was pumped from one of the Ktzi200/ Ktzi201 pair, the pressure response in the other well was extremely small. To the contrary, the responses to pumping between Ktzi202 and Ktzi201/Ktzi200 are fairly large. Wiese et al.(2010) initially

hypothesized that an impermeable region might be present between Ktzi200 and Ktzi201, based on analysis of the pressure drawdown data. However, they subsequently excluded this possibility after analyzing the pressure arrival time between the two wells (Ktzi200 and Ktzi201). They found the pressure derivative signal (dp/dt) travels the distance between Ktzi200 and Ktzi201 pretty fast (in about 12 minutes) and the travel time is proportional to the distance compared to those between Ktzi202 and Ktzi200/Ktzi201. They concluded that a large-scale no-flow boundary cannot exist between Ktzi200 and Ktzi201. However, the early-time portion of the pressure signal was dominated by the small heterogeneous feature such as fracture/thin layer of highly permeable sandstone. When pumping started, fluid flow was mostly through these highly permeable pathways. Over time, the pressure gradient between the high and low permeable layers decreased. The late-time drawdown was more determined by the effective permeability over a large influence volume (thus heterogeneity at a larger scale). Similar responses are observed in pumping tests in layered porous medium with contrasting permeability (Javandel and Witherspoon, 1969) and fractured rock (Moench, 1984). Therefore, it was likely that the presence of high-permeable thin layers embedded in these low-permeability barrier zones caused the fast arrival of pressure signal (dp/dt). A model was developed to prove this concept in Section 4.4.

Norden and Frykman (2013) simulated the facies distribution using geostatistical methods. Their work integrated regional geology, seismic data, core logging data, and other information, to provide a geological model describing the large-scale facies distribution. Based on 60 realizations they obtained, they argued that it was very likely that the channel bodies of the drilled boreholes are related to the same channel or to two channels which are connected. All of their 60 model realizations showed the sandstones in the Ktzi200 and Ktzi201 boreholes were located in the same channel belt system, and some of the realizations showed floodplain facies were present between the Ktzi202 and Ktzi200/Ktzi201 (Norden and Frykman, 2013).

Different from previous understanding, the current study concludes that a low-permeable zone was present between Ktzi200 and Ktzi201 while highly permeable channels connect Ktzi202 and Ktzi200/Ktzi201. First, the calculated pressure drawdown with this configuration matches the pressure data of the pumping tests well. Second, although similarity exists between lithological profiles of the Ktzi200 and Ktzi201 boreholes and they are likely to be in the same channel, the chances are good that the pores between them are filled by clay minerals and the individual sandstone bodies are not well connected (as shown in Figure 27). Core analysis showed cementation is quite common at the site and the sandstone pores are often filled by clayey and flake-looking minerals (Norden et al., 2010). Depending on the grade of cementation, the porosity and permeability of the sandstones can decrease by orders of magnitude (Norden et al., 2010).

Furthermore, a set of electrical resistivity (ERT) data provides new evidence regarding the presence of a low-permeability zone between Ktzi200 and Ktzi201. Cross-hole electrical resistivity surveys were conducted using the permanent vertical electrical resistivity array (VERA) to track the CO$_2$ migration in the Ketzin site (Kiessling et al., 2010; Martens et al., 2012). The displacement of the brine originally filling the pores with supercritical CO$_2$ results in an increased electrical resistivity in place. ERT provides a way to image the resistivity changes caused by CO$_2$ migration (Schmidt-Hattenberger et al., 2011). The ERT results of Mertens et al., 2012 (Figure 28) showed a significant resistivity increase at the reservoir level from the beginning of the CO$_2$ injection in June 2008. The high-resistivity region (high CO$_2$ saturation) in

the cross-hole section expanded over time and stabilized after 2 years of injections. The resistivity profile in June 2011 clearly shows that a vertical low-resistivity zone exists near the Ktzi200 side, indicating the zone has low permeability and blocked the supercritical CO_2 from entering the pores of this zone.
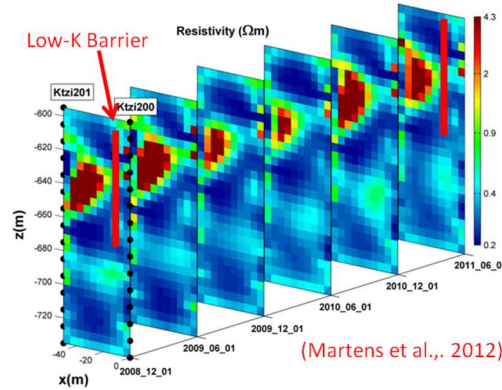
Figure 28: Electrical resistivity as a function of time from ERT monitoring data (Martens et al., 2012)

If there is a low-permeability barrier between Ktzi200 and Ktzi201 and high-permeability channels between Ktzi202 and Ktzi201/Ktzi200, an obvious question is why CO_2 arrived at Ktzi200 much earlier than Ktzi202. In Section 4.4, an explanation for this seemingly contradictory phenomenon was proposed.

4.2.4.3 Possible Presence of Low Permeability Boundaries Outside of the Near-Well Region

The inversion results indicate that the wells are situated in a semi-closed system. The near-well region is bounded by low-k regions except for 1 or 2 sides with high-k regions. As shown in the comparison between the Cases 1 and 2, incorporating this semi-closed boundary structure in the model is essential for reproducing the pressure responses in the pumping tests. Evidence supporting the validity of this conclusion is that, after pumping, most wells fail to recover to their original level over a long period of time (days to weeks). As mentioned by Beutler et al. (1999), the Stuttgart formation reflects a depositional style change from playa to fluvial environment, so the presence of one-ended fluvial channels is plausible from the geology standpoint.
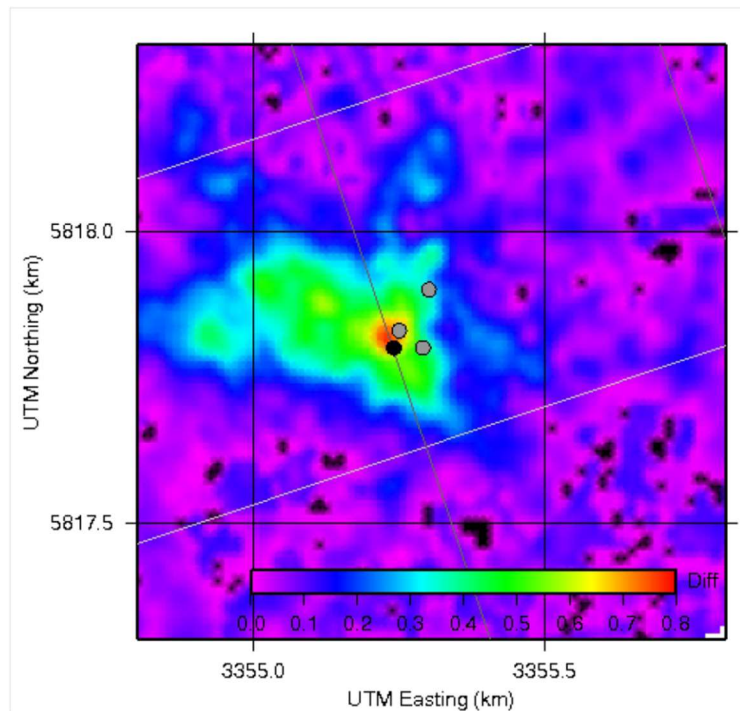
Figure 29: CO₂ plume inferred from 3-D seismic data in Martens et al. (2012).

The inversion results of this study showed a consistent low-permeability zone in the northern boundary region. The core loggings show the thickness of the sandstone unit of Ktzi 202 borehole is almost half that of Ktzi 200/Ktzi 201 (Norden et al., 2010). Norden and Frykman (2013) reported that the sandstone unit was not observed in the top of the Stuttgart formation in a borehole (Ug Ktzi 163/69, in Norden and Frykman (2013)) located in the northeastern region and approximately 4,000 m away from the site. It is possible that the closed end is present due to the sandstone unit thinning out in the northern region near the Ktzi 202.

Three-dimensional (3-D) seismic surveys, shown in Figure 29, suggest that the CO₂ plume extends laterally to the western direction after 15 months of injection (Martens et al., 2012). The plume showed a significant amount of CO₂ between Ktzi 201 and Ktzi 202, while a relatively small amount of CO₂ was detected behind Ktz i202 (Martens et al., 2012). A possible explanation is as follows: a high-permeability sandstone channel provides good connection between Ktzi 201 and Ktzi 202. When CO₂ was injected in Ktzi 201, the pressurized CO₂ pushed the brine between Ktzi 201 and Ktzi 202 to the northern boundary zones. Due to the low permeability of the northern boundary zones (and other parts of the semi-closed structure) the brine displacement is limited at a low rate, resulting in the accumulation of brine in this region and the delay of CO₂ arrival to this region. Although CO₂ transport is a complex phenomenon controlled by many factors besides permeability, this semi-closed structure estimated through inverse modeling of the pumping test data seems to provide a plausible explanation of the CO₂ plume inferred from 3-D seismic surveys.

4.3   DETECTION APPLICATION TO HYPOTHETICAL LEAKAGE PROBLEMS

4.3.1   <u>CO₂ Pilot Test at Ketzin</u>

CO_2 injection at Ktzi 201 was conducted from June 26, 2008 to August 29, 2013. The injection rate varies significantly during the 5-year operation, from 0 to a maximum rate of 58 kg/min (see Figure 30). The total injected mass is 67,271 tonnes CO_2 and the average rate is 26.6 kg/min. Pressure has been monitored at a sensor located at a depth of 550 m in the injection well, and at the well head of the injection well and two monitoring wells. The bottomhole pressure at Ktzi 201 shows significant variations with time, which are caused by changes in injection rate (Figure 30).
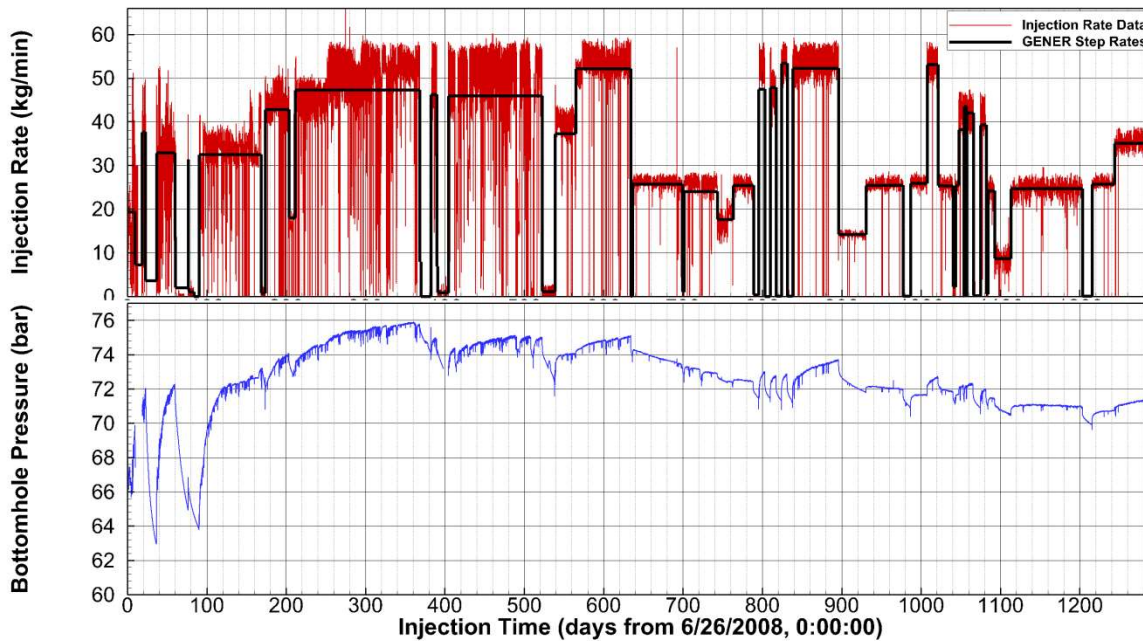
Figure 30: Actual CO₂ injection rate (in red) and bottomhole pressure (in blue) at a depth of 550 m at the injection well, with measurement frequency of every 5 min, as well as the step rates of injection used for modeling.

To test the effectiveness and efficiency of above-zone pressure monitoring in detecting leakage through wells and faults, GFZ drilled an above-zone monitoring well (P300) into the shallow Exter formation to a depth of 440 m in August 2011. This formation is 42-m thick, consists of three high-permeability sandstone layers, with a total thickness of 12 m, and is 175 m above the Stuttgart formation. As shown in Figure 31, P300 is located at (7,249.9 m, 6,923.07 m), is relatively close to Ktzi 200 at (7,269.5 m, 6,801.6 m), Ktzi 201 at (7,219.5 m, 6,803.7 m), and Ktzi 202 at (7,273.6 m, 6,901.4 m), but is ~ 4 km away from the only appraisal well (Ktzi 163/69) (see Figure 18). Pressure monitoring at P300 started in August 2011; it appears that the monitored pressure does not experience any anomalies (i.e., there is no indication of pressure increases induced by leakage from the underlying, pressurized storage formation).
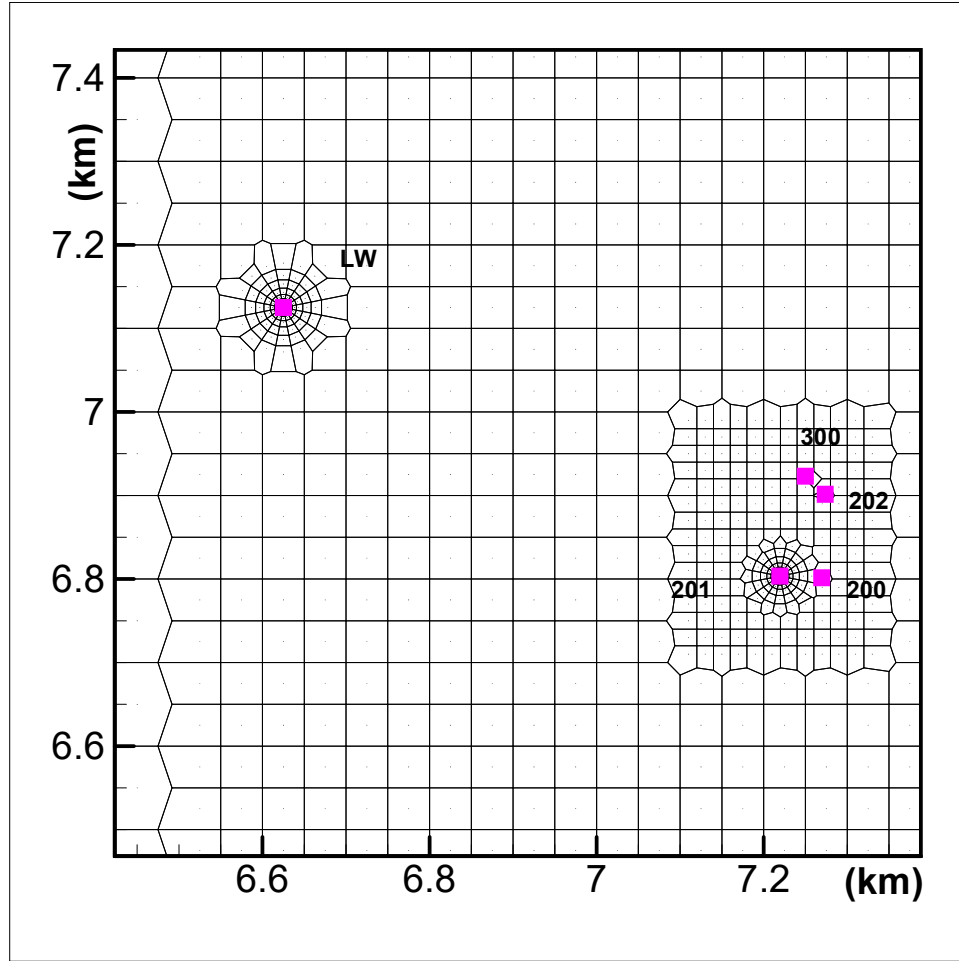
Figure 31: Locations of the injection well (Ktzi 201), two monitoring wells (Ktzi 200 and 202) in the storage formation, one monitoring well (P300) in the above zone, and the leaky well (LW) connecting the storage formation to the above zone.

4.3.2   Leakage Problem Formulation

In order to apply the developed methodology for early leakage detection to the Keztin site, this study hypothetically introduced a leaky well at (6,625.0 m, 7,125.0 m) (see Figure 31). The leaky well is located 675 m away from the injection well, and lies within the monitored CO_2 plume. The leaky well connects the storage formation with the shallow Exter aquifer. The radius of the leaky well is 0.11 m, and the well permeability considered varies from 10^{-7} to 10^{-11} m². In this way, a hypothetical leakage problem was formulated. It was assumed in this example that the presence of a potentially leaking well was known, but its properties were not.

To apply the detection methodology to the hypothetical leakage problem, this study: (1) developed the forward model by including the storage formation, the caprock, and the above-zone aquifer, and by using the revised geologic model of the storage formation; (2) conducted the forward simulation of the CO_2 injection and CO_2/brine leakage through the leakage well; (3) used the simulated pressure at the three wells (Ktzi 200, 201, and 202) in the storage formation, and the simulated pressure at P300 in the shallow aquifer as the "true" monitoring data; (4)

employed the leakage detection methodology to estimate the leaky well permeability, and compared the estimated value with the "true" value used for generating the monitoring data; (5) simulated the CO$_2$ injection into the system with the leaky well and its estimated permeability, and compared the CO$_2$ arrival time at the leaky well with the earliest time when the leakage is detected with confidence; and (6) demonstrated the benefits of the early leakage detection methodology.

The detectability of leakage through the leaky well by using monitoring data at the four wells depends on (1) the injection rate, (2) the leakage rate (i.e., the leaky well permeability), and (3) noises in the pressure data. In order not to significantly deviate from the actual injection history and injection rate at the pilot-scale test site, the total injected CO$_2$ mass in the hypothetical example was constrained to less than 100,000 metric tonnes (a value on which LBNL and our project partner GFZ agreed) in the base case, but the length of injection period was varied. Table 4 shows the different combinations of leaky well permeability, injection rate, and degree of pressure data noise for the leakage problem. Note that the injection period was fixed at 2 years. For each combination of detection application, the forward simulation was reran and the "monitoring" data generated, the detection conducted, and the benefits of the early detection results evaluated. For each application, all parameters in the forward models during the inversion are kept unchanged from their values used in the forward simulation to generate "monitoring data".

Table 4: Different combinations for the leakage problem with varying leaky well permeability, injection rate, and whether or not with pressure data noises

Leaky Well Permeability (m^2)	Injection Rate	Pressure Data Noises (standard deviation)
10^{-7}, 10^{-8}, 10^{-9}, 10^{-10}, or 10^{-11}	1.59 kg/s or 15.9 kg/s	0.1 or 0 bar

4.3.2.1 Forward Modeling

The forward model for simulating the two-phase CO$_2$-brine flow includes the Stuttgart formation, the Weser and Amstadt formations (caprock), and the Exter formation (the above-zone aquifer). To have negligible boundary effects, the revised geologic model was extended in 5 km × 5 km to a region of 15 km × 15 km, by extending 5 km to each direction (see Figures 32 and 33). The extended area is beyond the CO$_2$ plume, and a constant elevation is used from the edge of the geologic model (see Figure 31) because only the formation thickness is relevant to the single-phase brine flow. Within the geologic model domain, all thickness and elevation of all layers are kept unchanged from the geologic model for the Stuttgart formation. A constant thickness of 175 m and 12 m are used for the combined Weser/Amstadt caprock and the Exter formation (see Table 4).

4.3.2.2 3-D Model Development

First a two-dimensional (2-D) mesh is generated that has varying mesh resolution in the 15 km × 15 km domain, from cells sizes of 1 km × 1 km near the boundaries to very local refinement near the injection well and the leaky well. Figure 32 shows the generated 2-D mesh (i.e., the map

view of the generated 3-D mesh). In the vertical direction, the 3-D mesh has a total of 24 mode layers, with 3, 3, 16, 1, and 1 layer(s) for the lower, middle, and upper Stuttgart formation, the combined Weser/Amstadt unit and the Exter formation. The lower and middle Stuttgart units have low permeability and porosity, while the upper Stuttgart unit has high porosity and permeability, based on the revised 3-D geologic model.

Table 5: Geometric and hydrogeologic parameters for the storage formation system

Parameters	Lower Stuttgart	Middle Stuttgart	Upper Stuttgart	Weser/Amstadt	Exter
Thickness (m)	36	12	24	175	12
Model Layers	3	3	16	1	1
Porosity	Geomodel	Geomodel	Geomodel	0.14	0.33
Permeability	Geomodel	Geomodel	Geomodel	0.000029 mD	1,800 mD
Sr_w	0.5	0.5	0.5	0.5	0.5
Sr_{CO2}	0.25	0.25	0.25	0.25	0.25
Relative perm. m_{VG}	0.95	0.95	0.95	0.95	0.95
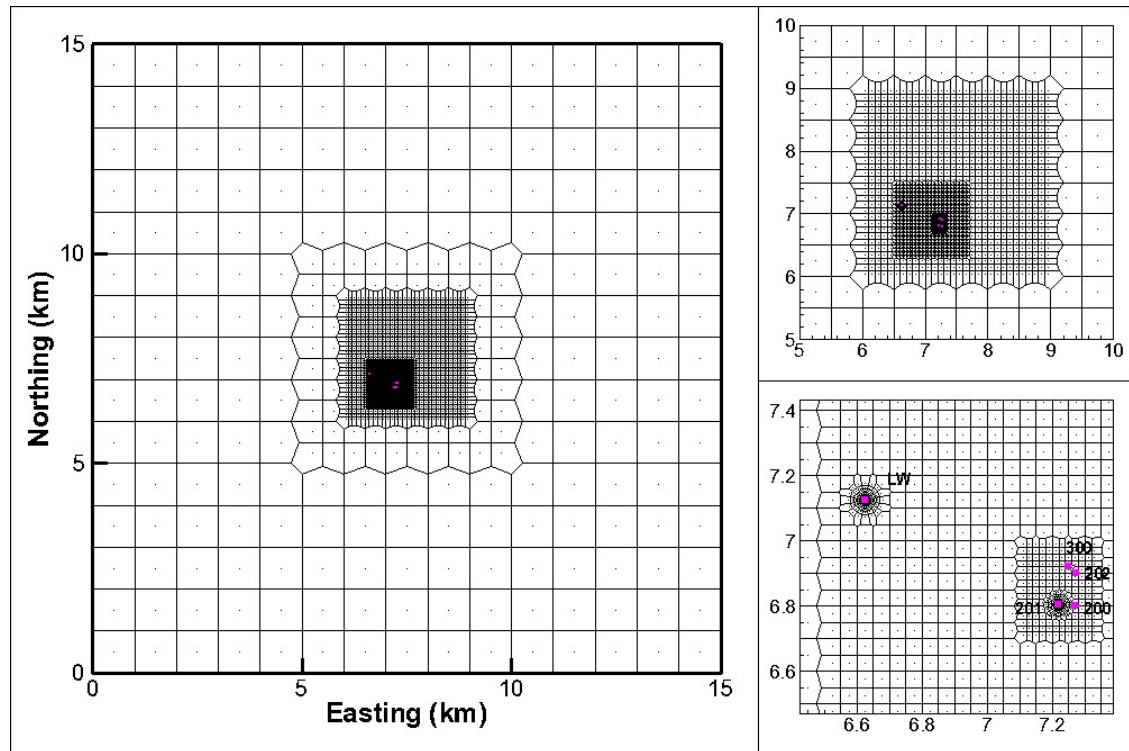
Figure 32: Map review of the generated 3-D mesh with local mesh refinements around the injection well and the leaky well, as well as in the estimated area of CO₂ plume.
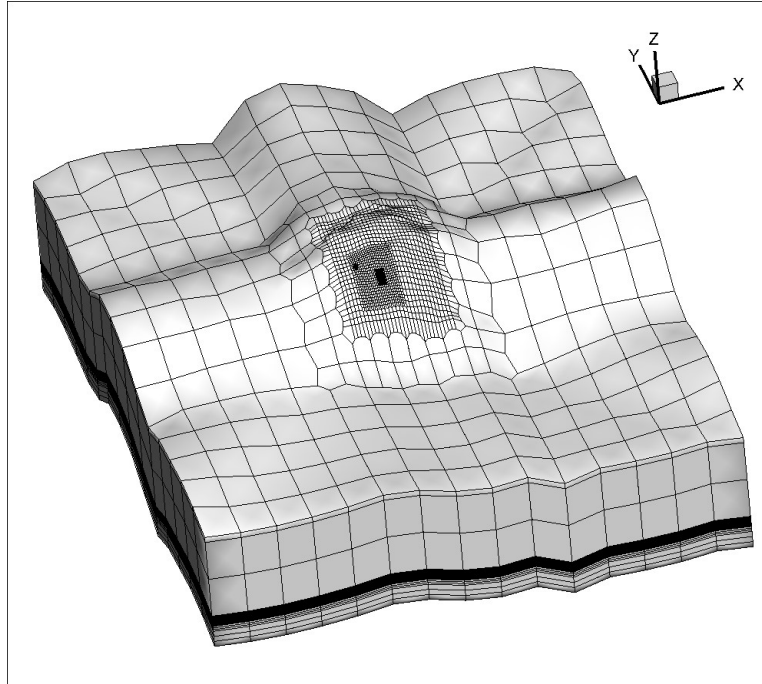
Figure 33: Generated 3-D mesh with coarse mesh far away from the injection and monitoring region and local mesh refinement around the injection well and the leaky well.

The complexity of the Ketzin site stems mainly from significant heterogeneity in porosity, permeability, and other rock properties. Figure 34 shows the spatial variability of permeability in Layers 4 through 8 in the upper Stuttgart unit in the developed 3-D flow model. (Note that Layer 3 in the upper Stuttgart formation has a low porosity and permeability.) In comparison with each of these five layers, Layer 6 may be of more interest as it connects the injection well and the leaky well through a high-permeability channel. For Layer 4, the permeability is very high near the leaky well, but much smaller near the injection well; as long as CO_2 leaks through the leaky well, it may also migrate into the high-permeability zone of Layer 4 after CO_2 enters the leaky well through a deeper layer.
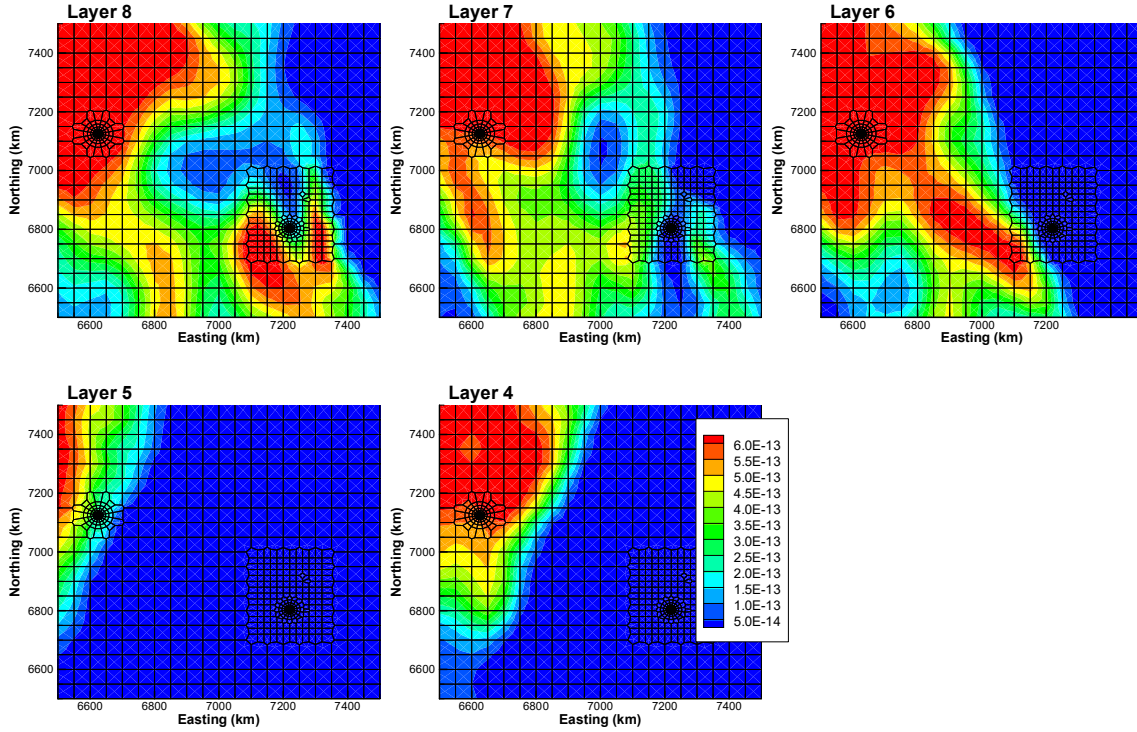
Figure 34: Model-layer permeability field, showing significant spatial variability. Layer numbers increase from top to bottom.

4.3.2.3 Forward Modeling for Obtaining "Monitoring" Data of Pressure

For each application, TOUGH2-MP/ECO2N was used to simulate the responses of CO$_2$ saturation, and pressure perturbations to CO$_2$ injection at Ktzi 201 and brine/CO$_2$ leakage at the leaky well. The pressure profiles (with time) at Ktzi 200, 201, and 202 in the storage formation, and at P300 at the above-zone aquifer were extracted and considered as pressure monitoring data to be used for the inversion in the next section. Figure 35 shows these pressure profiles for different leaky well permeability in the cases of constant injection rate of 1.59 kg/s for 2 years. The evolution of the pressure at each monitoring well was almost the same when the leaky well permeability was smaller than 10^{-9} m^2, providing insensitive leakage signals. This indicates that it might not be feasible to accurately estimate the leaky well permeability when the effective permeability is too small.
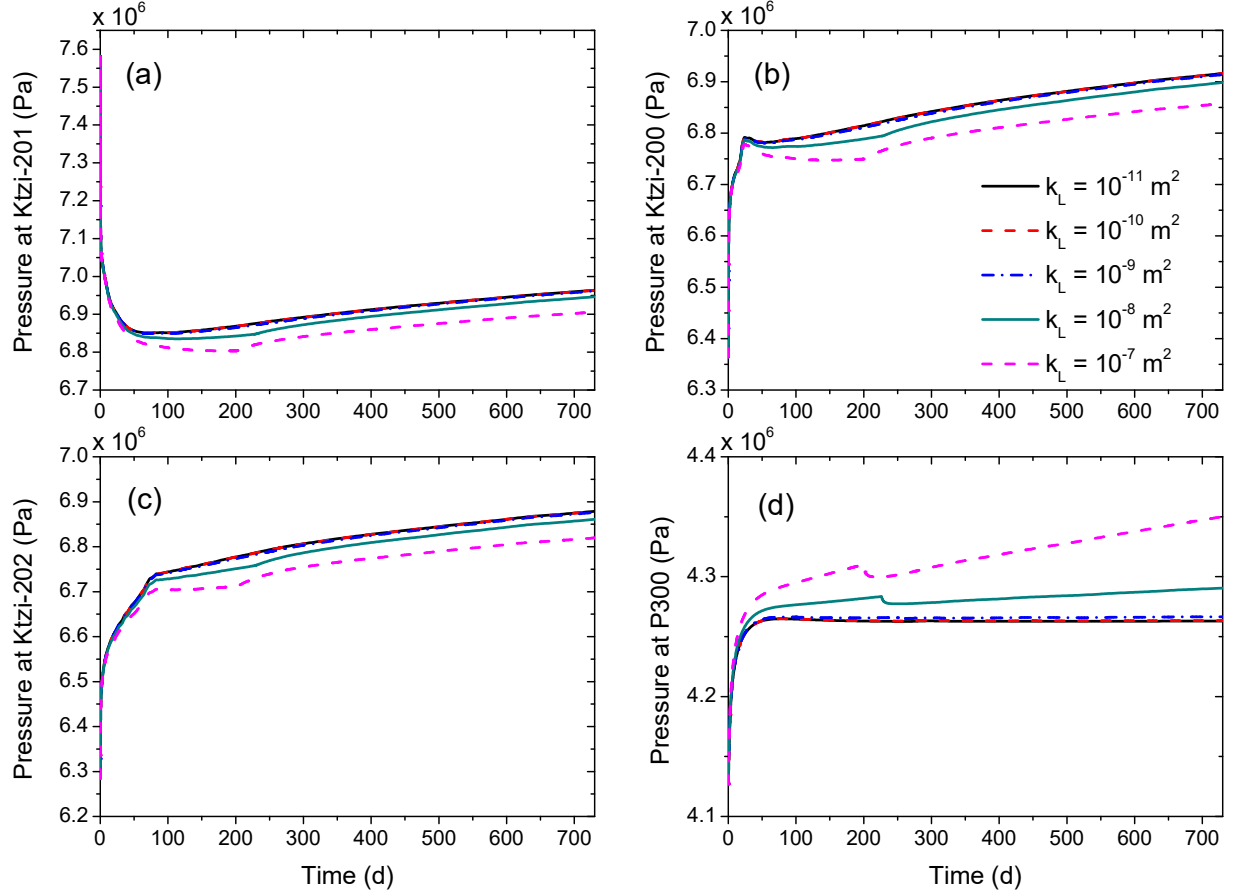
Figure 35: Monitoring data of pressure (a) at Ktzi 201, (b) Ktzi 200, and (c) Ktzi 202 in the storage formation, and (d) at P300 in the above-zone aquifer generated for the different cases of leaky well permeability values using forward modeling.

4.3.3   Inversion for Leakage Detection

In all applications, the only parameter to be estimated was the leaky well permeability, while the location of the leaky well was fixed. This represents an example of leakage detection for known abandoned wells, whose locations can often be determined by drilling record search during the site characterization phase. As mentioned before, only one monitoring well was used for the inversion in the above-zone aquifer and four wells in the injection zone.

4.3.4   Results of Leakage Detection and Discussion

4.3.4.1 Examples with 1.59 kg/s Injection Rate and 180-day Monitoring Data

This application includes the examples with five different leaky well permeabilities, an injection rate of 1.59 kg/s over 2 years, and no data noise. For each example, the detection via inversion was conducted using the first 180-day monitoring data. Figure 36 shows the match between the estimated leaky well permeabilities and their true values. The standard deviations of the estimated permeabilities are small (not shown), and the largest one is only 0.02. The estimated permeability was accurate for the examples with the leaky well permeability equal or higher than 10^{-9} m². For a lower leaky well permeability, the estimated permeability deviates from its "true"

value. This is because the pressure data are not sensitive to the leaky well permeability as shown in Figure 35. Note that the initial guess for the inversion of each example is 10^{-8} m^2.
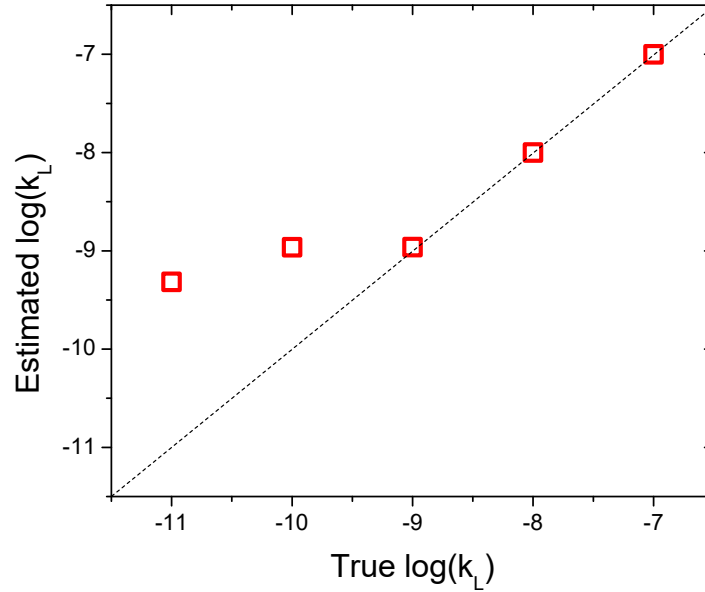

Figure 36: Comparison between the true and estimated leaky well permeability for the five different leaky well permeabilities, with an injection rate of 1.59 kg/s and no pressure data noises

Figure 37 shows the CO_2 plume in the overlying aquifer (Layer 1) and all the model layers of the upper Stuttgart unit (Layers 4 to 18) at 300 days of injection for a leaky well permeability of 10^{-9} m^2. The overall 3-D plume showed a strong effect of CO_2 buoyancy in the heterogeneous storage formation. In deeper layers (Layers 11–18), CO_2 occurred only near the injection well. The injected CO_2 mainly occupies the high-permeability zones in the top seven model layers (Layers 4–10, with 10 m thickness). At ~255 days, CO_2 arrived at the leaky well preferentially through Layer 6, and migrated upward to Layer 4, and farther up to the shallow aquifer (Layer 1). It is the sand channel of high permeability between the injection and the leaky well in Layer 6 that leads to an early arrival of CO_2 plume to the leaky well at this heterogeneous site, which was much earlier than in a homogeneous storage formation. It is very important to have a site-specific model that can accurately account for CO_2 plume migration to be able to estimate and predict leakage.

In the case of leaky well permeability of 10^{-9} m^2, the time of detection was 180 days, while the CO_2 arrival time at the leaky well was 255 days, indicating that there was a time lag between the detection time and the occurrence time of the actual risk of CO_2 leakage. This time lag can help to design and employ leakage mitigation measures. Figure 38 shows the evolution of gas saturation at the leaky well in the above-zone aquifer. The arrival of CO_2 in the above-zone aquifer was as early as 200 days after the CO_2 injection starts in the case of $k_L = 10^{-7}$ m^2. It seems in this case that the time lag was too small and the benefit of early leakage detection was not significant because the sand channel between the two wells in Layer 6 significantly shortens the CO_2 arrival time. However, CO_2 arrival time to a leaky well depends on many factors, including

the preferential flow channel connecting the injection well and the leaky well. As the leaky well permeability becomes smaller, it takes a longer time for CO_2 to migrate up the leaky well.
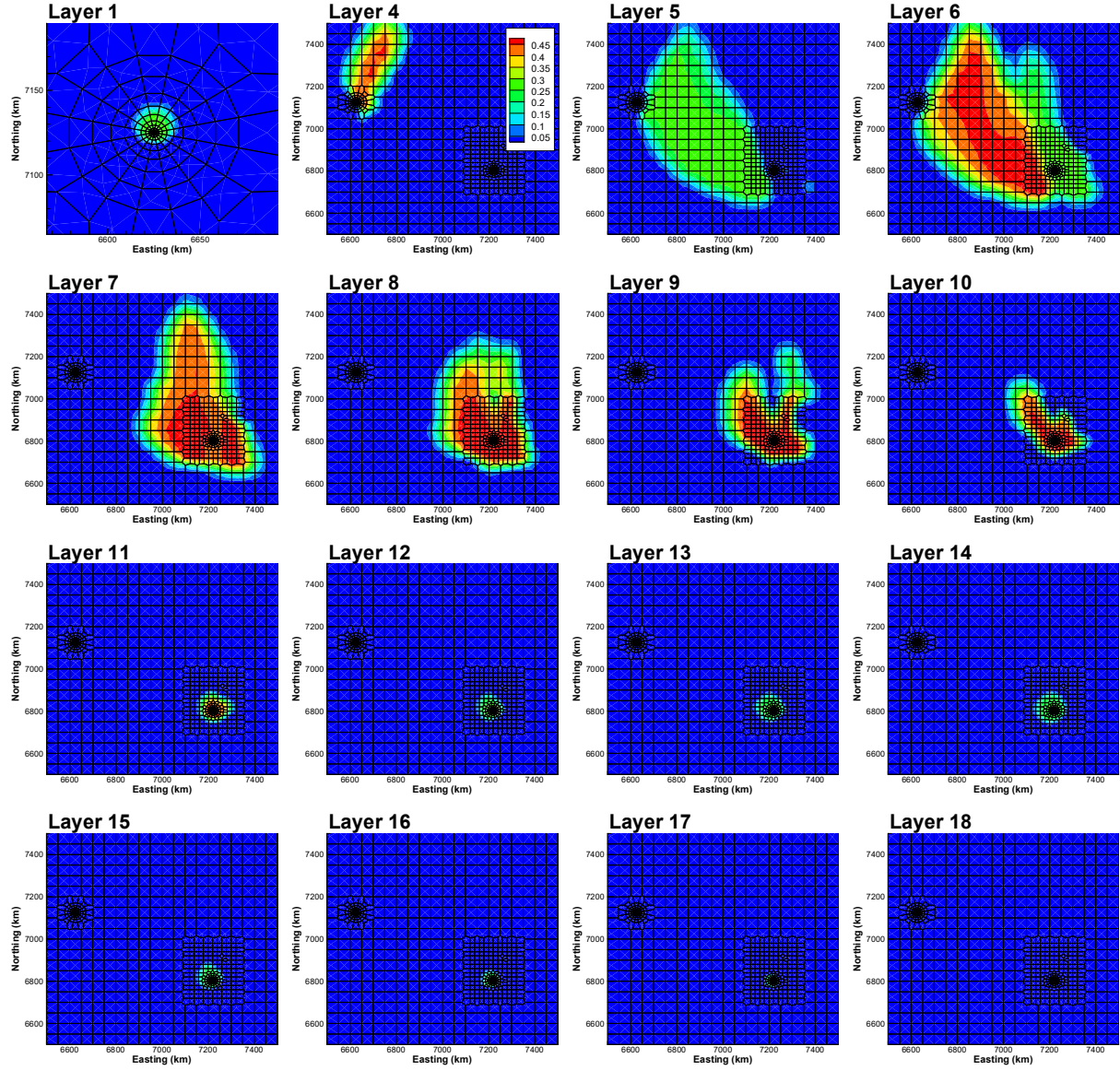

Figure 37: CO₂ plume distribution in all layers of the upper Stuttgart formation at 300 days of injection in the case of $k_L = 10^{-9}$ m². The map is zoomed in for Layer 1 to show the CO₂ leakage in the overlying aquifer. Layers numbers increase from top to bottom.
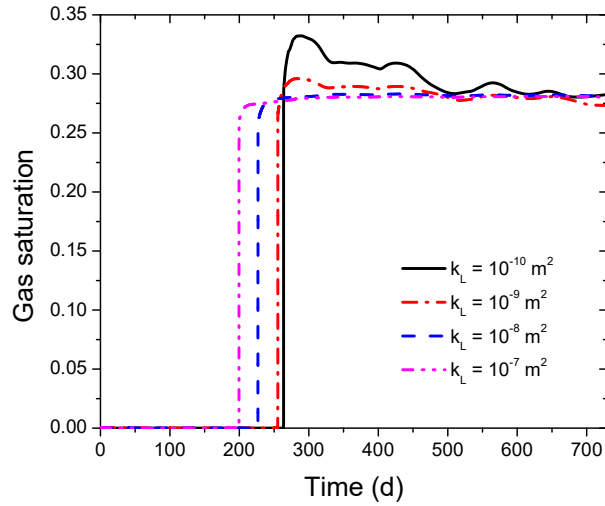
Figure 38: Evolution of gas saturation at the leaky well in the above-zone aquifer for four different leaky well permeabilities, with an injection rate of 1.59 kg/s and no pressure data noises.

4.3.4.2 Examples with 15.9 kg/s Injection Rate and 2-year Monitoring Data

This application included the same five leaky well permeabilities ranging from 10^{-7} to 10^{-11} m², but the injection rate was increased by a factor of 10 compared to Section 4.3.4.1. As shown in Table 6, the estimated leaky well permeability was very close to its true value, with a very small standard deviation, for a wide range of well permeabilities. When the injection rate was 1.59 kg/s, even with a 2-year period of monitoring, the accuracy of the estimate did not improve for cases with leaky well permeability lower than 10^{-9} m². This enhanced detectability with higher injection rate was mainly attributed to distinct pressure evolution at the monitoring wells. This indicated that with increase in the injection rate, the inversion-based detection methodology can detect the leaky well with higher accuracy.

Table 6: The estimated leaky well permeability and its standard deviation (using all data from monitoring and injection wells) in comparison to the "true" value and initial guess for the inversion process

Case Number	True value	Initial guess	Estimate	STD
BC1	-10.0	-8.0	-10.000	0.1884E-03
BC2	-11.0	-8.0	-11.001	0.1737E-03
BC3	-9.0	-8.0	-8.995	0.5218E-03
BC4	-8.0	-9.0	-7.999	0.2134E-03
BC5	-7.0	-9.0	-7.000	0.1053E-03

4.3.4.3 Examples with 1.59 kg/s Injection Rate and Up to 2-year Monitoring with Data Noise

This application introduced random data noise using a zero mean and a standard deviation of 0.1 bar to the monitoring pressure. For the leaky well permeability of 10^{-8} m^2 with 1.59 kg/s injection rate, four different monitoring periods were tested: 0.5, 1, 1.5, and 2 year. The results indicated that the detection can produce almost the same leaky well permeability estimates as those without data noises. The largest deviation for the estimated leaky well permeability was only ±0.06 (in logarithm), reassuring the effectiveness of the methodology. The size of the deviation was not necessarily correlated to the monitoring period, but dependent on the distribution of random noise, which indicated that the leakage signals at the monitoring wells were sufficiently strong as early as 0.5 year at this leaky well permeability.

4.4 CONCLUSISONS

The methodology of early leakage detection via inversion of pressure signals was applied to a hypothetical leakage problem at the Ketzin CO$_2$ pilot site in Germany. This problem was formulated by introducing a leaky well located 675 m away from the injection well, with varying well permeability and thus leakage rate. It was assumed that the location of the well was known (e.g., from historical well records), but not its properties. Note that at Ketzin, no signals of leakage of brine and CO$_2$ through the Weser/Amstadt formation (caprock) from the Stuttgart formation to the Exter formation (the above zone) were observed during the CO$_2$ injection over 5 years. The monitoring system consists of one injection well (Ktzi 201) and two monitoring wells (Ktzi 200, 202) in the storage formation, and one monitoring well (P300) in the Exter formation. The application demonstration includes the three components of the framework of the leakage detection system: site characterization, model calibration, and leakage detection.

The site characterization at Ketzin, mainly conducted by Geoforschungszentrum Potsdam (GFZ), included the drilling, geophysical logging, and coring and measurements, baseline 3-D seismic surveys, pumping tests prior to CO$_2$ injection, and development of a 3-D geologic model. All the site characterization data show that the Stuttgart formation is very heterogeneous, in particular in the upper 18 m of high-permeability sandstone.

A model calibration was first conducted to understand the heterogeneous distribution of permeability in the Stuttgart formation using pumping test data. These pumping tests conducted prior to the CO$_2$ injection test included nine pressure-time datasets in total, and one dataset from a well in the storage formation when pumping was conducted in each well. A forward model was developed using TOUGH2/EOS9, and the inverse modeling was conducted using iTOUGH2-PEST. The model calibration demonstrates that the pumping test datasets contain sufficient information of large-scale spatial-varying permeability. Specifically, the storage formation in the near-well region contained sand channels connecting Ktzi202 and Ktzi 201/200, and a low-permeability zone between Ktzi 201 and 200, and the near-well region was located in a semi-closed system with a flow barrier located in the north. These large-scale geologic features revealed from the pumping test calibration are consistent with the field monitoring of CO$_2$ injection. For example, the low-permeability zone between Ktzi 201 and 200 was consistent with the low-resistivity zone shown from the cross-well ERT data, while the nature of a semi-closed system was consistent with the four-dimensional (4-D) seismic data showing westerly CO$_2$ plume migration.

The early leakage detection method was then applied to the hypothetical leakage problem using the updated geologic model. The "monitoring" pressure at the three wells in the storage formation and at the one well in the above zone was obtained by simulating the CO_2 injection into the Stuttgart formation with the introduced leaky well. The forward model was developed for an extended 3-D domain of 15 km by 15 km covering the Stutgart formation, the Weser/Amstadt formation, and the Exter formation of ~260 m thickness in total. All the geometric and hydrogeologic parameters were based on site-specific data. Assuming a moderate CO_2 injection rate of 1.59 kg/s for 2 years, the detection methodology can accurately estimate the leaky well permeability when the permeability was higher than 1,000 darcy, indicating that the methodology was applicable to large leakage events with high flow rates. When the leaky well permeability was less than 1,000 darcy, the pressure signals were not sensitive to permeability, and the detection fails. However, with an increase in injection rate by a factor of 10, a leakage event via a well of 10 darcy or higher can be accurately detected.

The benefit of early leakage detection can be seen from the difference between the detection time using pressure signals and the CO_2 arrival time at the leaky well. The detection time was 180 days, while the CO_2 arrival time is 255 days. This time was relatively short due to the presence of a high-permeability preferential flow path connecting the CO_2 injection location and the leaky well.

5. **SUMMARY AND CONCLUSIONS**

This report summarizes the development, demonstration, and application of an inversion-based methodology for early leakage detection using pressure and surface-deformation monitoring data. The early leakage detection technique was complementary to current techniques for CO$_2$ leakage detection which are based on the physical, geophysical, or/and geochemical signatures that are induced by migrating CO$_2$ and that can be observed in the deep and shallow subsurface, at the land surface, and in the atmosphere. Many of these techniques have relatively low spatial resolution and coverage, in comparison to the footprint of CO$_2$ plumes, and all these techniques can only detect anomalous CO$_2$ signals long after CO$_2$ leakage has first occurred. The new technique proposed in this project has the ability to provide an early indication of potential CO$_2$ leakage before it occurs.

The framework of early leakage detection consists of four key components: site characterization for known surface faults and abandoned wells, early detection of brine leakage signals via joint inversion, CO$_2$ leakage prediction and monitoring, and decision-making for risk management and mitigation. The methodology for early detection of brine leakage signals was based on the fact that pressure and surface-deformation anomalies caused by brine leakage propagate in the subsurface much faster than CO$_2$ migrates. Thus, if successful, brine leakage could be an early indicator for potential CO$_2$ leakage, ideally long before the CO$_2$ plume would reach the leakage location. The early detection methodology involved automatic inversion of anomalous brine leakage signals to estimate the location and permeability of leaky features in the caprock. With regards to pressure measurements, these signals should be obtained not only in the injection formation, but also in the first aquifer overlying the caprock. A global sensitivity analysis was conducted to better understand under which conditions pressure anomalies in the overlying formations and the storage formation can be clearly identified as leakage signals, and evaluate signal detectability for a broad parameter range considering different detection limits and levels of data noise. The detectability in terms of detection time and detection region for a given leakage scenario (e.g., number, location, and permeability of leaky wells) can help understand the applicability of the early leakage detection methodology.

The inversion methodology for early leakage detection was used to estimate leakage parameters (i.e., the location and permeability of the leaky well) in four synthetic examples of idealized two-aquifer-and-one aquitard storage systems, with an injection well and a leaky well, for different monitoring scenarios. In Example 1, the formation parameters and pressure data were not associated with uncertainties and estimation errors. In this case, the inversion methodology can produce accurate leakage estimates, no matter whether the detection problem itself is unique or non-unique depending on the number and configuration of monitoring wells. In a random configuration of two monitoring wells, the inversion methodology may need to test for different initial location guesses to have accurate estimates of the leakage parameters and an optimal match with pressure data. The detection was generally stable after the first a half year of injection and monitoring. In Example 2, with two monitoring wells and large pressure data noises, the inversion methodology can improve the estimation accuracy of the leakage parameters with increasing monitoring time as more data are available in the inversion. The detection accuracy and convergence speed with monitoring time depend on the actual configuration of the two monitoring wells. For an optimal configuration, an accurate detection can be achieved within the first 2–3 years of monitoring. When the formation parameters were uncertain and the pressure measurements were associated with large data noise (Example 3), the

detection can be improved by simultaneously calibrating formation parameters and leakage parameters. As shown in Example 4, joint inversion of pressure *and* surface-deformation measurements can significantly improve the speed of convergence toward the true solution of the leakage parameters and enable earlier, accurate detection of the location of the leaky well. This example demonstrates how high-resolution deformation data can help identify the leakage location and the pressure data from limited number of monitoring wells can help estimate the permeability of a leaky well or the leakage rate.

Finally, the methodology of early leakage detection was applied to hypothetical leakage problems at the Ketzin CO_2 pilot site in Germany. These problems were formulated by introducing a leaky well located at 675 m away from the injection well, with varying well permeability and thus leakage rate. At Ketzin, no signals of leakage of brine and CO_2 through the Weser/Amstadt formation from the Stuttgart formation to the Exter formation were observed during the CO_2 injection over 5 years. The monitoring system consists of one injection well and two monitoring wells in the storage formation, and one monitoring well in the Exter formation. A model calibration was first conducted to estimate large-scale spatial-varying permeability using pressure data observed during the pumping tests conducted prior to the CO_2 injection test. A forward model was developed using TOUGH2/EOS9, and the inverse modeling was conducted using iTOUGH2-PEST. The model calibration indicated that the storage formation in the near-well region contained sand channels and a low-permeability zone, and that the near-well region was located in a semi-closed system with a flow barrier located in the north. The calibrated large geologic features were consistent with the field monitoring of CO_2 injection. For early leakage detection, the "monitoring" pressure at four wells was obtained by simulating the CO_2 injection into the Stuttgart formation with the hypothetical leaky well. The forward model was developed for an extended 3-D domain of 15 km by 15 km covering the Stuttgart formation, the Weser/Amstadt formation, and the overlying Exter formation of ~260 m thickness in total, using site-specific data. Using a moderate injection rate of 1.59 kg/s for 2 years, the detection methodology could accurately estimate the leaky well permeability when the permeability was higher than 1,000 darcy, indicating that the methodology was applicable to large leakage events with high flow rates. In case the CO_2 injection rate increased by a factor of 10 (i.e., a half million tones CO_2 per year), a leaky well with 10 darcy permeability or higher could be accurately identified. The benefits of early leakage detection can be seen from the difference between the detection time (180 days) and the CO_2 arrival time (255 days) at the leaky well. Because the leakage pathway can be detected and characterized ahead of the arriving CO_2 plume, some measures can be undertaken to mitigate the leakage risks, such as ceasing CO_2 injection or pumping CO_2 back out of the injection zone.

The authors of this report realize that the work conducted so far shows promise in that early leakage detection via joint inversion has been successful for simplified test cases and a fictitious leakage scenario for the Ketzin site. Without prior optimization of monitoring well location, detection was achieved in many example cases, but only when the leakage pathways had relatively large permeability and clear anomalies could be recorded. Further work is required to test the detection framework envisioned in this study, for a larger range of conditions and eventually in comparison with data from a field demonstration site in which actual leakage signals have been measured.

6. REFERENCES

Amelung, F.; Galloway, D. L.; Bell, J. W.; Zebker, H. A.; Laczniak, R. J. Sensing the ups and downs of Las Vegas: InSAR reveals structural control of land subsidence and aquifer-system deformation. *Geology* **1999,** *27*, 483–486.

Anderson, M. P. Comment on "Universal scaling of hydraulic conductivities and dispersivities in geologic media" by S. P. Neuman. *Water Resour.Res.* **1991,** *27*, 1381–1382.

Avci, C. B. Evaluation of flow leakage through abandoned wells and boreholes. *Water Resour. Res.* **1994,** *30*, 2565–2578.

Bawden, G. W.; Thatcher, W.; Stein, R. S.; Hudnut, K. W.; Peltzer, G. Tectonic contraction across Los Angeles after removal of groundwater pumping effects. *Nature* **2001,** *412*, 812–815.

Bell, J. W.; Amelung, F.; Ferretti, A.; Bianchi, M.; Novali, F. Permanent scatter InSAR reveals seasonal and long-term aquifer-system response to groundwater pumping and artificial recharge. *Water Resour. Res.* **2008,** *44*, W02407. http://dx.doi.org/10.1029/2007WR006152.

Benson, S. M. Monitoring carbon dioxide sequestration in deep geological formations for inventory verification and carbon credits. 2006 SPE Annual Technical Conference and Exhibition, San Antonio, TX, 2006; SPE 102833;

Benson, S. M.; Trautz, R.; Shan, C. *Sensitivity of Pressure Monitoring for Leak Detection*; Lawrence Berkeley National Laboratory: Berkeley, CA, 2006.

BES (Office of Basic Energy Sciences, Department of Energy). *Basic Research Needs for Geosciences: Facilitating 21st Century Energy Systems*; U.S. Department of Energy: Washington, DC, 2007; p 86.

Beutler, G.; Hauschke, N.; Nitsch, E. Faziesentwicklung des Keupers im Germanischen Becken. In *Tias - Eine ganz andere Welt*. Hauschke, N.; Wilde, V., Eds; Mitteleuropa im frühen Erdmittelalter: Pfeil, München, 1999; 129–174.

Birkholzer, J. T.; Cihan, A.; Zhou, Q. Impact-driven pressure management via targeted brine extraction−Conceptual studies of CO_2 storage in saline formations. *Int. J. Greenhouse Gas Control* **2012,** *7*, 168–180.

Birkholzer, J. T.; Zhou, Q. Basin-scale hydrological impacts of CO_2 storage: Regulatory and capacity implications. *Int. J. Greenh. Gas Control* **2009,** *3*, 745–756.

Birkholzer, J. T.; Zhou, Q.; Tsang, C.-F. Large-scale impact of CO_2 storage in deep saline aquifers: A sensitivity study on the pressure response in stratified systems. *Int. J. Greenhouse Gas Control* **2009,** *3*, 181–194.

Buckley, S. M.; Rosen, P. A.; Hensley, S.; Tapley, B. D. Land subsidence in Houston, Texas, measured by radar interferometry and constrained by extensometers. *J. Geophys. Res.* **2003,** *108*, 2542. http://dx.doi.org/10.1029/2002JB001848

Carroll, S.; Hao, Y.; Aines, R. Geochemical detection of carbon dioxide in dilute aquifers. *Geochem. Trans.* **2009,** *10*. http://dx.doi.org/10.1186/1467-4866-10-4.

Celia, M. A.; Nordbotten, J. M.; Court, B.; Dobossy, M.; Bachu, S. Field-scale application of a semi-analytical model for estimation of CO$_2$ and brine leakage along old wells. *Int. J. Greenh. Gas Control* **2011,** *5*, 257–269.

Chabora, E. R.; Benson, S. M. Brine displacement and leakage detection using pressure measurements in aquifers overlying CO$_2$ storage reservoirs. *Energy Procedia*, **2009**, *1*, 2405–2412.

Chabora, E.; Benson, S. M. Monitoring pressure transients in zones overlying CO$_2$ storage reservoirs as a means of leak detection and diagnosis. In *Proceeding of 7th Annual Conference on Carbon Capture and Sequestration*, Pittsburgh, PA, May 7, 2008.

Chen, F.; Wiese, B.; Zhou, Q; Kowalsky, M. B.; Norden, B.; Kempka, T.; Birkholzer, J. T. Numerical modeling of the pumping tests at the CO$_2$ pilot site in Ketzin, Germany: Model calibration and heterogeneity effects. Submitted to *International Journal of Greenhouse Gas Control* **2013,** *22*, 200–212.

Cihan, A.; Birkholzer, J. T.; Zhou, Q. Pressure buildup and brine migration in CO$_2$ storage systems with multiple leakage pathways: Application of a new analytical solution. *Ground Water* **2013,** *51*, 252–267.

Cihan, A.; Zhou, Q.; Birkholzer, J. T. Analytical solutions for pressure perturbation and fluid leakage through aquitards and wells in multilayered aquifer systems. *Water Resour. Res.* **2011,** *47*, W10504. doi:10.1029/2011WR010721, W10504

Commer, M.; Kowalsky, M. B.; Doetsch, J.; Newman, G. A.; Finsterle, S. MPiTOUGH2: A parallel parameter estimation framework for hydrological and hydrogeophysical applications. *Computers & Geosciences* **2014,** *65*, 127–135. http://dx.doi.org/10.1016/j.cageo.2013.06.011i

Doetsch, J.; Kowalsky, M. B.; Doughty, C.; Finsterle, S.; Ajo-Franklin, J. B.; Carrigan, C. R.; Yang, X.; Hovorka, S. D.; Daley, T. M. Constraining CO$_2$ simulations by coupled modeling and inversion of electrical resistance and gas composition data. *Int. J. of Greenhouse Gas Control* **2013,** *18*, 510–522. http://dx.doi.org/10.1016/j.ijggc.2013.04.011

Doherty, J. *FORTRAN 90 Modules for Implementation of Parallelized, Model-Independent, Model-Based Processing*; Watermark Numerical Computing: Brisbane, Australia, 2007a.

Doherty, J. *PEST: Model-Independent Parameter Estimation*; Watermark Numerical Computing: Brisbane, Australia, 2007b.

Doughty, C.; Freifeld, B. M.; Trautz, R. C. Site characterization for CO$_2$ geologic storage and vice versa: The Frio brine pilot, Texas, USA as a case study. *Environmental Geology* **2008,** *54*, 1635–1656.

Fielding, E. J.; Blom, R. G.; Goldstein, R. M. Rapid subsidence over oil fields measured by SAR interferometry. *Geophys. Res. Lett*. **1998,** *27*, 3215–3218.

Finsterle, S. *iTOUGH2 Universal Optimization Using the PEST Protocol*; Report LBNL-3698E; Lawrence Berkeley National Laboratory: Berkeley, CA, 2011.

Finsterle, S. *iTOUGH2 User's Guide;* Report LBNL-40040; Lawrence Berkeley National Laboratory: Berkeley, CA, 2007.

Finsterle, S. *ITOUGH2 User's Guide*; Report LBNL-40040; Lawrence Berkeley National Laboratory, Berkeley, CA, 1999.

Finsterle, S. Multiphase inverse modeling: Review and iTOUGH2 applications. *Vadose Zone J.*, **2005,** *3*, 747–762.

Finsterle, S.; Zhang, Y. Solving iTOUGH2 simulation and optimization problems using the PEST protocol. *Environ. Modell. Softw*. **2011,** *26*, 959–968.

Fjær, E.; Holt, R. M.; Horsrud, P.; Raaen, A. M.; Risnes, R. *Petroleum related rock mechanics*, 2nd ed; Elsevier: Amsterdam, 2008.

Förster, A.; Norden, B.; Zinck-Jorgensen, K.; Frykman, P.; Kulenkampff, J.; Spangenberg, E.; Erzinger, J.; Zimmer, M.; Kopp, J.; Borm, G.; Juhlin, C.; Cosma, C.; Hurter, S. Baseline characterization of the CO2SINK geological storage site at Ketzin, Germany. *Environ. Geosciences* **2006,** *13*, 145–161.

Förster, A.; Schöner, R.; Förster, H.; Norden, B.; Blaschke, A.; Luckert, J.; Beutler, G.; Gaupp, R.; Rhede, D. Reservoir characterization of a CO_2 storage aquifer: The Upper Triassic Stuttgart Formation in the Northeast German Basin. *Mar. Pet. Geol.* **2010,** *27*, 2156–2172.

Frykman, P.; Zink-Jørgensen, K.; Bech, N.; Norden, B.; Förster, A.; Larsen, M. Site characterization of fluvial, incised-valley deposits. In *Proceedings, CO2SC Symposium*, Lawrence Berkeley National Laboratory: Berkeley, CA, Mar 20–22, 2006.

Galloway, D. L.; Hoffmann, J. The application of satellite differential SAR interferometry-derived ground displacements in hydrogeology. *Hydrogeol. J.* **2007,** *15*, 133–154.

Galloway, D. L.; Hudnut, K. W.; Ingebritsen, S. E.; Phillips, S. P.; Peltzer, G.; Rogez, F.; Rosen, P. A. Detection of aquifer system compaction and land subsidence using interferometric synthetic aperture radar, Antelope Valley, Mojave Desert, California. *Water Resour. Res.* **1998,** *34*, 2573–2585.

Gasda, S. E.; Bachu, S.; Celia, M. A. Spatial characterization of the location of potentially leaky wells penetrating a deep saline aquifer in a mature sedimentary basin. *Environ. Geol.*, **2004,** *46*, 707–720.

Hart, D. J.; Bradbury, K. R.; Feinstein, D. T. The vertical hydraulic conductivity of an aquitard at two spatial scales. *Ground Water* **2006,** *44*, 201–211.

Hoffmann, J.; Galloway, D. L.; Zebker, H. A. Inverse modeling of interbed storage parameters using land subsidence observations, Antelope Valley, California. *Water Resour. Res.* **2003,** *39*. http://dx.doi.org/10.1029/2001WR001252

Hoffmann, J.; Zebker, H. A.; Galloway, D. L.; Amelung, F. Seasonal subsidence and rebound in Las Vegas Valley, Nevada, observed by synthetic aperture radar interferometry. *Water Resour. Res.* **2001,** *37*, 1551–1566.

IPCC (Intergovernmental Panel on Climate Change). *IPCC Special Report on Carbon Dioxide Capture and Storage*; Cambridge University Press: New York, 2005.

Javandel, I.; Tsang, C. F.; Witherspond, P. A.; Morganwalp, D. Hydrologic detection of abandoned wells near proposed injection wells for hazardous waste disposal. *Water Resour. Res.* **1988,** *24*, 261–270.

Javandel, I.; Witherspoon, P. A. A method of analyzing transient fluid flow in multilayered aquifers. *Water Resour. Res.* **1969,** *5*, 856–869.

Jung, Y.; Zhou, Q.; Birkholzer, J. T. Early detection of brine and CO₂ leakage through abandoned wells using pressure and surface-deformation monitoring data: Concept and demonstration. Submitted to *Advances in Water Resources* **2013,** *62*, 555–569. http://dx.doi.org/10.1016/j.advwatres.2013.06.008

Kempka, T.; Kühn, M.; Class, H.; Frykman, P.; Kopp, A.; Nielsen, C.M.; Probst, P. Modelling of CO₂ arrival time at Ketzin – Part I. *Int. J. Greenh. Gas Control* **2010,** *4*, 1007–1015.

Kiessling, D.; Schmidt-Hattenberger, C.; Schuett, H.; Schilling, F.; Krueger, K.; Schoebel, B.; Danckwardt, E.; Kummerow, J. Geoelectrical methods for monitoring geological CO₂ storage: First results from cross-hole and surface–downhole measurements from the CO2SINK test site at Ketzin (Germany). *Int. J. Greenh. Gas Control* **2010,** *4*, 816–826.

Kowalsky, M. B.; Doetsch, J.; Commer, M.; Finsterle, S.; Doughty, C.; Zhou, Q.; Ajo-Franklin, J.; Birkholzer, J.; Daley, T. *Coupled Inversion of Hydrological and Geophysical Data for Improved Prediction of Subsurface CO₂ Migration*; NRAP-TRS-III-004-2016; NRAP Technical Report Series; U.S. Department of Energy, National Energy Technology Laboratory: Morgantown, WV*, 2016; p 56.

Lengler, U.; De Lucia, M.; Kühn, M. The impact of heterogeneity on the distribution of CO₂: Numerical simulation of CO₂ storage at Ketzin. *Int. J. Greenh. Gas Control* **2010,** *4*, 1016–1025.

Levenberg, K. A method for the solution of certain nonlinear problems in least squares. *Quart. Appl. Math*. **1944,** *2*, 164–168.

Lewicki, J. L.; Hilley, G. E. Eddy covariance mapping and quantification of surface CO₂ leakage fluxes. *Geophys. Res. Lett.* **2009,** *36*, L21802. http://dx.doi.org/10.1029/2009GL040775

Lewicki, J. L.; Hilley, G. E.; Fischer, M. L.; Pan, L.; Oldenburg, C. M.; Dobeck, L.; Spangler, L. Eddy covariance observations of surface leakage during shallow subsurface CO₂ releases. *J. Geophys. Res. – Atmos*. **2009,** *114*, D12302. http://dx.doi.org/10.1029/2008JD011297

Long, J. C. S.; Aydin, A.; Brown, S. R.; Einstein, H. H.; Hestir, K.; Hsieh, P. A.; Myer, L. R.; Nolte, K. G.; Norton, D. L.; Olsson, O. L.; Paillet, F. L.; Smith, J. L.; Thomsen, L. *Rock Fractures and Fluid Flow: Contemporary Understanding and Applications*; National Academy Press:Washington, DC, 1996.

Marquardt, D. W. An algorithm for least squares estimation of nonlinear parameters. *SIAM J. Appl. Math*. **1963,** *11*, 431–441.

Martens, S.; Kempka, T.; Liebscher, S.; Luth, S.; Moller, F.; Myttinen, A.; Norden, B.; Schmidt-Hattenberger, C.; Zimmer, M.; Kuhn, M.; The Ketzin Group. Europe's longest-operating on-shore CO₂ storage site at Ketzin, Germany: a progress report after three years of injection. *Environ. Earth Sci.* **2012,** *67*, 323–334.

Massonnet, D.; Feigl, K. L. Radar interferometry and its application to changes in the earth's surface. *Rev. Geophys.* **1998,** *36*, 444–500.

Massonnet, D.; Holzer, T.; Vadon, H. Land subsidence caused by the East Mesa geothermal field, California, observed using SAR interferometry. *Geophys. Res. Lett.* **1997,** *24*, 901–904.

Massonnet, D.; Rossi, M.; Carmona, C.; Adragna, F.; Peltzer, G.; Feigl, K.; Rabaute, T. The displacement field of the Landers earthquake mapped by radar interferometry. *Nature* **1993,** *364,* 138–142.

Matheron, G. Éléments pour une théorie des milieux poreux; Masson et Cie: Paris, 1967.

Moench, A. F. Double-porosity models for a fissured groundwater reservoir with fracture skin. *Water Resour. Res.* **1984,** *20,* 831–846.

Morris, J. P.; Hao, Y.; Foxall, W.; McNab, W. A study of injection-induced mechanical deformation at the In Salah CO$_2$ storage project. *Int. J. Greenh. Gas Control* **2011,** *5,* 270–280.

Morris, M. D. Factorial sampling plans for preliminary computational experiments. *Technometrics,* **1991,** *33,* 161–174.

NETL (National Energy Technology Laboratory). *Best Practices for Monitoring, Verification, and Accounting of CO$_2$ Stored in Deep Geologic Formations*; National Energy Technology Laboratory: Pittsburgh, PA, 2009.

Neuzil, C. E. How permeable are clays and shales? *Water Resour. Res.* **1994,** *30,* 145–150.

Nicot, J. P. Evaluation of large-scale CO$_2$ storage on fresh-water sections of aquifers: An example from the Texas Gulf Coast Basin. *Int. J. Greenh. Gas Control* **2008,** *2,* 582–593.

Nogues, J. P.; Nordbotten, J. M.; Celia, M. A. Detecting leakage of brine or CO$_2$ through abandoned wells in a geological sequestration operation using pressure monitoring wells. *Energy Procedia* **2011,** *4,* 3620–3627.

Nordbotten, J. M.; Celia, M. A.; Bachu, S. Analytical solutions for leakage rates through abandoned wells. *Water Resour. Res.* **2004,** *40,* W04204. http://dx.doi.org/10.1029/2003WR002997

Norden, B.; Förster, A.; Vu-Hoang, D.; Marcelis, F.; Springer, N.; Le Nir, I. Lithological and Petrophysical Core-Log Interpretation in CO2SINK, the European CO$_2$ Onshore Research Storage and Verification Project. *SPE Res Eval & Eng* **2010,** *13,* 179–192.

Norden, B.; Frykman, P. Geological modelling of the Triassic Stuttgart Formation at the Ketzin CO$_2$ storage site, Germany. *Int. J. Greenh. Gas Control* **2013,** *19,* 756–774.

Oldenburg, C. M.; Lewicki, J. L.; Hepple, R. P. *Near-Surface Monitoring Strategies for Geologic Carbon Dioxide Storage Verification*; Report LBNL-54089; Lawrence Berkeley National Laboratory: Berkeley, CA, 2003.

Pan, L. *User information document for: WINGRIDDER version 3.0*; 10024-UID-3.0-00; Lawrence Berkeley National Laboratory: Berkeley, CA, 2007.

Prevedel, B.; Wohlgemuth, L.; Legarth, B.; Henninges, J.; Schütt, H.; Schmidt-Hattenberger, C.; Norden, B.; Förster, A.; Hurter, S. The CO2SINK boreholes for geological CO$_2$ -storage testing. *Energy Procedia* **2009,** *1,* 2087–2094.

Pruess, K. ECO2N: A *TOUGH2 fluid property module for mixtures of water, NaCl, and CO$_2$*; LBNL-57952; Lawrence Berkeley National Laboratory: Berkeley, CA, 2005.

Pruess, K.; Nordbotten, J. M.; Zhang, K. Numerical simulation studies of the long-term evolution of a CO$_2$ plume under a sloping caprock. Paper presented at the TOUGH Symposium 2009, Lawrence Berkeley Natl. Lab., Berkeley, CA, Sept 14–16, 2009.

Pruess, K.; Oldenburg, C.; Moridis, G. *TOUGH2 User's Guide, Version 2.1*; LBNL-43134(revised); Lawrence Berkeley National Laboratory: Berkeley, California, 2011.

Pruess, K.; Oldenburg, C.; Moridis, G. *TOUGH2 User's Guide*, Version 2.0; LBNL-43134; Lawrence Berkeley National Laboratory: Berkeley, CA, 1999.

Rinaldi, A. P.; Rutqvist, J. Modeling of deep fracture zone opening and transient ground surface uplift at KB-502 CO_2 injection well, In Salah, Algeria. *International Journal of Greenhouse Gas Control* **2013,** *12*, 155–167.

Romanak, K. D.; Bennett, P. C.; Yang, C.; Hovorka, S. D. Process-based approach to CO_2 leakage detection by vadose zone gas monitoring at geologic CO_2 storage sites. *Geophys Res Lett* **2012,** 39, L15405. http://dx.doi.org/10.1029/2012GL052426

Rutqvist, J. The geomechanics of CO_2 storage in deep sedimentary formations. *Geotech. Geol. Eng.* **2012,** *30*, 525–551. doi:10.1007/s10706-011-9491-0

Saltelli, A.; Ratto, M.; Andres, T.; Campolongo, F.; Cariboni, J.; Gatelli, D.; Saisana, M.; Tarantola, S. *Global Sensitivity Analysis: The Primer*; John Wiley & Sons, Ltd.: Chichester, UK, 2008.

Sanchez-Vila, X.; Guadagnini, A.; Carrera, J. Representative hydraulic conductivities in saturated groundwater flow. *Rev. Geophys*. **2006,** *44*, RG3002.

Schmidt, D. A.; Bürgmann, R. Time dependent land uplift and subsidence in the Santa Clara Valley, California, from a large InSAR data set. *J. Geophys. Res*. **2003,** *108*, 2416. http://dx.doi.org/10.1029/2002JB002267

Schmidt-Hattenberger, C.; Bergmann, P.; Kießling, D.; Krüger, K.; Rücker, C.; Schütt, H.; Group, K. Application of a Vertical Electrical Resistivity Array (VERA) for monitoring CO_2 migration at the Ketzin site: First performance evaluation. *Energy Procedia* **2011,** *4*, 3363–3370.

Strazisar, N. R.; Wells, A. W.; Diehl, J. R.; Hammack, R. W.; Veloski, G. A. Near-surface monitoring for the ZERT shallow CO_2 injection project. *Int. J. Greenh. Gas Control* **2009,** *3*, 736–744.

Sun, A. Y.; Nicot, J. P. Inversion of pressure anomaly data for detecting leakage at geologic carbon sequestration sites. *Adv. Water. Resour*. **2012,** *44*, 20–29.

Sun, A. Y.; Zeidouni, M.; Nicot, J. P.; Lu, Z.; Zhang, D. Assessing Leakage Detectability at Geologic CO_2 Sequestration Sites Using the Probabilistic Collocation Method. *Adv. Water Resour*. **2013,** *56*, 49–60. http://dx.doi.org/10.1016/j.advwatres.2012.11.017

Vasco, D. W.; Ferretti, A.; Novali, F. Estimating permeability from quasi-static deformation: Temporal variations and arrival-time inversion. *Geophysics* **2008b,** *73*, O37–O52. http://dx.doi.org/10.1190/1.2978164

Vasco, D. W.; Ferretti, A.; Novali, F. Reservoir monitoring and characterization using satellite geodetic data: Interferometric synthetic aperture radar observations from the Krechba field, Algeria. *Geophysics* **2008a,** *73*, WA113–WA122. http://dx.doi.org/10.1190/1.2981184

Vasco, D. W.; Rucci, A.; Ferretti, A.; Novali, F.; Bissel, R. C.; Ringrose, P. S.; Mathieson, A. S.; Wright, I. W. Satellite-based measurements of surface deformation reveal fluid flow

associated with the geological storage of carbon dioxide. *Geophys. Res. Lett.* **2010,** *37*, L03303. doi:10.1029/2009GL041544

Watson, T. L.; Bachu, S. Identification of wells with high CO_2-leakage potential in mature oil fields developed for CO_2-enhanced oil recovery. SPE Improved Oil Recovery Symposium, Tulsa, OK, 2008; SPE 112924.

Wiese, B.; Böhner, J.; Enachescu, C.; Würdemann, H.; Zimmermann, G. Hydraulic characterisation of the Stuttgart formation at the pilot test site for CO_2 storage, Ketzin, Germany. *Int. J. Greenh. Gas Control* **2010,** *4*, 960–971.

Winterfeld, P. H.; Wu, Y. S. Parallel simulation of CO_2 sequestration with rock deformation in saline aquifers. SPE Reservoir Simulation Symposium, the Woodlands, Texas, Feb 21–23, 2011; SPE 141514.

Würdemann, H.; Zimmermann, G. Hydraulic characterisation of the Stuttgart formation at the pilot test site for CO_2 storage, Ketzin, Germany. *Int. J. Greenh. Gas Control* **2010,** *4*, 960–971.

Wurster, P. Geologie des Schilfsandsteins. Mitteilungen des Geologischen Staatsinstituts Hamburg **1964,** *33*, 1–40.

Xu, H.; Dvorkin, J.; Nur, A. Linking Oil Production to Surface Subsidence from Satellite Radar Interferometry. *Geophys. Res. Lett.* **2001,** *28*, 1307–1310.

Zeidouni, M.; Pooladi-Darvish, M.; Keith, D. W. Leakage detection and characterization through pressure monitoring. *Energy Procedia* **2011,** *4*, 3534–41.

Zettlitzer, M.; Moeller, F.; Morozova, D.; Lokay, P.; Würdemann, H. Re-establishment of the proper injectivity of the CO_2-injection well Ktzi 201 in Ketzin, Germany. *Int. J. Greenh. Gas Control* **2010,** *4*, 952–959.

Zhang, K.; Wu, Y.S.; Pruess, K. *User's guide for TOUGH2-MP—A massively parallel version of the TOUGH2 code*; Report LBNL-315E; Lawrence Berkeley National Laboratory: Berkeley, CA, 2008.

Zhou, Q.; Birkholzer, J. T.; Mehnert, E.; Lin, Y. F.; Zhang, K. Modeling basin- and plume-scale processes of CO_2 storage for full-scale deployment. *Ground Water* **2010,** *48*, 494–514.

Zhou, Q.; Birkholzer, J. T.; Tsang, C. F.; Rutqvist, J. A method for quick assessment of CO_2 storage capacity in closed and semi-closed saline formations. *Int. J. Greenh. Gas Control* **2008,** *2*, 626–639.

Zhou, Q.; Birkholzer, J.T. On scale and magnitude of pressure build-up induced by large-scale geologic storage of CO_2. *Greenh. Gases Sci. Technol.* **2011,** *1*, 11–20.

Zhou, Q.; Birkholzer, J.T.; Tasng, C.-F. A semi-analytical solution for large-scale injection-induced pressure perturbation and leakage in a laterally bounded aquifer-aquitard system. *Transp. Porous. Med.* **2009,** *78*, 127–148.

NRAP is an initiative within DOE's Office of Fossil Energy and is led by the National Energy Technology Laboratory (NETL). It is a multi-national-lab effort that leverages broad technical capabilities across the DOE complex to develop an integrated science base that can be applied to risk assessment for long-term storage of carbon dioxide (CO$_2$). NRAP involves five DOE national laboratories: NETL, Lawrence Berkeley National Laboratory (LBNL), Lawrence Livermore National Laboratory (LLNL), Los Alamos National Laboratory (LANL), and Pacific Northwest National Laboratory (PNNL).

Technical Leadership Team

Diana Bacon
Lead, Groundwater Protection Working Group
Pacific Northwest National Laboratory
Richmond, WA

Jens Birkholzer
LBNL Lab Lead
Lawrence Berkeley National Laboratory
Berkeley, CA

Grant Bromhal
Technical Director, NRAP
Research and Innovation Center
National Energy Technology Laboratory
Morgantown, WV

Chris Brown
PNNL Lab Lead
Pacific Northwest National Laboratory
Richmond, WA

Susan Carroll
LLNL Lab Lead
Lawrence Livermore National Laboratory
Livermore, CA

Abdullah Cihan
Lead, Reservoir Performance Working Group
Lawrence Berkeley National Laboratory
Berkeley, CA

Tom Daley
Lead, Strategic Monitoring Working Group
Lawrence Berkeley National Laboratory
Berkeley, CA

Robert Dilmore
NETL Lab Lead
Research and Innovation Center
National Energy Technology Laboratory
Pittsburgh, PA

Nik Huerta
Lead, Migration Pathways Working Group
Research and Innovation Center
National Energy Technology Laboratory
Albany, OR

Rajesh Pawar
LANL Lab Lead
Lead, Systems/Risk Modeling Working Group
Los Alamos National Laboratory
Los Alamos, NM

Tom Richard
Deputy Technical Director, NRAP
The Pennsylvania State University
State College, PA

Josh White
Lead, Induced Seismicity Working Group
Lawrence Livermore National Laboratory
Livermore, CA

NRAP Technical Report Series